Master's thesis

NTNU
Norwegian University of Science and Technology
Faculty of Information Technology and Electrical Engineering
Department of Electric Power Engineering

Marie Rønhaug Pettersen

Stability Assessment of a Microgrid

Master's thesis in Energy and Environmental Engineering
Supervisor: Mohammad Amin
June 2020

NTNU
Norwegian University of Science and Technology

Marie Rønhaug Pettersen

Stability Assessment of a Microgrid

Master's thesis in Energy and Environmental Engineering
Supervisor: Mohammad Amin
June 2020

Norwegian University of Science and Technology
Faculty of Information Technology and Electrical Engineering
Department of Electric Power Engineering

NTNU
Kunnskap for en bedre verden

Abstract

The increased focus on environmental pollution has also led to changes in the power industry. Today, it can be observed an increased integration of renewable energy sources to ensure a greener energy sector. The enabling technology is power electronics which can fulfill the new requirements of the future grid, including improved performance, higher reliability and controllability. However, the emerging proportion of power electronics also lead to power quality and stability issues, such as harmonic oscillations.

The focus of this thesis is to recognize sources of instability and to understand the importance of preliminary stability assessment of systems dominated by power electronics. Furthermore, it focuses on small-signal stability analysis in the frequency domain and introduces the impedance-based stability analysis as a method to predict the stability of a power electronics dominated system.

Throughout this thesis, the stability of a current controlled voltage source converter (VSC), a voltage controlled VSC, a grid connected microgrid and an islanded microgrid is investigated. The impact on the stability from control and system parameters are researched applying the impedance-based stability method. Additionally the thesis identifies the causes of instability and predicts the stability strength of the systems. The predicted stability is further verified by time domain simulations and the method is proven to be accurate and useful as a tool to help assess the stability of the investigated systems.

Sammendrag

Det økte fokuset på klimagassutslipp har ført til forandringer i kraftindustrien. I dag ser vi en økende integrering av fornybare energikilder for å sikre en grønnere energisektor. For å muliggjøre denne overgangen vil kraftelektronikk være en viktig nøkkel for å innfri de nye kravene til framtidens nett som innebærer høyere ytelse, større pålitelighet og kontrollerbarhet. Imidlertid fører den voksende andelen kraftelektronikk også til problemer med kraftkvalitet og stabilitet.

Fokuset til denne oppgaven er å gjenkjenne ulike kilder til ustabilitet og å forstå viktigheten av en forhåndsvurdering av et systems stabilitet. Videre fokuseres det på stabilitetsanalyse i frekvensdomenet og den impedansbaserte stabilitetsanalysen er introdusert som en metode for å forutsi stabiliteten til et system dominert av kraftelektronikk.

I denne oppgaven har stabiliteten til en strømstyrt omformer, en spenningsstyrt omformer, et mikrogrid tilkoblet nettet og et mikrogrid frakoblet nettet blitt undersøkt. Ved hjelp av den impedansbaserte stabilitetsanalysen har påvirkningen til system- og kontrollparametre blitt belyst og årsaken til ustabiliteten har blitt identifisert. Den forutsagte stabilitetstyrken har blitt verifisert gjennom simuleringer i tidsdomenet. Konklusjonen fra analyseresultatene er at den impedansbaserte stabilitetsanalysen egner seg som et godt og nøyaktig verktøy til bruk for å vurdere stabiliteten til de undersøkte systemene.

Preface

This thesis is submitted to the Norwegian University of Science and Technology (NTNU) as the final requirement to achieve a Masters of Science in the 5-years programme Energy and Environmental Engineering. The thesis has been created as a result of two separate periods. All necessary prerequisites were acquired during the fall 2019 and submitted in what is called a Specialization Project in December. The period from January 2020 to June 2020 has been used to build on to this knowledge, and the resulting research is presented in this thesis.

The research has been completed for the Department of Electrical Power Engineering at NTNU, with Associate Professor Mohammad Amin as main supervisor and Professor Marta Molinas as co-supervisor.

Acknowledgement

First and foremost, I have to thank Associate Professor Mohammad Amin as my main supervisor. He has always been available in the office for a discussion and has really succeeded in creating a good environment for learning. I also appreciate the way he dealt with the challenges of the coronavirus pandemic and managed to maintain the valuable communication in alternative ways. In addition to have given professional advice and guidance, our everyday conversation at the beginning of every meeting has been really appreciated in a time otherwise filled with academic theory.

I would also like to thank my friends, family and boyfriend for all support and help (and food), but also for all the non scientific conversations we have had throughout this period. I must also not forget to thank my brother who has taken me out to jog when my head has needed a break.

During my five years at NTNU I have received many wise words and advice from my grandfather. He is always encouraging and interested in my life, and this year it has been especially reassuring with our written communication through email. I would therefore like to thank my grandfather for being a support, but also a role model.

And lastly, I want to thank my cat who has been sitting next to (and some times on) my laptop for the last couple of months. She has been a steady support and must now be one of few cats with a lot of knowledge in power electronics (she has already started to brag..).

June 2020, Trondheim Marie Rønhaug Pettersen

Contents

List of Figures

List of Tables

List of Abbreviations

AC Alternating Current

CSC Current Source Converter

DC Direct Current

FFT Fast Fourier Transform

GNC Generalized Nyquist Stability Criterion

ICC Inner Current Control

IG Induction Generator

IGBT Insulated-Gate Bipolar Transistors

KCL Kirchhoff's Current Law

KVL Kirchhoff's Voltage Law

LCC Line Commutated Converter

PCC Point of Common Coupling

PI Proportional-Integral

PLL Phase Locked Loop

pu Per Unit

PV Photovoltaic

PWM Pulse Width Modulation

RHP Right Half-Plane

SRF Synchronous Reference Frame

VSC Voltage Source Converter

Chapter 1

Introduction

This chapter gives an introduction to the motivation behind the thesis. In addition, it presents the scope, highlights the contributions and outline the structure of the research.

1.1 Motivation and Problem Statement

1.1.1 The Future Grid

Environmental pollution from non-renewable energy resources such as coal and oil has made today's energy crisis and environmental issues more prominent. Because of this, an increased focus regarding making the energy sector greener has emerged. A larger proportion of renewable energy involves a technological shift in the power industry to enable a coordination between the grid and distributed generation [1].

Today's power grid is based on a centralized power generation from large power plants that often are located far away from the end-users. The most prominent advantage of centralized power is the ability to enhance the efficiency of energy use, while drawbacks are operational difficulties, high costs and difficulty in meeting the user's new requirements regarding reliability and safety [2]. This emphasizes the need of a decentralized power generation, built up by several small power generators. This technology is called distributed generation, which is a general term for renewables and non-renewables that have smaller capacity than the traditional power plants [3]. Some of the advantages of distributed generation are less pollution, reduction of line losses and operating costs, higher energy efficiency and improved performance and reliability of power supply [4].

While the number of distributed generation units are continuously increasing in today's power grid, new challenges for operating and controlling the power grid safely are created. The concept of microgrids emerged as a way to address these challenges [5]. A microgrid is directly connected to the user side and is a smaller, independent and decentralized

power system. It benefits from using power electronics and puts distributed generation units such as wind power, solar power, energy storage and gas turbine devices together. The basic structure of a microgrid is illustrated in Fig. 1.1. A microgrid brings benefits to both the user and the grid. It can be observed as a controllable power unit for large power grids because of its ability to meet, within a few seconds, the needs of the distribution grid. For the users, on the other hand, a microgrid will reduce feeder loss, increase the reliability and enhance the stability of local voltage.

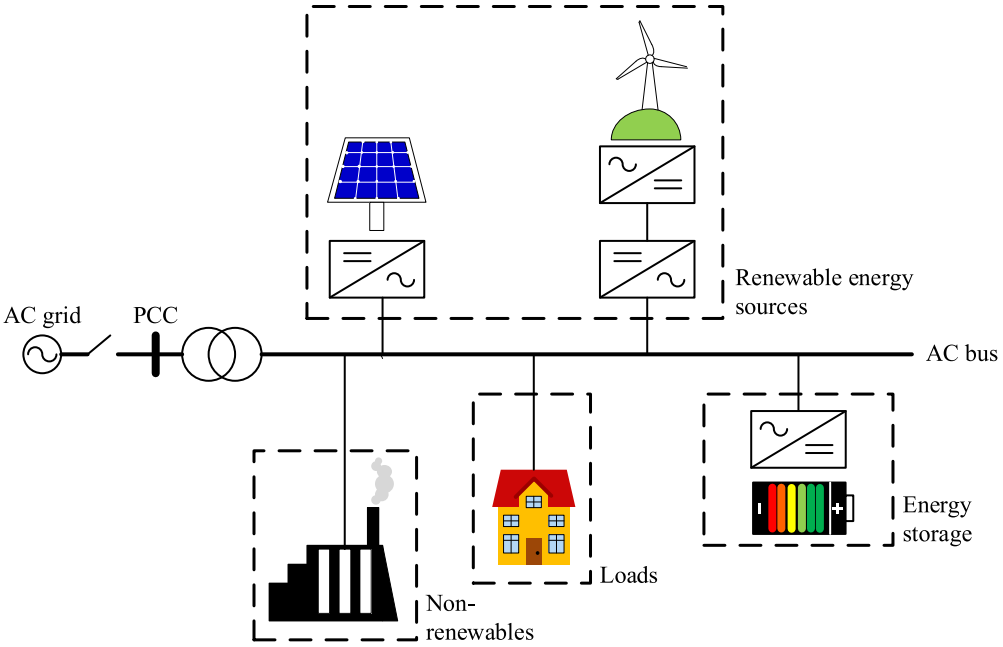

Figure 1.1: An illustration of the future power grid.

A microgrid is commonly known for five characteristics: (I) uniqueness, (II) diversity, (III) controllability, (IV) interactivity and (V) independency [6]. It is unique from its definition as a group of interconnected loads and microsources with clear and defined electrical boundaries that acts as a single unit connected or disconnected to the grid. This characteristic emphasizes the main difference from a large grid, which is the microgrid's ability to be flexible. It is diverse because of the composition. A microgrid can consist of both traditional power units, renewable energy and different type of loads. In addition, energy storage is necessary to ensure stable operations. Furthermore, a microgrid has high controllability because of its ability to choose the most appropriate control strategy. As an independent generation unit, a microgrid interacts with the grid such that it can provide support to the main grid and also receive support from the main grid when that is necessary. Because of the already mentioned ability to be connected or disconnected to the grid, a microgrid has high independency and works as an independent generation unit that can provide the local demand of power under circumstances where the grid experiences failure.

1.1.2 Stability Analysis

From the information above, the future grid, including microgrids, will therefore have many and more prominent advantages compared to today's grid. In addition to facilitate for renewable energy sources, the implementation of more power electronics will lead to higher reliability, efficiency and controllability [7]. On the downside, the integration of converters, such as voltage source converters (VSC), to the power system will result in power quality and stability issues [8]. This makes it necessary and important to get familiar with different stability analysis tools to understand the instability of a system dominated by power electronics [9].

There are several methods to analyze the stability of a power electronics dominated system. However, for small-signal stability analysis the most common used methods are the eigenvalue-based and the impedance-based stability analysis. They are known to need less computation and to include the impact of controller dynamics and the grid impedance on the stability [10]. This thesis will focus on analyzing the stability according to the impedance-based method. However, to substantiate the choice, advantages and disadvantages of the impedance-based and eigenvalue-based method will be presented.

As can be seen from the scheme in Fig. 1.2, both the impedance-based and the eigenvalue-based analysis methods are under the category of small-signal stability analysis in the frequency domain. Furthermore, the impedance-based analysis can be applied either on the alternating current (AC) side or the direct current (DC) side. If the method is applied to the AC side, the impedance model can either be derived in the sequence domain or the dq-domain. This thesis will focus on the AC-impedance in the dq-domain.

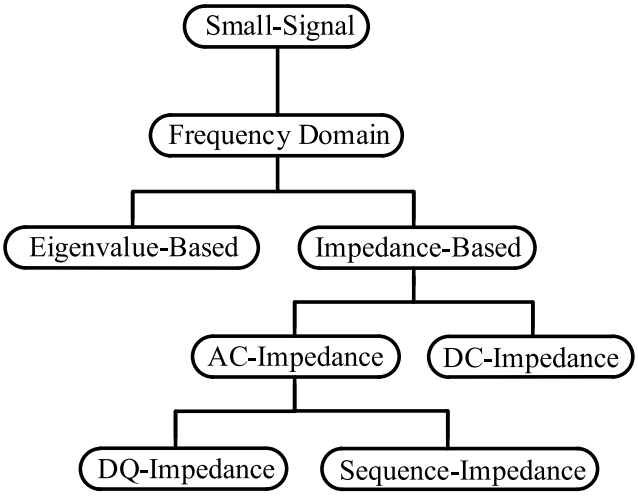

Figure 1.2: Small-signal stability analysis in the frequency domain.

As discussed in many other papers [11–14], the impedance-based method split the system into one source subsystem and one load subsystem. The ratio of the source impedance to the load impedance is called the minor loop gain and the stability of the system is found by applying the generalized Nyquist stability criterion (GNC) to this ratio [15].

The stability of the system is then predicted from the Nyquist plot. A stable system does not encircle the point $(-1, j0)$ and should have a sufficient phase margin higher than 35° [16]. The eigenvalue-based stability method, on the other hand, represents the system by a small-signal state-space model, and determines the stability by evaluating the position of the eigenvalues.

The major advantage of the impedance-based method is that even if the system is a black box the impedances of the two subsystems can be obtained from measurements from one single point. This further means that the impedances of the source and load subsystems can be found in real-time, which also applies for the stability. The eigenvalue-based stability method, on the other hand, requires detailed model information of the system to analytically derive the small-signal state-space model and consequently does not have the possibility to predict the stability in real time.

As already mentioned, the impedance-based stability analysis can either be applied on the DC side or the AC side of the converter. Different researches have discovered that if the analysis is applied on the DC side it will not be possible to observe some of the instability phenomena on the AC side and the other way around. This means that the impedance-based stability analysis is a local stability method, that might require several interfacing points to be able to analyze the stability of the whole system. On the other side, the eigenvalue-based stability analysis is a global stability method and is able to assess the stability of the whole system.

1.1.3 Sources of Instability

There are several different sources of instability in a power electronics dominated system, among others, a high grid impedance can influence the stability of the system. A grid-connected microgrid or other power electronics based power systems should in principle be stable for all grid conditions [17], but a weak grid can cause instability. A weak grid is brought by a high grid impedance, which can destabilize the current controller which again can lead to sustained harmonic oscillations.

It has also been proven that the control loops of the converter technology may be a source to instability. Among others, the phase locked loop (PLL) bandwidth and the parameters of the proportional-integral (PI) controller of the current controller can affect the stability of the system [18]. In addition, there might also arise stability issues regarding connecting several converter technologies in parallel to constitute a microgrid [19]. As a result of this, control loops might interact with each other, which can lead to harmonic instability [20].

The stability of grid-connected VSCs has been thoroughly researched in [21], which emphasizes the affect the current controller and PLL has on the stability. In [22] the stability of paralleled VSCs applying the impedance-based method is investigated. It proposes a method, based on the impedance-based stability analysis, that can predict the stability of paralleled VSCs. The origin of oscillations between an interconnected wind farm and a VSC-based HVDC system is thoroughly researched in [23, 24]. However,

it appears that there is a lack of research in the field of stability analysis applying the impedance-based stability method for grid-connected and islanded microgrids. The eigenvalue-based method is used to investigate the stability of a grid-connected microgrid in [25] and an islanded microgrid in [26]. The research in [27] look at the stability of a microgrid applying the impedance-based method, however, this thesis differs from other research by presenting a more thorough stability analysis by investigating the affect of several more sources of instability.

1.1.4 Problem Statement

The understanding of instability sources in the emerging power electronics dominated power systems is crucial to make the realization of the future grid possible. Therefore, in this thesis, the impedance-based stability analysis will be applied to different power electronics dominated systems, including: (I) a current controlled VSC, (II) an AC voltage controlled VSC, (III) a microgrid operating in grid-connected mode and (IV) a microgrid operating in islanded mode.

1.2 Objective of the Thesis

This thesis focuses on the analytical small-signal stability analysis of a power electronics dominated system. The analytical results are verified using numerical simulations, where the impact of passive and active components is investigated. The research result identifies how the stability of a power electronics dominated system is affected by change in different parameters. It discusses which components that affect most to instability, and what to consider when power electronics is cascaded. The objective of the thesis is motivated by the following research gap:

- Stability analysis of a microgrid in grid-connected and islanded mode.

1.3 Scope of the Thesis

To be able to investigate this subject, a small-signal stability analysis has been carried out for a VSC and a microgrid. A derivation of the small-signal state-space model and the impedance model of the system has therefore been necessary. Based on this, the impedance-based stability analysis has been applied and it has been possible to present findings in terms of what affects the stability in a VSC and a microgrid. To limit the complexity and to stay relevant to the subject, some assumptions where made:

- The investigated systems are relatively small.

- Mainly the impedance-based method is applied to analyze the stability.
- The focus is to study the interactions between the converter and the AC side and therefore, the control and impedance modeling of the DC side is omitted, assuming a constant DC voltage input.
- The VSCs constituting the microgrid is equal in control and structure to simplify the impedance modeling and stability analysis.

1.4 Contributions of the Thesis

This thesis has contributed to the field of research in stability analysis of power electronics dominated systems. The contribution is especially prominent with regard to stability analysis of grid-connected and islanded microgrids. The stability assessment has been performed by applying the impedance-based stability method. The contributions of the thesis includes the following:

- In Chapter 2, a step-by-step description of the topology and modeling of a current controlled and an AC voltage controlled VSC is presented. By combining the knowledge of different control strategies, a microgrid that can be operated in both grid-connected and islanded mode is presented.
- In Chapter 3, the linearized small-signal state-space model of the current controlled and AC voltage controlled VSC is derived. The two models are verified by comparing them to time domain simulations to ensure that they can be further used for stability analysis.
- In Chapter 4, the impedance model of the current controlled and AC voltage controlled VSC is derived, which is further used to derive the impedance model of the microgrid for different operating modes. Single tone approach is introduces as a method to verify the impedance models of a current controlled VSC.
- In Chapter 5, the stability of a current controlled VSC, an AC voltage controlled VSC and a microgrid is analyzed by applying the impedance-based method. The potential causes of instability are observed by changing different parameters of the system. The impacts of the grid impedance and control parameters are especially investigated. The research furthermore brings out how the stability changes when several VSCs are connected in parallel to form a microgrid.

1.5 Structure of the Thesis

In the following, the structure of the thesis is reviewed. Every chapter has an ingress in italics and a section named "Introduction". The ingress is meant as a short summary

to give the reader an idea of what the chapter will discuss. The introductory section, on the other hand, gives a more thorough establishment of the background of why the chapter is important, in addition to give a precise explanation of what each section in the chapter will go through.

Chapter 2 presents the description and topology of the microgrid that is analyzed further in this thesis. To build a microgrid it is necessary to get to know the building blocks, which in this case are VSCs. The topology of a VSC is furthermore thoroughly reviewed, including the pulse width modulation (PWM) and the LCL-filter. It is explained how different control strategies are necessary to enable both grid-connected and islanded operating modes of the microgrid, and both a current controlled and an AC voltage controlled VSC is studied. The above information is combined to present the control strategy of a microgrid, and lastly, simulations of the microgrid are shown.

Chapter 3 explains the importance of deriving a small-signal state-space model of the VSC. Many of the commonly used stability analysis must be applied to a linearized model. The state-space model of both the current controlled VSC and the AC voltage controlled VSC is therefore presented by describing the mathematical model of the physical system and the control system. Small-signal representation is applied to linearize the system and the models are verified by comparing the small-signal state-space responses to time domain simulations of a system that includes the nonlinear characteristics.

Chapter 4 introduces the impedance-based stability analysis. It first explains how the method divide a system into one source subsystem and one load subsystem. The ratio of the source impedance to the load impedance is called the minor-loop gain and the stability of the system is found by applying the GNC to this ratio. The system stability strength is decided from the characteristics loci of the minor-loop gain and the phase margin. Furthermore, the impedance models for both a current controlled VSC and an AC voltage controlled VSC is derived. This knowledge is further used to derive the impedance models of a grid-connected and an islanded microgrid. Lastly, the single-tone approach is introduced as a method to verify the analytically derived impedance models.

Chapter 5 presents the stability analysis of the systems. It first discusses the often seen sources of instability in a power electronics dominated system. The impedance-based method is first applied to the current controlled VSC for different cases such as changing the grid impedance or control parameters. The stability is predicted based on the Nyquist plot retrieved from the impedance ratio found in Chapter 4. The predicted stability is further verified by time domain simulations. Following, the stability of an AC voltage controlled VSC, grid-connected microgrid and islanded microgrid is investigated. The affect of having intermittent power sources with variable power input connected to the microgrid is also researched through simulations. Lastly, a discussion of the results is presented.

Chapter 6 includes a conclusion with the main findings and a recommendation for future work.

1.6 Relation to Specialization Project

The research in this thesis is based on work done in the project preceding this thesis [28]. The sections that are similar to the previous research includes:

- Section 4.3: DQ-Domain Impedance Modeling of the Current Controlled VSC
- Section 4.7: The Single-Tone Approach
- Section 5.2: Impedance-Based Stability Analysis of the Current Controlled VSC

The presented material in Chapter 2 is also based on the preceding project report, but is amended due to the new problem statement.

Chapter 2

Description and Control of a Microgrid

This chapter presents the description and control of the microgrid further analyzed in this thesis. First, the difference in modeling and control of a microgrid in grid-connected and islanded mode is explained. To constitute the microgrid, several VSCs are connected in parallel and the model and control of each individual converter is presented. Lastly, time domain simulations of the microgrid is shown.

2.1 Introduction

As mentioned in Chapter 1, today's power grid is in the middle of a big transition to facilitate the increased integration of renewables. The realization of the future grid will not be possible without power electronics and it can therefore be seen as the enabling technology. To be able to analyze the stability of a microgrid, it is necessary to know the building blocks, namely the VSCs. It is therefore important to gain knowledge of the topology and modeling of a VSC and to be able to design a control system that establishes stable operations. In addition, if a microgrid should have the possibility to operate in both grid-connected and islanded mode, different control strategies of the VSCs are required.

This chapter presents the microgrid that will be further analyzed in this thesis. Section 2.2 presents the modeling of a microgrid and the difference between grid-connected and islanded mode. Section 2.3 describes the topology of each individual VSC that constitutes the microgrid, and among others, mentions the role of a PWM and a LCL-filter. Two different control strategies of the VSC are discussed in Section 2.4. Section 2.5 combines all the previous knowledge to describe the control design of the microgrid and how it changes between the two different operation modes. Lastly, time domain simulations of the system are presented.

2.2 Description of a Microgrid

Fig. 2.1 illustrates a commonly used construction of a microgrid. Several VSCs are typically connected in parallel to constitute a microgrid. The VSCs convert the DC voltage, $v_{dc,n}$, to AC voltage, and are commonly used in power systems dominated by power electronics as a tool to achieve higher controllability [29]. The n converters are connected to the grid through LCL-filters at the point of common coupling (PCC). It consists of two inductances, $L_{1,n}$ and $L_{2,n}$, on each side of a capacitance, C_n. The microgrid can exchange power with the main grid at the PCC, which enhances the reliability and emphasizes the characteristic of interactivity.

The sum of each PCC current, $i_{o,n}$, is the grid current i_o. The grid voltage, v_g with the grid inductance, L_g, can be connected or disconnected to the microgrid through a switch, which maintain the characteristic of independency. To satisfy the requirement of diversity, the different converters n should incorporate both renewables, non-renewables, energy storage and loads.

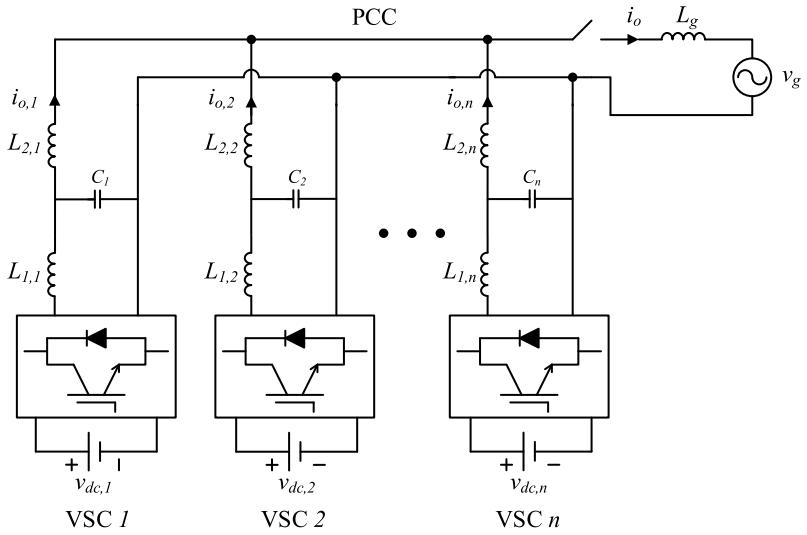

Figure 2.1: VSCs connected in parallel to form a microgrid.

2.2.1 Topology of the Microgrid

The topology of the microgrid that will be further analyzed is given in Fig. 2.2. To satisfy the characteristic of diversity, an induction generator (IG), wind power, photovoltaics (PVs), a battery energy storage system (BESS) and a regular RL-load are constituting the microgrid. The different loads and microsources are connected in parallel to the grid according to Fig. 2.1. Wind power produces AC voltages at varying frequencies and would first need an AC to DC converter and then a DC to AC converter to achieve constant frequency. For simplicity, the first converter step is not included.

Renewable power capacity grew with 8% in 2018 and for the last four years it has been

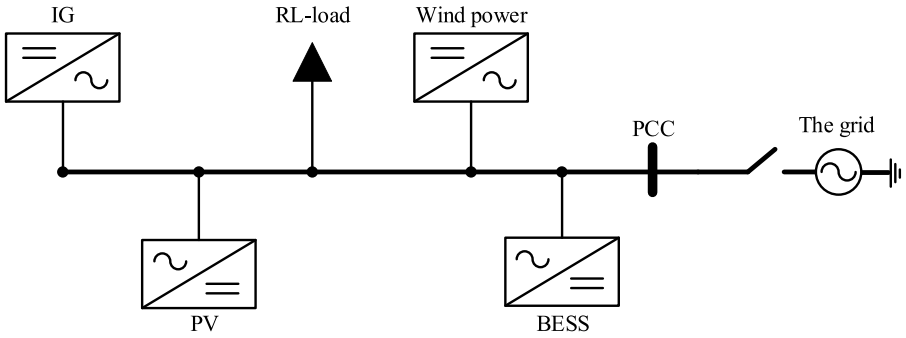

Figure 2.2: Topology of the microgrid.

installed more renewables than fossil fuel and nuclear power together [30]. The solar and wind power is therefore included to represent this growth in renewables and also to represent the intermittent power supplies, characterized by randomness and uncertainty, that often are found in microgrids. A BESS is included to introduce bidirectional power flow and plays an important part in the microgrid's ability to be independent of the main grid. Energy storage supports the independent operation of the microgrid by maintaining the dynamic balance of generation and load, stabilizing the system disturbance and keeping the stability of voltage and frequency.

Two loads are also connected to the grid, where one is a regular *RL*-load, while the other is an industry represented by an IG that requires DC voltage. While it is given that the loads consume power and wind and PV produces power, the BESS is either consuming or producing power based on if it is charging or discharging. All the converters are connected to the grid through the PCC and a switch is implemented on the grid side to enable the change from grid-connected to islanded mode. For simplicity, all of the microsources and loads are connected to the grid through equal VSCs and the power produced is represented by a constant DC voltage source. For further simplicity the grid has a constant value and is therefore considered as a stiff grid.

2.2.2 Grid-Connected Mode

A microgrid can be operated in grid-connected or islanded mode based on what the need is. During grid-connected mode, the power can flow in both directions and the two parts, grid and microgrid, serve as a backup for each other [31]. The microgrid adjusts the power balance of supply and demand by sending power to or retrieving power from the main grid. Also, the voltage and frequency regulation are managed by the main grid.

The control principle of the microgrid is also changed based on if it is in grid-connected or islanded mode. When the switch of the microgrid in Fig. 2.2 is closed it is operated in grid-connected mode. The main grid is therefore handling the voltage and frequency regulation and all of the VSCs are based on a current controlled strategy [27]. A current reference is given as input to the control system and the amount of power is therefore decided by the absolute value of this input. By choosing between a negative and a positive

current reference, the converter is either producing or consuming power, respectively. The modeling and control principle of a current controlled VSC is further discussed in Subsection 2.4.3.

2.2.3 Islanded Mode

A microgrid can be operated in islanded mode for different reasons [32]. Among others, it can be because of an unplanned incident if the main grid is experiencing a failure. By disconnecting the grid, the microgrid is still able to supply critical loads with power and prevent sudden power outages. A planned incident could be disconnecting the grid during preplanned maintenance on the main grid. This would allow performing maintenance on substations and feeders without the user experiencing service interruption. Another advantage of islanded operations is the ability to disconnect the microgrid during peak hours [33]. In that way it is possible to avoid importing power from the grid by being self-sufficient during such hours.

Since the grid is disconnected when the microgrid is operating in islanded mode, it is necessary that one of the VSCs are based on an AC voltage controlled strategy. It is a logic choice to implement this control strategy on the BESS converter, considering its possibility to change between charging and discharging operations. While the other current controlled VSCs must follow a given current reference, the BESS can change its current to ensure that the PCC voltage stays constant at the desirable value. The modeling and control principle of an AC voltage controlled VSC is further discussed in Subsection 2.4.4.

2.3 The Voltage Source Converter

The energy technologies constituting the microgrid in Fig. 2.2 all provide a DC output which requires power electronics to interface with the grid [34]. There are proposed and utilized several different converter topologies throughout the world to serve this task, but it mainly exists two dominant types which is the line commutated converter (LCC) and the voltage source converter. As already mentioned, the microgrid presented in Section 2.2 will be built by VSCs. However, advantages and disadvantages of both technologies as done in [35] will be presented to substantiate the choice.

The LCC is also known as a current source converter (CSC) because the output current is kept constant. It has a converter bridge that is built up by thyristors as shown in Fig. 2.3a. This only provides turn-on control while the turn-off is dependent on zero crossing of the current. To commutate, the LCC is line-commutated and requires a high synchronous voltage source and black-start operation is therefore impossible during a blackout. The converter bridge of the VSC shown in Fig. 2.3b, on the other hand, is built up by insulated gate bipolar transistors (IGBTs) that can both be turned on and off in response to the gate signal. As a self-commutated converter, it creates its own

AC signal and black-start operation, which is beneficial from a microgrid perspective, is therefore possible. The thyristors of the LCC only conduct the current in one direction, and power reversal is therefore performed by inverting the DC voltage polarity. The power reversal of a VSC is much faster because of the diodes that are connected in anti-parallel across the IGBTs and allow the currents to flow in both directions.

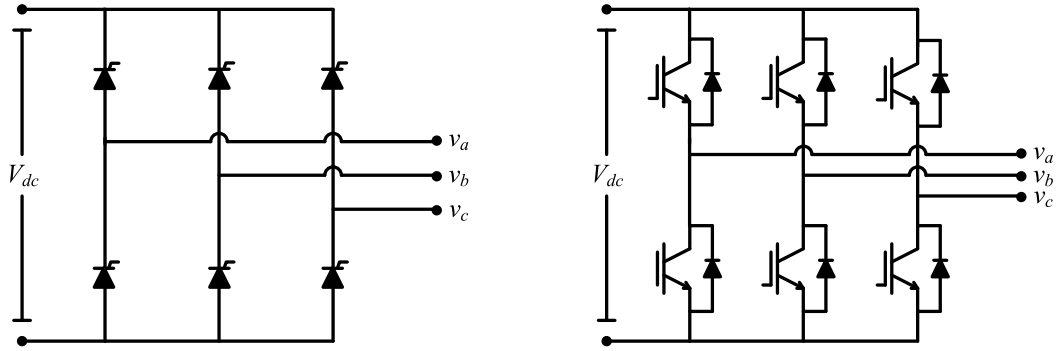

(a) (b)

Figure 2.3: Converter bridge of: (a) a three-phase LCC and (b) a three-phase VSC.

However, there are also disadvantages with the VSC, such as harmonics, high switching losses and high voltage stress. Harmonics appear as a result of the AC side voltages and currents which contain harmonic components of frequencies that are an integer multiple of the switching frequency [36]. Lower order harmonics are more severe than higher order harmonics, and the problem can therefore be reduced by increasing the switching frequency [37]. This introduces another drawback with the VSC which is high switching losses due to rapidly turn-on and turn-off of the IGBTs [38]. Because of the series connection of the IGBTs, the semiconductors must withstand full voltage stress which will introduce stress on the equipment insulation. Regardless of these disadvantages, the VSC is predicted to be increasingly applied in power electronics dominated power systems in the future [39]. It is commonly chosen because of its contollability, simple system interface and low carbon footprint because of few components [40]. In addition, its possibility to control active and reactive power independently and its role as a basic building block for cascaded converters makes it convenient and appropriate to use in a microgrid.

2.3.1 Topology of a Voltage Source Converter

Fig. 2.4 depicts the structure of each individual three-phase two-level VSC which is used to perform the conversion between DC and AC in the microgrid. The produced or consumed power is represented by a constant DC voltage source, v_{dc}. The converter bridge is built up by six IGBTs as semiconductor switches which at a high switching frequency utilize PWM. Only one of the switches in each leg can be turned on at the same time, and three switches are always conducting to avoid short-circuiting and to maintain the three-phase output converter currents and voltages, i_l and v_{cv} [41]. It

is called a two-level VSC because of the switching devices which are complementary operated to either have an output level of $+v_{dc}/2$ or $-v_{dc}/2$.

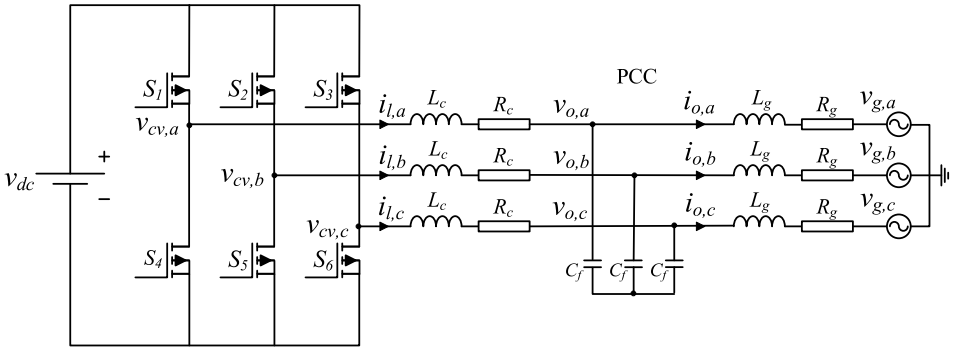

Figure 2.4: Topology of each individual three-phase VSC.

Furthermore follows the total series inductance and resistance between the converter and PCC, L_c and R_c, and the grid impedance, L_g and R_g. Together with the filter capacitance, C_f, this constitutes a LCL-filter that eliminates high order frequencies. The voltage at the PCC is v_o. When the VSC has an AC voltage controlled strategy the grid is disconnected and a load inductance and resistance, L_l and R_l is necessary to maintain the voltage. For simplicity, the system parameter values of each individual VSC are the same and are given in Table 2.1, where f is the grid frequency and fsw is the converter switching frequency. A per unit (pu) system is given in Appendix A and is developed to simplify calculations and to easier understand the relationship between the parameter magnitudes. It will also be beneficial in Chapter 3 where the small-signal state-space model of the system is established.

Table 2.1: Parameters of each individual VSC.

Parameter	Value
Rated power, S	15 kVA
Rated AC voltage, v_g	230 V
Rated frequency, f	50 Hz
Rated DC voltage, v_{dc}	375 V
Switching frequency, f_{sw}	8000 Hz
Converter Inductance, L_c	0.1 pu
Converter Resistance, R_c	0.005 pu
Filter Capacitance, C_f	0.016 pu
Grid Inductance, L_g	0.16 pu
Grid Resistance, R_g	0.02 pu
Grid Inductance, L_l	0.16 pu
Grid Resistance, R_l	2.8 pu

2.3.2 Pulse Width Modulation

As already mentioned, PWM is used to create the desired sinusoidal form of the converter output voltage. It keeps the voltage constant, while it allows simultaneous adjustment of the amplitude and phase angle of the voltage. This brings advantages such as being able to control active and reactive power independently and also the fast reversal of power flow [42]. Fig. 2.5 shows the performance of the PWM. It behaves as a comparator and compare a low frequency reference signal, v_{ref}, with a high frequency triangular waveform, $v_{carrier}$. In the case shown in Fig. 2.5 the reference signal has a frequency of 50 Hz, while the triangular waveform has a frequency of 2000 Hz. If the sinusoidal waveform is higher than the triangular waveform the PWM signal is 1 and opposite, if the sinusoidal waveform is less than the triangular waveform the PWM signal is set to 0.

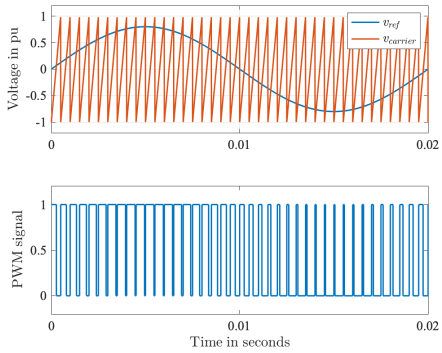

Figure 2.5: The behavior of a PWM.

Fig. 2.6a shows the resulting converter output voltage and since the PWM is operated at a high frequency, most of the harmonics are found around the switching frequency [43]. Fig. 2.6b shows the fast Fourier transform (FFT) plot of the output voltage in Fig. 2.6a, and as can be seen most of the harmonics are located around the 40^{th} harmonic, which corresponds to the switching frequency. A filter is therefore necessary to eliminate these high order harmonics.

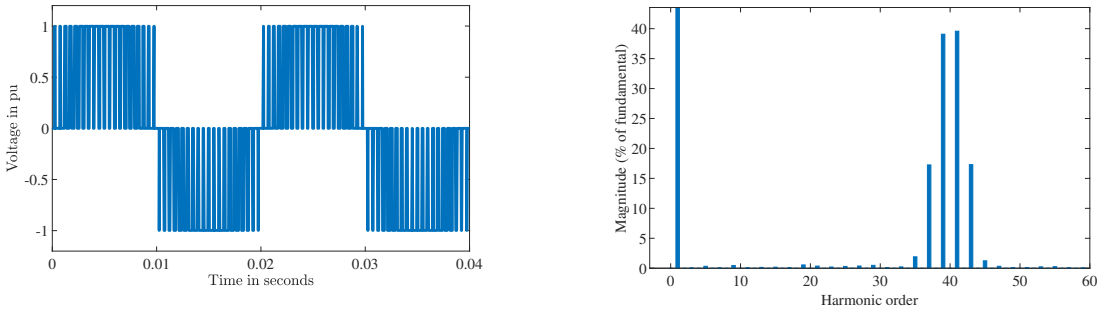

(a) (b)

Figure 2.6: (a) Converter output voltage and (b) FFT of the converter output voltage.

2.3.3 LCL-filter

A LCL-filter is chosen to filter out the high order harmonics generated from the high switching frequency of the PWM. The filter has the ability to reduce resonance between the grid and the converter and to debilitate the switching current ripples [44]. The LCL-filter is also often chosen because of practical limitations such as weight, size and cost. Fig. 2.7 shows the per phase equivalent of the LCL-filter. From the equivalent circuit, the transfer function, $Y_{LCL}(s)$, between converter output voltage and grid current can be found as in (2.1). ω_{res} is the resonance frequency and is given as in (2.2).

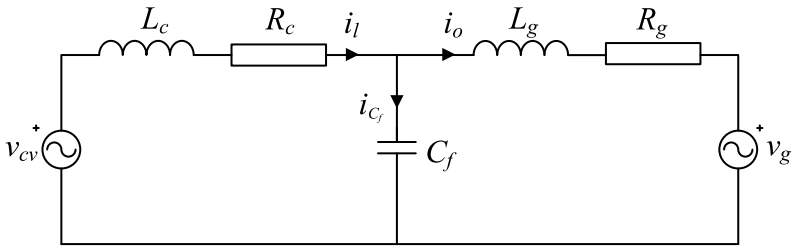

Figure 2.7: Per phase equivalent circuit of the LCL-filter.

$$Y_{LCL}(s) = \frac{i_o(s)}{v_{cv}(s)} = \frac{1}{sL_cL_gC_f\left(s^2 + s(\frac{R_c}{L_c} + \frac{R_g}{Lg}) + \omega_{res}\right) + R_c + R_g} \tag{2.1}$$

$$\omega_{res} = \sqrt{\frac{1}{L_cC_f} + \frac{1}{L_gC_f} + \frac{R_cR_g}{L_cL_g}} \tag{2.2}$$

The parameters L_c, R_c, R_g and L_g are already given in Table 2.1 and are chosen from commonly used values of a VSC, while the filter capacitance, C_f, is chosen in such a way that the harmonics around the switching frequency will be eliminated. To achieve this, the resonance frequency, f_{res}, must be lower than the switching frequency. The resonance frequency is often defined as in (2.3) and by solving (2.2) with respect to C_f the filter capacitor can be decided as in (2.4).

$$f_{res} = \frac{1}{5}f_{sw} = 1600\,\text{Hz} \tag{2.3}$$

$$C_f = \left(\frac{1}{L_c} + \frac{1}{L_g}\right)\left(\frac{1}{\omega_{res}^2 - \frac{R_cR_g}{L_cL_g}}\right) = 0.016\,\text{pu} \tag{2.4}$$

The Bode plot of the transfer function $Y_{LCL}(s)$ is shown in Fig. 2.8 and as can be seen the harmonics around the switching frequency are damped.

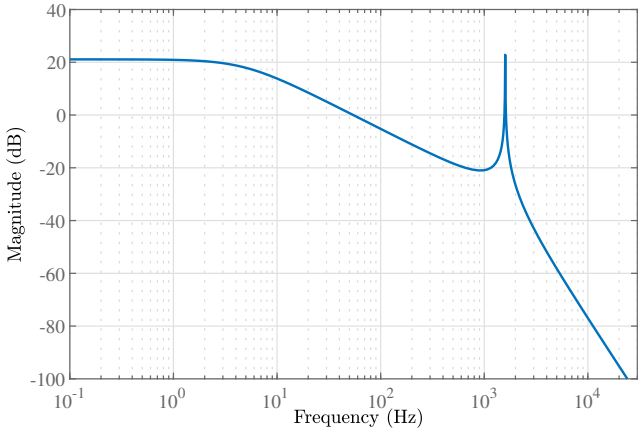

Figure 2.8: Bode plot of the LCL-filter.

2.4 Control of the Voltage Source Converter

A commonly used control method of the VSC is vector control [45] where AC signals are transformed into two constant signals using the direct-quadrature-zero (dqz) transform. The z-component is zero for symmetric systems, as is the case for the system in this thesis. A Clarke transformation is first used to convert a three-phase (abc) stationary coordinate system to a two-phase ($\alpha\beta$) stationary coordinate system. Furthermore, a Park transformation is used to transform the two components in the $\alpha\beta$-frame to a rotating coordinate system in the dq-frame. The result from these two transformations is that AC signals are transformed to two constant signals in a synchronous reference frame (SRF), which significantly simplifies the computations and static errors can be avoided in the control system by using PI-controllers [46,47]. The method and approach of dqz-transform is further explained in Appendix B.

As already mentioned in Section 2.2, the control principle of the microgrid will change based on if it is in grid-connected or islanded mode. An overview of the general control principle is depicted in Fig. 2.9. As can be seen a PLL is necessary to retrieve the phase angle of the voltage and to enable the transform from abc-frame to dq-frame. The control of the VSC consists of an inner current control loop. When the microgrid is grid-connected it is not necessary with an outer control loop that controls the reference signals, i_{ldref} and i_{lqref}. However, when the grid is disconnected and the microgrid is operated in islanded mode an outer AC voltage control loop is necessary to generate the reference currents that are the input of the current controller. Each and every element of the control principle depicted in Fig. 2.9 is discussed in the following subsections.

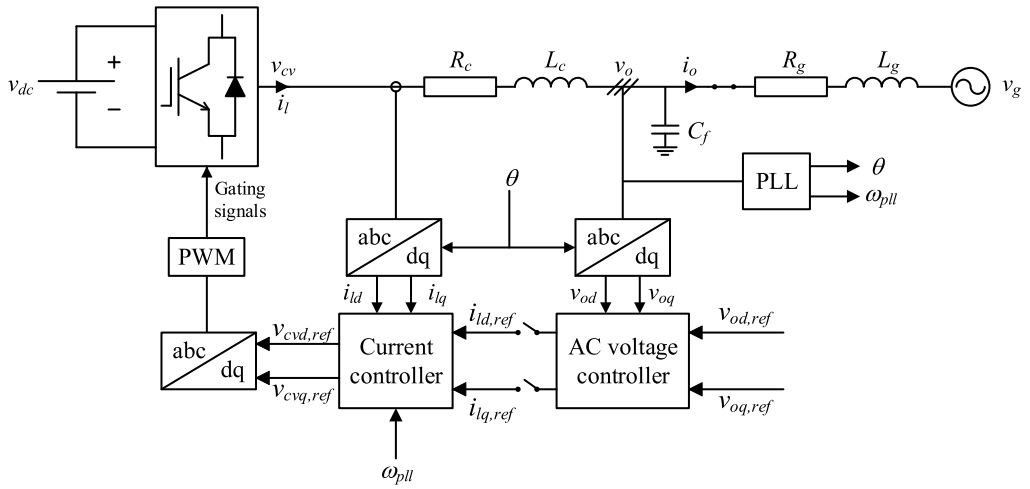

Figure 2.9: Control principle of the VSC.

2.4.1 Modeling of the Voltage Source Converter

Fig. 2.9 is further used to derive the mathematical model of the VSC. The difference between converter voltage and the voltage at the PCC is found in (2.5) by applying Kirchhoff's voltage law (KVL) on the AC side. The subscript k represents each phase, a, b and c, of the converter.

$$v_{cv,k} - v_{o,k} = R_c i_{l,k} + L_c \frac{di_{l,k}}{dt} \tag{2.5}$$

To control the system, the equation has to be transformed into dq-frame as in (2.6). This adds an extra coupled term, $\omega_g L_c i_{ld}$ and $\omega_g L_c i_{lq}$, that will be accounted for later.

$$\begin{aligned} v_{cvd} - v_{od} &= R_c i_{ld} + L_c \frac{di_{ld}}{dt} - \omega_g L_c i_{lq} \\ v_{cvq} - v_{oq} &= R_c i_{lq} + L_c \frac{di_{lq}}{dt} + \omega_g L_c i_{ld} \end{aligned} \tag{2.6}$$

The active power, P, and reactive power, Q, are expressed as in (2.7).

$$\begin{aligned} P &= \frac{3}{2}(v_{oq} i_{lq} + v_{od} i_{ld}) \\ Q &= \frac{3}{2}(v_{oq} i_{ld} - v_{od} i_{lq}) \end{aligned} \tag{2.7}$$

To simplify these two equations, the dq-frame voltage vector, v_{od}, is aligned on top of v_o. This process is illustrated in Fig. 2.10 and the result is that $v_{oq} = 0$, which changes the power equations to (2.8).

$$\begin{aligned} P &= \frac{3}{2} v_{od} i_{ld} \\ Q &= -\frac{3}{2} v_{od} i_{lq} \end{aligned} \tag{2.8}$$

It is now clear that by taking advantage of the dq-frame, it is possible to independently control active and reactive power. Active power is controlled by controlling i_{ld}, while reactive power is controlled by controlling i_{lq}. The angle of the voltage position, θ, is found from Fig. 2.10b and given by (2.9), where $v_{o\alpha}$ and $v_{o\beta}$ are the voltage components of the $\alpha\beta$-frame.

$$\theta = \tan^{-1}\left(\frac{v_{o\beta}}{v_{o\alpha}}\right) \tag{2.9}$$

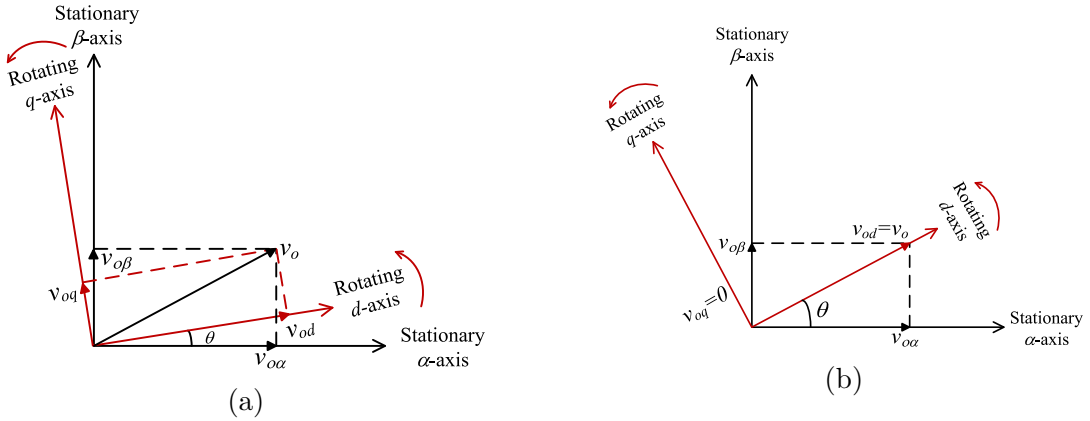

Figure 2.10: (a) Before v_{od} is aligned on top of v_o and (b) after v_{od} is aligned on top of v_o.

2.4.2 Phase Locked Loop

The angular position of the voltage, θ, is retrieved by using a phase locked loop. A PLL makes an output signal synchronize with a reference input signal in both phase and frequency [48] and is therefore widely used in the task of synchronizing power electronics based converters [49].

Fig. 2.11 shows a commonly used topology of a PLL. The input of the PLL is the three-phase PCC voltage, v_o. This voltage is transformed to the dq-frame so that the system can be oriented in such a way that the q-component of the voltage, v_{oq}, equals zero. The adjustment of orientation is served by a PI-controller with k_{ppll} as proportional gain and k_{ipll} as integral gain [50]. By integrating the PLL frequency, ω_{pll}, the phase angle of the voltage is retrieved.

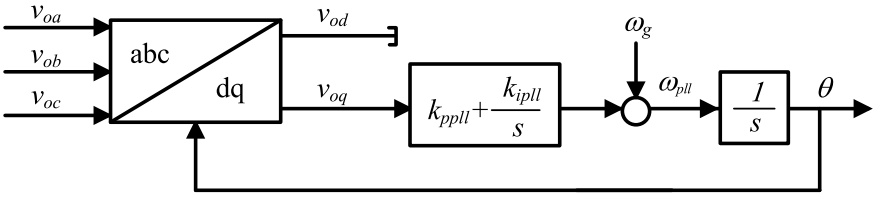

Figure 2.11: Block diagram of the PLL.

The open loop transfer function of the PLL is found in (2.10) where $T_{ipll} = k_{ppll}/k_{ipll}$. By inserting the values of the integral gain and proportional gain given in Table 2.2, the Bode plot of the open loop transfer function is as in Fig. 2.12. It has a sufficient phase margin of 39.9° and the phase will never cross below the −180° line which means that the closed loop transfer function of the PLL will stay stable.

$$G_{ol}(s) = \underbrace{\left(K_{p,ppl}(\frac{1 + sT_{i,pll}}{sT_{i,pll}}) \right)}_{\text{PI}} \cdot \underbrace{\frac{1}{s}}_{\text{I}} \tag{2.10}$$

Table 2.2: Parameters of the PLL.

Parameter	Value
K_{ppll}	0.0844 p.u.
K_{ipll}	4.6908 p.u.

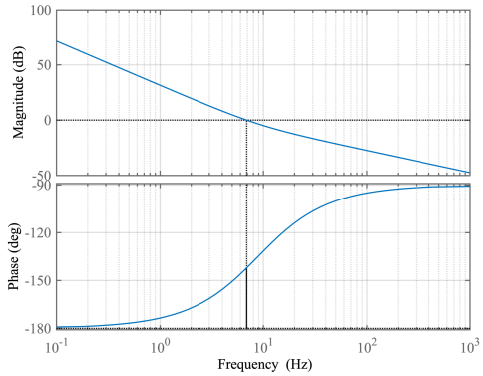

Figure 2.12: Bode Plot of the open loop transfer function of the PLL.

2.4.3 Inner Current Control Loop

Fig. 2.13 depicts the inner current control loop of the VSC, which consists of a PI-regulator, a PWM and the system.

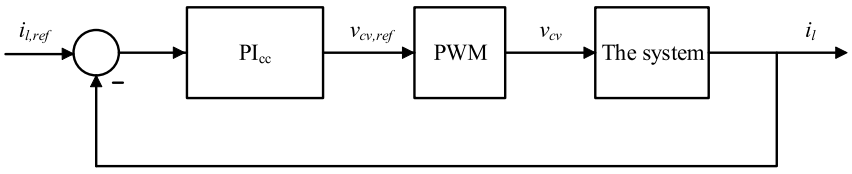

Figure 2.13: Block diagram of inner current control loop.

The PI-controller, with a proportional gain of k_{pc} and integral gain of k_{ic}, is used to ensure that the current follows its reference. The PI-controller is a good trade off between complexity and performance, and hence is the most used controller in the industry [51]. The input of the PI-regulator is the error between reference current, $i_{l,ref}$, and actual inductance current, i_l, while the output is the converter reference voltage, $v_{cv,ref}$. The transfer function of the PI-controller when the control design is implemented in dq-frame is given in (2.11), where $T_{ic} = k_{pc}/k_{ic}$ and the superscript "dq" means that it is valid for both d- and q-axis.

$$\frac{v_{cv,ref}^{dq}(s)}{i_{l,ref}^{dq} - i_{l}^{dq}} = k_{pc}\left(\frac{1 + sT_{ic}}{sT_{ic}}\right) \tag{2.11}$$

As described in Subsection 2.3.2 the PWM behaves as a comparator that compares a high frequency triangular waveform with a reference control signal. The output of the PI-regulator, $v_{cv,ref}$, is the input of the PWM and therefore also the reference control signal. The PWM can be approximated as a delay and represented by a first order transfer function shown in (2.12), where the time delay $\tau_a = T_{sw}/2$.

$$\frac{v_{cv}^{dq}(s)}{v_{cv,ref}^{dq}(s)} = \frac{1}{1 + s\tau_a} \tag{2.12}$$

The output of the PWM is gating signals that are used to control the switching of the VSC. The result of this switching is the converter output voltage v_{cv}. The next step of the inner current controller is the system which is already described in (2.6). The system equations in pu are given in (2.13).

$$\begin{aligned} v_{cvd,pu} - \underbrace{v_{od,pu}}_{\text{Feed-forward}} &= R_{c,pu} i_{ld,pu} + \frac{L_c}{\omega_b}\frac{di_{ld,pu}}{dt} - \underbrace{\omega_{g,pu} L_{c,pu} i_{lq,pu}}_{\text{Feed-forward}} \\ v_{cvq,pu} - \underbrace{v_{oq,pu}}_{\text{Feed-forward}} &= R_{c,pu} i_{lq,pu} + \frac{L_c}{\omega_b}\frac{di_{lq,pu}}{dt} + \underbrace{\omega_{g,pu} L_{c,pu} i_{ld,pu}}_{\text{Feed-forward}} \end{aligned} \tag{2.13}$$

While the PI-controller and the PWM have the same transfer function in both abc-frame and dq-frame, it has already been mentioned that the system equations will consist of one extra cross coupled term in the dq-frame. To decouple the two equations, feed-forward according to (2.13) is used to eliminate the cross coupling. This process is shown in Fig. 2.14.

This gives new system equations as in (2.14). The system equations are now decoupled which enable independent control of d- and q-axis which is an essential characteristic of vector control.

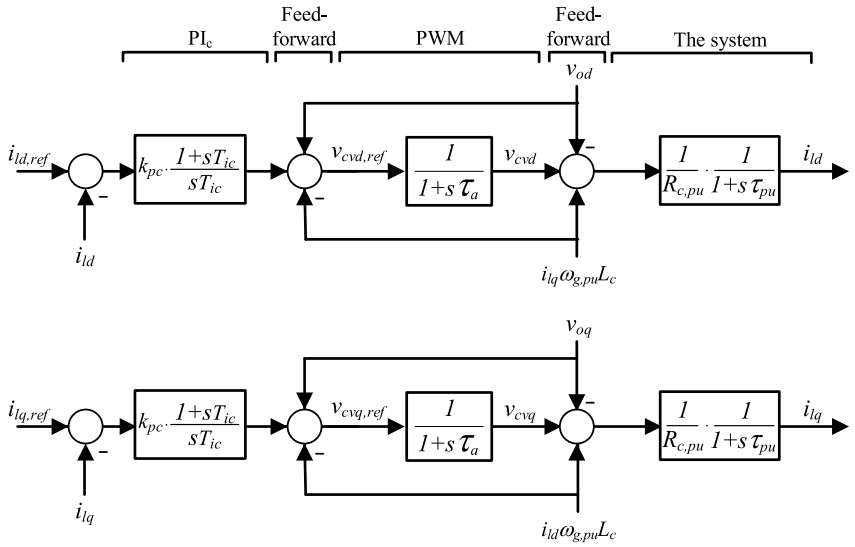

Figure 2.14: Block diagram of inner current control loop in dq-frame.

$$
\begin{aligned}
v_{cvd,pu} &= R_{c,pu} i_{ld,pu} + \frac{L_c}{\omega_b} \frac{di_{ld,pu}}{dt} \\
v_{cvq,pu} &= R_{c,pu} i_{lq,pu} + \frac{L_c}{\omega_b} \frac{di_{lq,pu}}{dt}
\end{aligned}
\tag{2.14}
$$

From Laplace transformation the transfer function of the system can be represented as a simple first order system as given in (2.15).

$$
\frac{i_{l,pu}^{dq}(s)}{v_{cv,pu}^{dq}(s)} = \frac{1}{R_{c,pu}} \frac{1}{1 + s\tau_{pu}}, \quad \tau_{pu} = \frac{L_{c,pu}}{\omega_b R_{c,pu}}, \quad L_{c,pu} = \omega_b \frac{L_c}{Z_b}, \quad R_{c,pu} = \frac{R_c}{Z_b} \tag{2.15}
$$

2.4.4 Outer AC Voltage Control Loop

As mentioned in Section 2.2, an outer AC voltage control loop, as shown in Fig. 2.15, is necessary when the microgrid is in islanded mode. A PI-controller, with k_{pvac} and k_{ivac} as proportional and integral gain, is utilized to create a reference current that ensures that the AC voltage follows its reference. The input of the PI-controller is the dq-frame error between reference PCC voltage, $v_{o,ref}$, and actual PCC voltage, v_o, while the output is the reference dq-frame inductance current $i_{l,ref}$ which is sent as input to the inner current control loop (ICC).

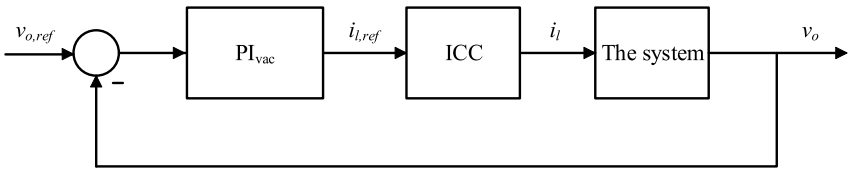

Figure 2.15: Outer AC voltage control loop.

The inner current controller is now represented in dq-frame by the first order transfer function in (2.16), where the time constant $\tau_{eq} = 2\tau_a$.

$$\frac{i_l^{dq}(s)}{i_{l,ref}^{dq}(s)} = \frac{1}{1 + s\tau_{eq}} \tag{2.16}$$

To find the system transfer function, Kirchhoff's current law (KCL) is applied to the node that connects the filter capacitance, C_f, as in (2.17).

$$\begin{aligned} i_{C_f d} &= i_{ld} - i_{od} \\ i_{C_f q} &= i_{lq} - i_{oq} \end{aligned} \tag{2.17}$$

The current across the capacitor is given as in (2.18). The d- and q-axis equations are cross coupled by the terms, $\omega_g C_f v_{od}$ and $\omega_g C_f v_{oq}$.

$$\begin{aligned} i_{C_f d} &= C_f \frac{dv_{oq}}{dt} - \omega_g C_f v_{od} \\ i_{C_f q} &= C_f \frac{dv_{oq}}{dt} + \omega_g C_f v_{od} \end{aligned} \tag{2.18}$$

By combining (2.17) and (2.18), the pu representation of the d- and q-axis system equations are given in (2.19) where $C_{f,pu} = \omega_b C_f Z_b$.

$$\begin{aligned} i_{ld,pu} - \underbrace{i_{od,pu}}_{\text{Feed-forward}} &= \frac{C_f}{\omega_b}\frac{dv_{oq,pu}}{dt} - \underbrace{\omega_{g,pu} C_{f,pu} v_{od,pu}}_{\text{Feed-forward}} \\ i_{lq,pu} - \underbrace{i_{oq,pu}}_{\text{Feed-forward}} &= \frac{C_{f,pu}}{\omega_b}\frac{dv_{oq,pu}}{dt} + \underbrace{\omega_{g,pu} C_{f,pu} v_{od,pu}}_{\text{Feed-forward}} \end{aligned} \tag{2.19}$$

Feed-forward of the cross-coupling terms and PCC current as illustrated in Fig 2.16 is utilized to decouple the equations. The system can now be described as in (2.20), where τ_v is the system time constant.

$$\frac{v_o^{dq}(s)}{i_l^{sq}(s)} = \frac{1}{s\tau_v}, \qquad \tau_v = \frac{C_{f,pu}}{\omega_b} \tag{2.20}$$

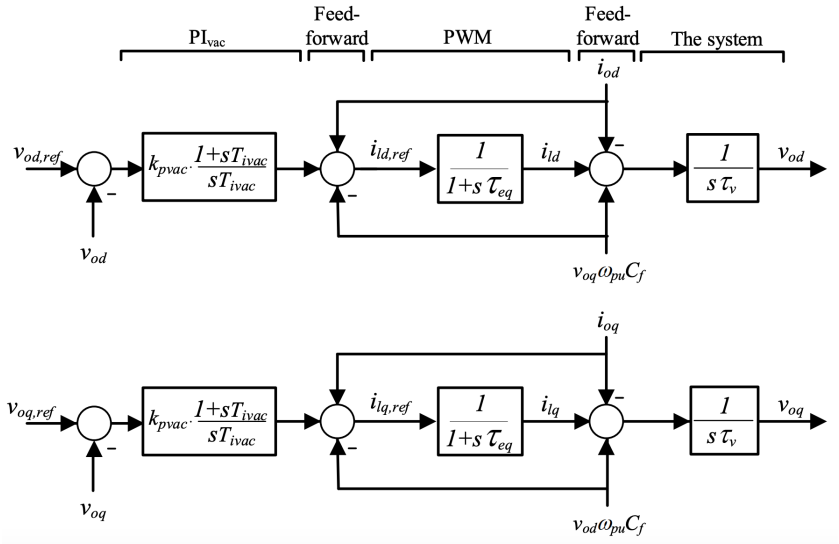

Figure 2.16: Outer AC voltage control loop.

2.4.5 Tuning

Because of simplicity and fast response, modulus optimum is used to tune the inner current control loop [52]. The goal of this method is to keep the closed loop transfer function, $G_{cl}(s)$, equal to 1 with no overshoot for a frequency as high as possible. Fig. 2.17 illustrates the fact that the closed loop transfer function must be one for the current to follow its reference.

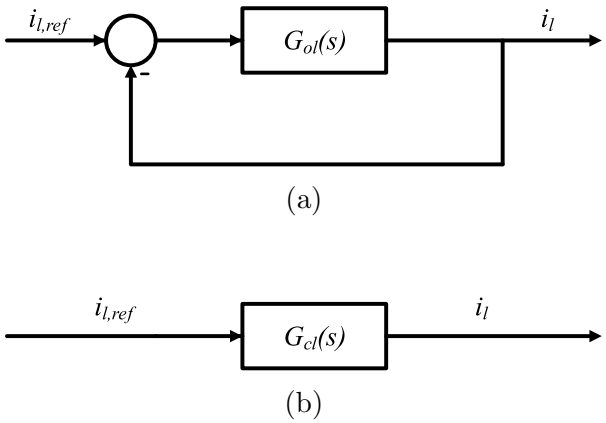

Figure 2.17: (a) Closed loop transfer function and (b) open loop transfer function of the inner control loop.

The requirements of modulus optimum is that the system has one dominant time constant and zero poles in the origin [18]. The dominant time constant will be the one of the physical system, τ_{pu}. Using Fig. 2.13, the open loop transfer function is found in (2.21).

$$G_{ol}(s) = \underbrace{\left(k_{pc}(\frac{1+sT_{ic}}{sT_{ic}})\right)}_{\text{PI}_\text{c}} \cdot \underbrace{\left(\frac{1}{1+s\tau_a}\right)}_{\text{PWM}} \cdot \underbrace{\left(\frac{1}{R_{c,pu}} \cdot \frac{1}{1+s\tau_{pu}}\right)}_{\text{The system}} \tag{2.21}$$

The controller zero of the PI-controller can be used to cancel out the dominant pole of the system. When $T_i = \tau_{pu}$, the simplified open loop transfer function is given in (2.22) and the corresponding closed loop transfer function is given in (2.23).

$$G_{ol}(s) = \frac{k_{pc}}{\tau_{pu}R_{c,pu}} \cdot \frac{1}{s(1+s\tau_a)} \tag{2.22}$$

$$G_{cl}(s) = \frac{G_{ol}(s)}{1+G_{ol}(s)} = \frac{\frac{k_{pc}}{\tau_{pu}\tau_a R_{c,pu}}}{s^2 + \frac{1}{\tau_a}s + \frac{k_{pc}}{\tau_{pu}\tau_a R_{c,pu}}} \tag{2.23}$$

Due to the cancellation of the system pole, the closed loop transfer function is a second order transfer function with the characteristic equation of $s^s + 2\zeta\omega_n s + \omega_n^2 = 0$. The natural frequency, ω_n and the damping factor ζ is given in (2.24).

$$\omega_n = \sqrt{\frac{k_{pc}}{\tau_{pu}\tau_a R_{c,pu}}}, \qquad \zeta = \frac{1}{2}\sqrt{\frac{\tau_{pu}R_{c,pu}}{k_{pc}\tau_a}} \tag{2.24}$$

The condition to achieve maximum flatness of $G_{cl}(s)$ is that $\zeta = \frac{1}{\sqrt{2}}$, which gives PI-controller parameters as expressed in (2.25).

$$k_{pc} = \frac{\tau_{pu}R_{c,pu}}{2\tau_a}, \qquad T_i = \tau_{pu} \tag{2.25}$$

The control parameters of the outer AC voltage control loop are found by trial and error method and are together with the inner current control loop parameters given in Table 2.3.

Table 2.3: Control system parameters.

Parameter	Value
k_{pc}	2.55 pu
k_{ic}	40 pu
k_{pvac}	0.1 pu
k_{ivac}	20 pu

The open loop transfer function of the outer AC voltage controller can be found according to the block diagram in Fig. 2.15, and is given in (2.26).

$$G_{ol}(s) = \underbrace{\left(k_{pvac}(\frac{1+sT_{ivac}}{sT_{ivac}})\right)}_{\text{PI}_\text{vac}} \cdot \underbrace{\left(\frac{1}{1+s\tau_{eq}}\right)}_{\text{ICC}} \cdot \underbrace{\left(\frac{C_{f,pu}}{\omega_b}\right)}_{\text{The system}} \tag{2.26}$$

Fig. 2.18a shows the Bode plot of the open loop transfer function of the current control loop and AC voltage control loop for the given control parameters. The crossover frequency of the inner current controller is at 1159 Hz, which is 7 times smaller than the converter's switching frequency and an acceptable ratio. The phase margin is 65.5° and the gain margin is infinite which indicate stable operations. The crossover frequency of the outer AC voltage loop is 267 Hz. This makes it approximately 4 times faster than the inner current control loop, which is desirable.

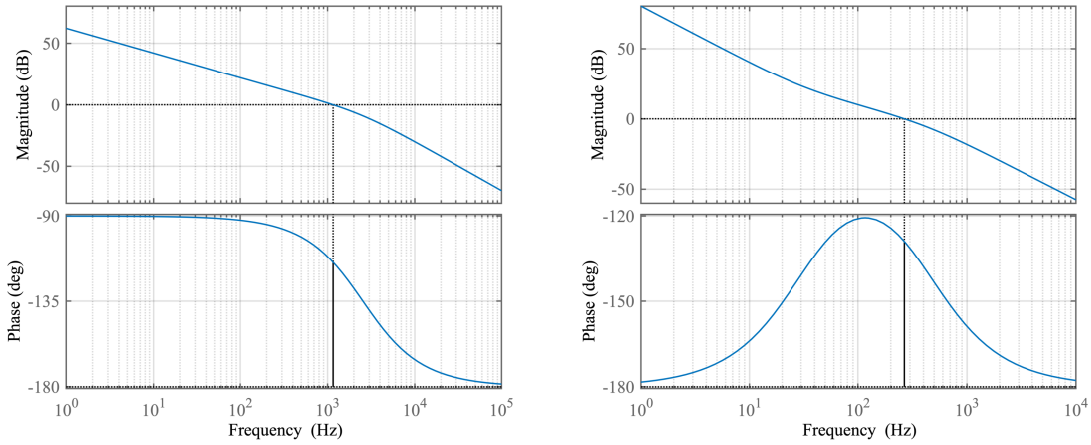

(a) (b)

Figure 2.18: Bode plot of the open loop transfer function of (a) inner current controller and (b) outer AC voltage controller.

2.4.6 Control of the Current Contolled VSC

The complete control system in pu of a current controlled VSC is shown in Fig. 2.19. In order to deliver power to the grid, a PLL is used to track the actual grid frequency and a current controller is used to enable that the system follows the current reference. m_d and m_q are the modulation indexes obtained from the current controller which are given as inputs to the PWM.

Fig. 2.20 shows time domain simulations of the presented current controlled VSC. A step in the d-axis reference current is applied after 0.5 seconds from 0.8 to 1.0 pu. Fig. 2.20a shows how the three-phase grid currents and PCC voltages reacts to this change. The voltage stays constant through the change except some small disturbances at the time when the reference current changes. Fig. 2.20b shows that the d- and q-axis currents are able to follow its reference without any overdamped or underdamped characteristics.

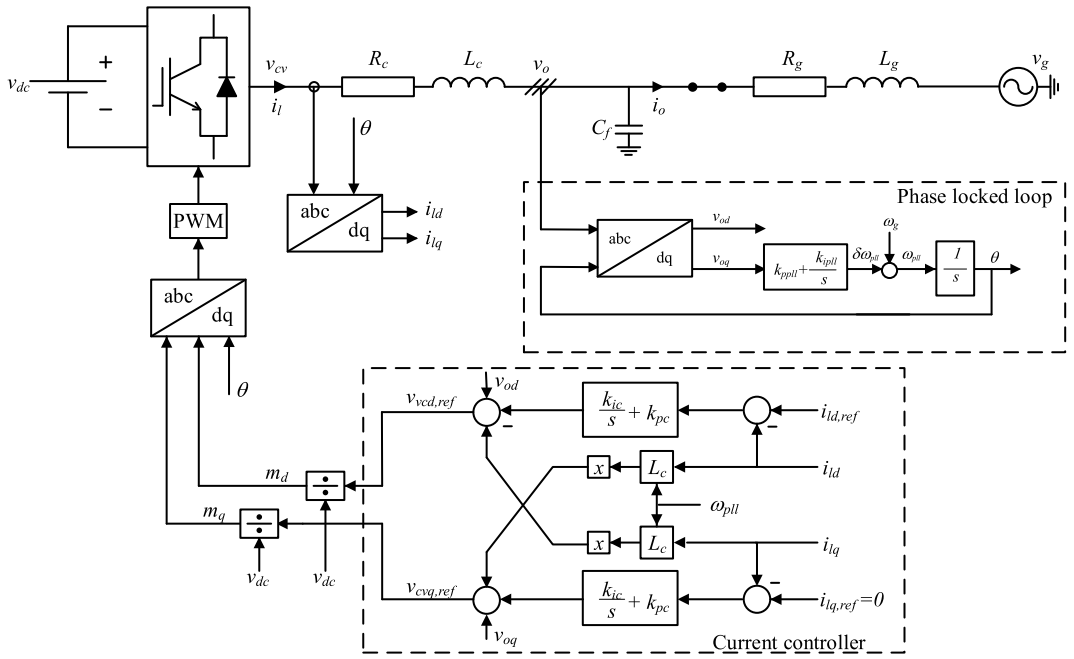

Figure 2.19: Control system of a current controlled VSC.

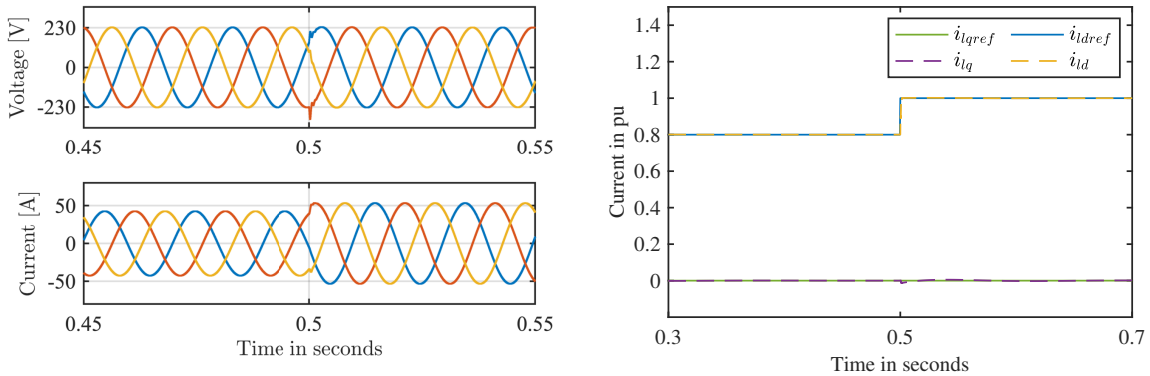

(a) (b)

Figure 2.20: Time domain simulations of (a) three-phase voltages and currents and (b) d- and q-axis currents of the current controlled VSC.

2.4.7 Control of the AC Voltage Controlled VSC

The control principle of the AC voltage controlled VSC is depicted in Fig. 2.21. An outer-loop AC voltage controller is now added to create the reference current input of the current controller [53]. Because the grid is decoupled a PLL is not expedient and is replaced with a simple block that obtains the phase angle of the voltage by integrating the base of the grid frequency [23].

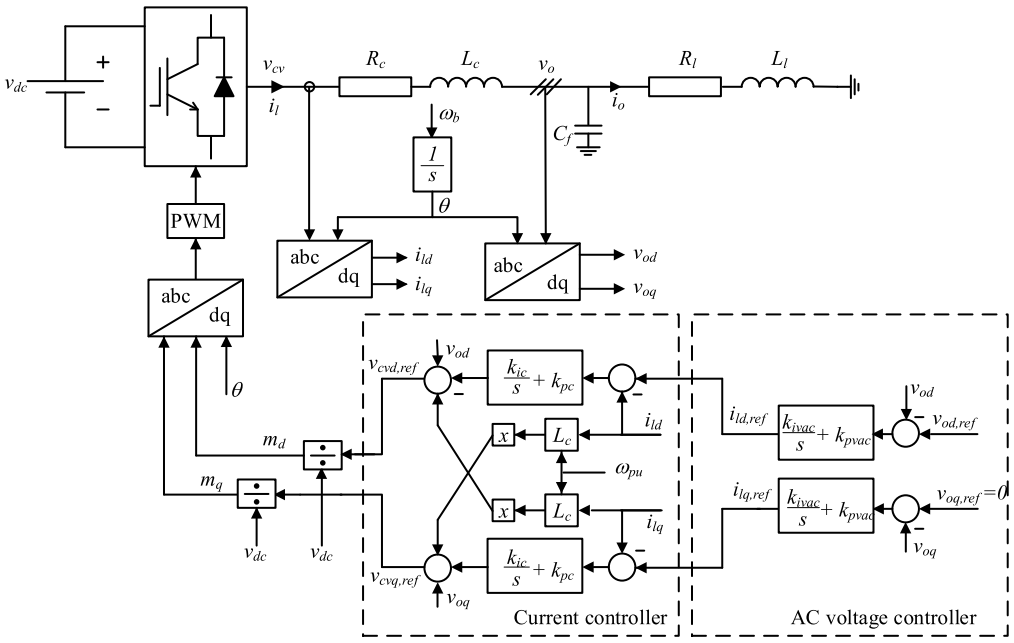

Figure 2.21: Control system of an AC voltage controlled VSC.

Fig. 2.22 shows the time domain simulations of the AC voltage controlled VSC. At 0.5 seconds a step in the voltage reference from 0.9 to 1.0 pu is applied. Fig. 2.22a shows how the three-phase grid currents and PCC voltages, i_o and v_o, react to this change. The voltage has a 0.1 pu change at 0.5 seconds and to set this voltage there must also be a change in the current. The quick step response is further confirmed by Fig. 2.22b.

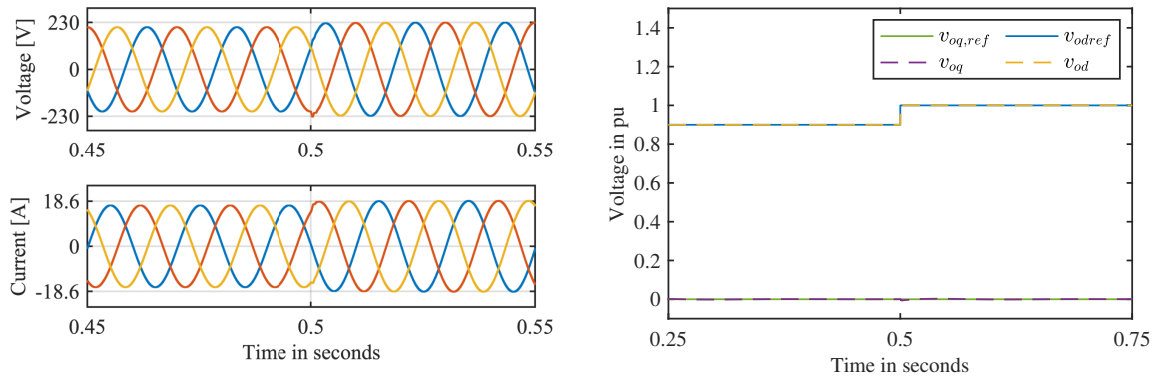

(a) (b)

Figure 2.22: Time domain simulations of (a) three-phase voltages and currents and (b) d- and q-axis currents of the AC voltage controlled VSC.

2.5 Control of the Microgrid

Sections 2.3 and 2.4 have thoroughly reviewed modeling and control of a single VSC based on both a current controlled and an AC voltage controlled control strategy. By

combining this information with Section 2.2, that went through the model description of a microgrid, it is possible to explain the control of the microgrid operating in both grid-connected and islanded mode.

As previously mentioned, the grid-connected microgrid does consist of only current controlled VSCs. However, when the microgrid is operated in islanded mode, it is necessary with one AC voltage controlled VSC because of the absence of the main grid. Appendix C shows the Simulink model of the presented microgrid, where it can be observed how the switching between the two control strategies are implemented.

The pu value of the reference current input of the current controller for the different VSCs are given in Table 2.4. A positive reference current represents a generator, while a negative reference current represents a load. A current reference of -0.2 pu for the BESS therefore means that the battery is charging when it is in grid-connected mode. However, as is illustrated in the next subsection, this will change when the microgrid is islanded. In Chapter 5 the stability of the system when introducing a variable power input due to intermittent solar and wind power is analyzed, but for the simulations below it is assumed that all the microsources and loads produce or consume a constant amount of power according to the table.

Table 2.4: Reference current input of each current controller.

Parameter	Value
$i_{ldref,pv}$	0.4 pu
$i_{ldref,wind}$	0.2 pu
$i_{ldref,ig}$	-0.7 pu
$i_{ldref,bess}$	-0.2 pu

2.5.1 Simulations of the Microgrid

Time domain simulations of the grid currents and PCC voltages, i_o and v_o, of the microgrid are shown in Fig. 2.23. It can be observed that the microgrid is operated at current and voltage values of 1.0 pu which is equivalent to 53.3 A and 230 V. Fig. 2.23a shows the three-phase currents and voltages when the microgrid switches from grid-connected to islanded mode after 1.0 second. The grid current stays constant before it becomes zero when the grid is decoupled, while the voltage experiences some small deviations at the point of decoupling before it goes back to normal.

Fig. 2.23b shows the time domain simulations of how the microgrid reacts to the change from islanded to grid-connected mode. In this case, the grid current is zero until the grid is connected, while the voltage stays constant through the switching between the different modes. The current respond quickly to the connection of the grid and reaches the correct value after a short amount of time.

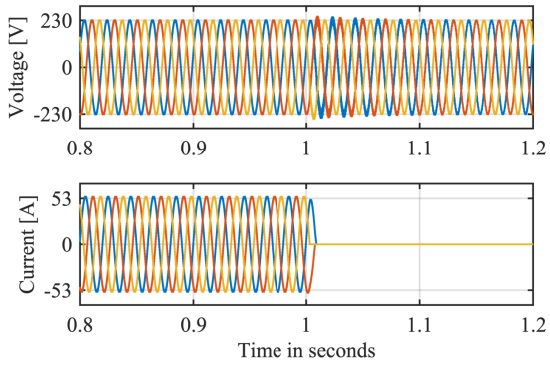

(a)

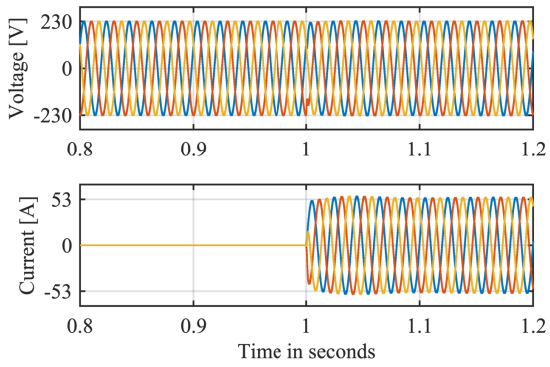

(b)

Figure 2.23: Time domain simulations of grid currents and PCC voltages in the change from: (a) grid-connected to islanded mode, (b) islanded to grid-connected mode.

Since the BESS is changing between two control modes it is interesting to see how it operates differently in grid-connected and islanded mode. Fig. 2.24a shows the three-phase currents and voltages at the PCC of the BESS when the microgrid changes from grid-connected to islanded mode at 1.0 second. This corresponds to a change from current controlled to an AC voltage controlled control strategy for the BESS. The voltage experiences a little drop, before it quickly restores its value. The current of the BESS first follows the reference value of -0.2 pu. However, when the grid is disconnected, the current is increased to 0.85 pu to meet the power demand and to ensure that the voltage remains at the correct level. This means that in islanded mode, the battery is charging or discharging depending on what is necessary to maintain the correct PCC voltage. The three-phase current is stable through the change, but needs some time before it reaches the final value.

Fig. 2.24b, on the other hand, shows the time domain simulations of the three-phase voltages and currents at the PCC of the BESS when the microgrid changes from islanded to grid-connected mode. It can be observed that the change from islanded to grid-connected mode is faster and smoother than the other way around. The voltage is unaffected by the change in operation mode, and the current reaches the reference value of -0.2 pu immediately.

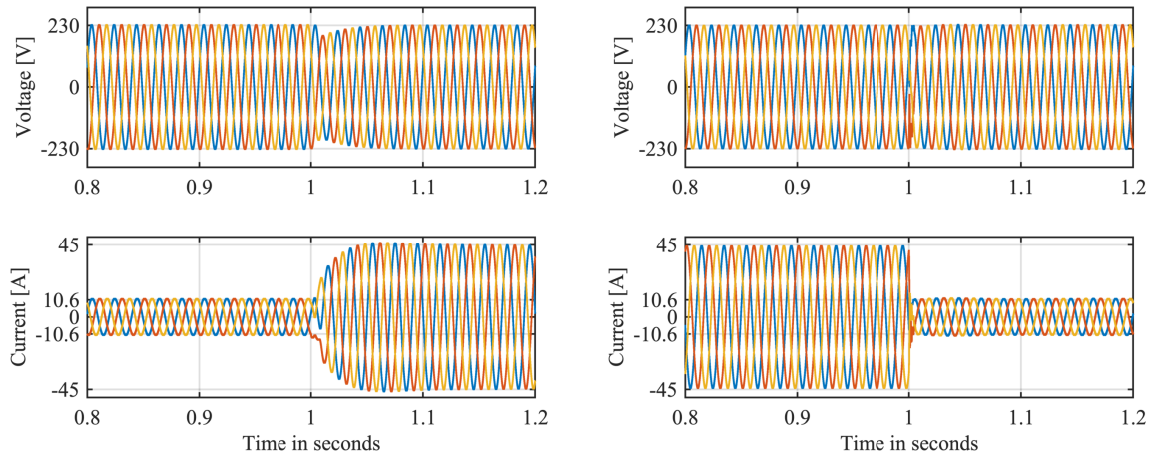

Figure 2.24: Time domain simulations of PCC currents and voltages of the BESS in the change from: (a) current controlled to AC voltage controlled strategy and (b) AC voltage controlled to current controlled strategy.

Lastly, it is interesting to see how the other converters manage through the change between the two microgrid operating modes. Fig. 2.25 shows the PCC currents and voltages of the IG when the microgrid changes from islanded to grid-connected mode, and as can be observed the voltage stays undisturbed through the change, and the current follows its reference of -0.7 pu.

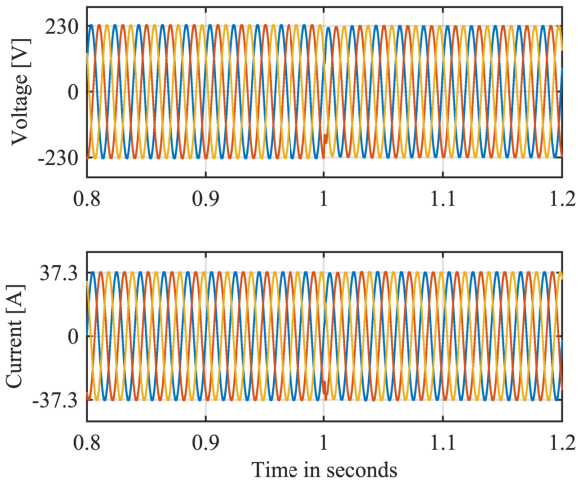

Figure 2.25: Three-phase PCC currents and voltages for the IG.

Chapter 3

Small-Signal State-Space Modeling of the VSC

This chapter will derive a nonlinear state-space model in pu of the VSC described in Chapter 2. By presenting a mathematical model of the physical system, the current controller, the AC voltage controller and the PLL, all the states, inputs and outputs will be discussed. Following, a small-signal representation of the state-space model is found to be able to apply stability assessments based on linear techniques. Lastly, the linearized model is validated through comparison with a simulated model that includes the nonlinear characteristics of the system.

3.1 Introduction

Chapter 1 described many of the advantages of a power electronics dominated power system. However, in addition to achieve an even more controllable and effective power system, integration of power electronics brings several new challenges regarding power stability and quality. There exists several different methods to analyze the stability of a power electronics dominated system. However, a common characteristic of a large proportion of these methods is that they require a linearized model of the system to analyze the stability.

Fig. 3.1 illustrates the concept of linearization, which is to find the linear approximation to a function at a given point. The function $f(x)$ is linearized around an operating point, x, by its derivative $f'(x)$. As can be seen from the figure the linearization approximate the function around the operating point, but becomes inaccurate when the distance to x increases.

To linearize a given system, a state-space model is first found analytically in the dq-frame. For a power electronics dominated system, this model includes both the control loops and dynamics of the system [54]. The state-space model represents the system

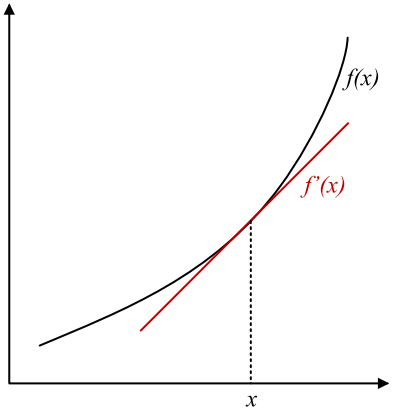

Figure 3.1: Illustration of linearization.

through a set of first order nonlinear differential equations, expressed by state variables, inputs and outputs as in (3.1), where $x(t)$ is the state vector and $u(t)$ is the input vector. State variables are introduced by the derivatives of the control system, currents across inductors and voltages across capacitors. The set of states of a dynamic system is the set of variables that is necessary to describe the system and determine the future behavior.

$$\begin{aligned} \frac{dx}{dt} &= f\big(x(t), u(t)\big) \\ y &= g\big(x(t), u(t)\big) \end{aligned} \tag{3.1}$$

The same principles of linearization, as illustrated in Fig. 3.1, apply for a system consisting of a function set with multiple variables. However, since more than one variable exist, a single derivative is not enough to linearize the system and the multi-variable equivalent of the derivative, the Jacobian, must be used. The Jacobian matrix, $\mathbf{J}$, given in (3.2) is a matrix consisting of the derivatives of the function set with respect to all the existing states in the system. As in the illustrative case, the Jacobian must be assessed at a point of operation. In multi-variable systems this point is known as the steady-state values of the differential equations and are found by setting all the differential equations to zero. It is not possible to find steady-state values for a three-phase AC system, which emphasizes the reason why two constant d- and q-signals in SRF are advantageous. If the matrix is multiplied with a certain state vector with small magnitudes the product can approximate the nonlinear system [55]. Generally, the product will determine the small-signal behavior around the operating point.

$$\mathbf{J} = \begin{bmatrix} \dfrac{\partial \mathbf{f}}{\partial x_1} & \cdots & \dfrac{\partial \mathbf{f}}{\partial x_n} \end{bmatrix} = \begin{bmatrix} \frac{\partial f_1}{\partial x_1} & \cdots & \frac{\partial f_1}{\partial x_n} \\ \vdots & \ddots & \vdots \\ \frac{\partial f_m}{\partial x_1} & \cdots & \frac{\partial f_m}{\partial x_n} \end{bmatrix} \tag{3.2}$$

The physical system is not only affected by the states, but also from external inputs, u. The equation governing these relations must also be included. They can also be

nonlinear and must be linearized with the Jacobian as well, but with respect to the input variables. The product of this new Jacobian matrix and the input vector determines the linearization of any input dynamics. Adding this product with the state product above models the complete dynamic behavior of the linearly approximated system as shown in (3.3). Δ indicates the small-signal deviation around the steady-state operating point, $\Delta_x f$ represents the Jacobian matrix of f with respect to the states, x, and $\Delta_u f$ represents the Jacobian matrix of f with respect to the inputs ,u.

$$\begin{aligned} \frac{d\Delta x}{dt} &= A\Delta x + B\Delta u \\ A = \Delta_x f, &\quad B = \Delta_u f \end{aligned} \tag{3.3}$$

Additional matrices C and D can be used to determine what the outputs of the system should be as shown in (3.4), where $\Delta_x g$ represents the Jacobian matrix of g with respect to the states, x, and $\Delta_u g$ represents the Jacobian matrix of g with respect to the inputs ,u.

$$\begin{aligned} \Delta y &= C\Delta x + D\Delta u \\ C = \Delta_x g, &\quad D = \Delta_u g \end{aligned} \tag{3.4}$$

Deriving the small-signal state-space model is expedient for two reasons. First, it is necessary to know the steady-state values of the state to derive the impedance models of the VSC, which is a prerequisite to apply the impedance-based stability analysis. Secondly, it is important to verify the small-signal steady-state model by comparing it to the nonlinear model before proceeding the stability analysis.

This Chapter presents the small-signal state-space model of the VSC discussed in Chapter 2. Section 3.2 first introduces the states of the dynamic equations of the physical system, before the states of the PLL are introduced. Furthermore, the states of the current controller and AC voltage controller are introduced. A small-signal state-space matrix is now derived for both control modes of the VSC in Section 3.3. Section 3.4 presents the time domain comparison between the state-space linearized model and the nonlinear model. Lastly, in Section 3.5, the eigenvalue-based stability analysis is applied to confirm the stability of the original systems and to illustrate how the stability is affected by changing system and control parameters.

3.2 State-Space Modeling of the VSC

In this section the per unit state-space modeling of the VSC in Fig. 3.2, including control systems, will be found analytically.

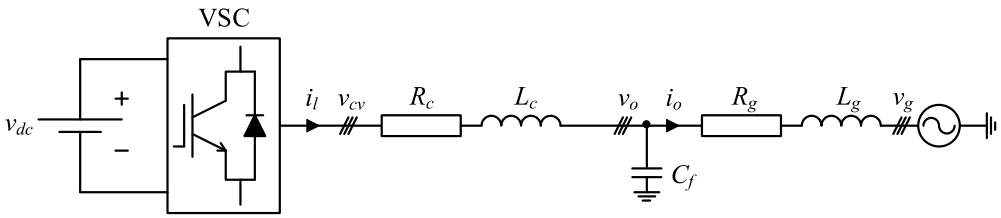

Figure 3.2: Overview of the VSC.

3.2.1 Dynamic Equations of the VSC

First, the analytical equations of the physical system are found. As mentioned in the introduction, state variables of the physical system is introduced by currents across inductors and voltages across capacitors. For the VSC in Fig. 3.2, the states are introduced by the filter inductance, L_c, the filter capacitor, C_f, and the grid inductance, L_g, which result in three states. However, since the modeling, control and analysis of the system is presented in SRF every state has one d- and one q-axis component, and the resulting number of states of the physical system is changed to six. Following the same procedure as in [56], and using Fig. 3.3 the analytical equations describing the physical system are found.

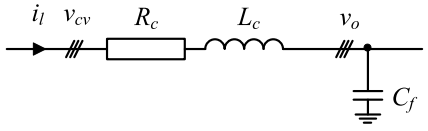

(a)

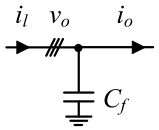

(b)

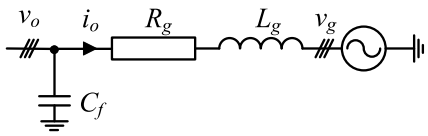

(c)

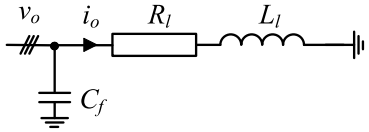

(d)

Figure 3.3: (a), (b) and (c) are used to find converter, filter, and grid equations, respectively and (d) is used to find the grid equations when the grid is disconnected.

KVL is applied on Fig. 3.3a, to find the states of the currents across L_c. The converter equations are given in pu by (3.5) and introduces the two inductor current states, i_{ld} and i_{lq}.

$$\begin{aligned}\frac{di_{ld,pu}}{dt} &= \frac{\omega_b}{L_{c,pu}}v_{cvd,pu} - \frac{\omega_b}{L_{c,pu}}v_{od,pu} + \omega_{g,pu}\omega_b i_{lq,pu} - \frac{\omega_b R_{c,pu}}{L_{c,pu}}i_{ld,pu} \\ \frac{di_{lq,pu}}{dt} &= \frac{\omega_b}{L_{c,pu}}v_{cvq,pu} - \frac{\omega_b}{L_{c,pu}}v_{oq,pu} - \omega_{g,pu}\omega_b i_{ld,pu} - \frac{\omega_b R_{c,pu}}{L_{c,pu}}i_{lq,pu}\end{aligned} \tag{3.5}$$

To express the states of the filter capacitor, C_f, KCL is applied on Fig. 3.3b. Equation (3.6) gives the filter equations of the two states, v_{od} and v_{oq}, in pu.

$$\begin{aligned}\frac{dv_{od,pu}}{dt} &= \frac{\omega_b}{C_{f,pu}}i_{ld,pu} - \frac{\omega_b}{C_{f,pu}}i_{od,pu} + \omega_{g,pu}\omega_b v_{oq,pu} \\ \frac{dv_{oq,pu}}{dt} &= \frac{\omega_b}{C_{f,pu}}i_{lq,pu} - \frac{\omega_b}{C_{f,pu}}i_{oq,pu} - \omega_{g,pu}\omega_b v_{od,pu}\end{aligned} \tag{3.6}$$

KVL is applied to Fig. 3.3c to find the AC grid equations in pu given in (3.7). This introduces the two states, i_{od} and i_{oq}.

$$\begin{aligned}\frac{di_{od,pu}}{dt} &= \frac{\omega_b}{L_{g,pu}}v_{od,pu} - \frac{\omega_b}{L_{g,pu}}v_{gd,pu} + \omega_{g,pu}\omega_b i_{oq,pu} - \frac{\omega_b R_{g,pu}}{L_{g,pu}}i_{od,pu} \\ \frac{di_{oq,pu}}{dt} &= \frac{\omega_b}{L_{g,pu}}v_{oq,pu} - \frac{\omega_b}{L_{g,pu}}v_{gq,pu} - \omega_{g,pu}\omega_b i_{od,pu} - \frac{\omega_b R_{g,pu}}{L_{g,pu}}i_{oq,pu}\end{aligned} \tag{3.7}$$

However, when the grid is disconnected and the VSC utilize the AC voltage controlled strategy, Fig. 3.3d is used. R_l and L_l is now obtaining the voltage level and the equations representing the states i_{od} and i_{oq} are given by (3.8).

$$\begin{aligned}\frac{di_{od,pu}}{dt} &= \frac{\omega_b}{L_{l,pu}}v_{od,pu} + \omega_{g,pu}\omega_b i_{oq,pu} - \frac{\omega_b R_{l,pu}}{L_{l,pu}}i_{od,pu} \\ \frac{di_{oq,pu}}{dt} &= \frac{\omega_b}{L_{l,pu}}v_{oq,pu} - \omega_{g,pu}\omega_b i_{od,pu} - \frac{\omega_b R_{l,pu}}{L_{l,pu}}i_{oq,pu}\end{aligned} \tag{3.8}$$

3.2.2 Phase Locked Loop

The PLL has already been discussed in Chapter 2. However, the block diagram in Fig. 3.4 is modified to simpler illustrate the introduction of states. The PLL introduces two states, where the PI-controller introduces one and the integrator introduces the other.

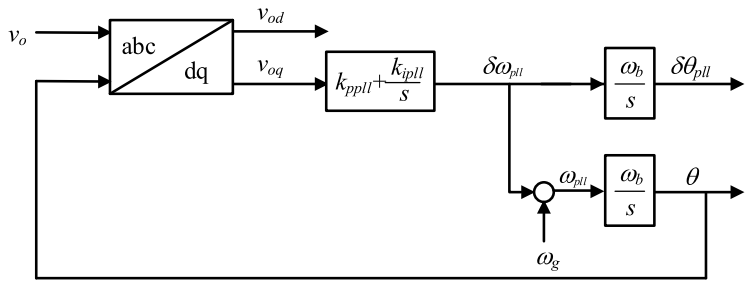

Figure 3.4: Block diagram of phase locked loop.

$\delta\omega_{pll}$ is the output of the PI-controller and represents the speed deviation with respect to the grid frequency and is given by (3.9). The ε_{pll} term represents the integrator state introduced by the PI-controller and is given in (3.10).

$$\delta\omega_{pll} = k_{ppll}v_{oq} + k_{ipll}\varepsilon_{pll} \tag{3.9}$$

$$\frac{d\varepsilon_{pll}}{dt} = v_{oq} \tag{3.10}$$

$\delta\theta_{pll}$ describes the phase angle deviation between the grid voltage and the orientation of the PLL. It represents the second state and is introduced by the integrator as in (3.11).

$$\frac{d\delta\theta_{pll}}{dt} = \delta\omega_{pll}\omega_b = \omega_b(k_{ppll}v_{oq} + k_{ipll}\varepsilon_{pll}) \tag{3.11}$$

The grid voltage can be transformed into PLL reference frame as in (3.12), where $\hat{v}_g$ is the amplitude value.

$$v_g = \hat{v}_g e^{j\delta\theta_{pll}} \tag{3.12}$$

While $\delta\theta_{pll}$ and $\delta\omega_{pll}$ are necessary to model the system in SRF, the actual frequency of the PLL, ω_{pll}, given by (3.13) is needed to transform from stationary to SRF in the actual control system.

$$\omega_{pll} = \delta\omega_{pll} + \omega_g \tag{3.13}$$

3.2.3 Current Controller

Fig. 3.5 shows the block diagram of the inner current control loop. The figure is used to express the output of the current controller as in (3.14). The converter output voltage reference introduces no states, but is necessary as an input of the converter equations presented in (3.5).

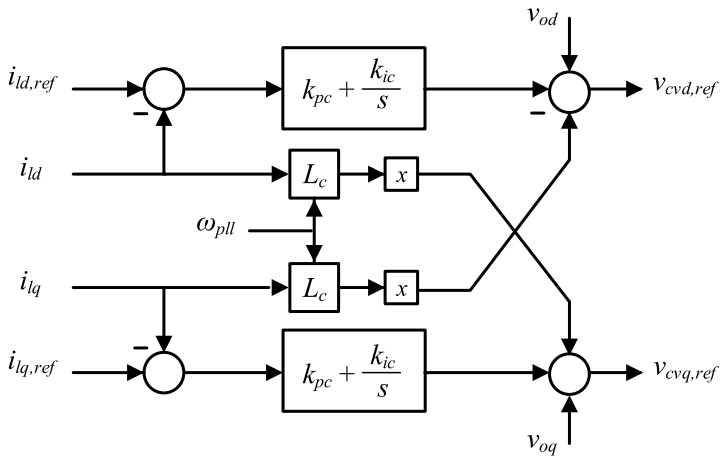

Figure 3.5: Block diagram of current controller.

$$\begin{aligned} v_{cvd,ref} &= (i_{ld,ref} - i_{ld})k_{pc} + \gamma_d k_{ic} - \omega_{pll} L_c i_{lq} + v_{od} \\ v_{cvq,ref} &= (i_{lq,ref} - i_{lq})k_{pc} + \gamma_q k_{ic} + \omega_{pll} L_c i_{ld} + v_{oq} \end{aligned} \tag{3.14}$$

Lastly, the integrator of the PI-controller introduces the two states of the current controller which is represented by γ_d and γ_q as in (3.15).

$$\begin{aligned} \frac{d\gamma_d}{dt} &= i_{ld,ref} - i_{ld} \\ \frac{d\gamma_q}{dt} &= i_{lq,ref} - i_{lq} \end{aligned} \tag{3.15}$$

3.2.4 AC Voltage Controller

As mentioned in Chapter 2, an AC voltage control strategy as shown in Fig. 3.6 is necessary when decoupling the grid.

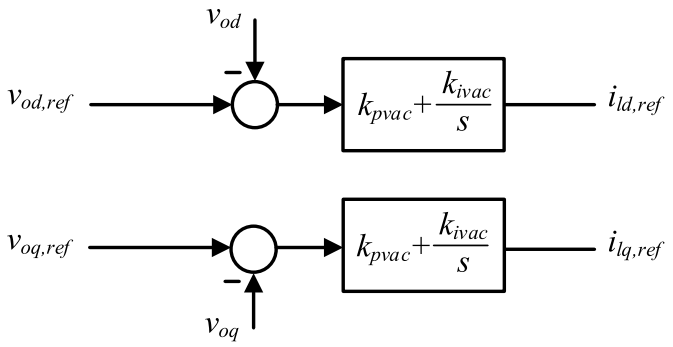

Figure 3.6: Block diagram of AC voltage controller.

The outputs of the AC voltage control, $i_{ld,ref}$ and $i_{lq,ref}$, are given in (3.16) and are the input of the current controller discussed above. This equation introduces no states, but is necessary as an input of the current controller states in (3.15).

$$\begin{aligned} i_{ld,ref} &= (v_{od,ref} - v_{od})k_{pvac} + \alpha_d k_{ivac} \\ i_{lq,ref} &= (v_{oq,ref} - v_{oq})k_{pvac} + \alpha_q k_{ivac} \end{aligned} \tag{3.16}$$

The integrator of the PI-controller introduces two states which are represented by α_d and α_q as in (3.17) [57].

$$\begin{aligned} \frac{d\alpha_d}{dt} &= v_{od,ref} - v_{od} \\ \frac{d\alpha_q}{dt} &= v_{oq,ref} - v_{oq} \end{aligned} \tag{3.17}$$

3.3 Small-Signal State-Space Matrix Realization

The steady-state operating point of the system is found by putting all the nonlinear differential equations to zero. By linearizing the system using the Jacobian as described in Section 3.1 a small-signal state-space model is derived. This model will approximate the nonlinear state-space system around magnitudes close to the steady-state operating point. As expressed in (3.3) and (3.4) the linearized system can be expressed by the matrices A and B. The A matrix is the Jacobian matrix of f with respect to all the states, x. f represents all the state-space equations, and there are as many state-space equations as there are states. This means that if the number of states are n, the A matrix would be a $n \times n$-matrix. The physical system is also affected by the external inputs, u. The B-matrix is therefore the Jacobian matrix of f with respect to all inputs, u. If the number of input is m, the B-matrix would be a $n \times m$-matrix. The A- and B-matrix are given in (3.18).

$$A = \begin{bmatrix} \frac{\partial f_1}{\partial x_1} & \cdots & \frac{\partial f_1}{\partial x_n} \\ \vdots & \ddots & \vdots \\ \frac{\partial f_n}{\partial x_1} & \cdots & \frac{\partial f_n}{\partial x_n} \end{bmatrix}, \qquad B = \begin{bmatrix} \frac{\partial f_1}{\partial x_1} & \cdots & \frac{\partial f_1}{\partial x_m} \\ \vdots & \ddots & \vdots \\ \frac{\partial f_n}{\partial x_1} & \cdots & \frac{\partial f_n}{\partial x_m} \end{bmatrix} \tag{3.18}$$

Matrices C and D are used to determine the outputs of the system. The inputs are not interesting to look at so the D-matrix is a $n \times m$ zero-matrix. The C-matrix has zeroes on all non-diagonal elements, and ones on the diagonal elements that is expedient as output. The C-matrix is a $n \times n$-matrix, and if all of the outputs are desirable it equals the identity matrix. The form of the C- and D-matrix is given in (3.19).

$$C = \begin{bmatrix} 1 & 0 & 0 & \dots & 0 \\ 0 & 1 & 0 & \dots & 0 \\ 0 & 0 & 1 & \dots & 0 \\ \vdots & \vdots & \vdots & \ddots & \vdots \\ 0 & 0 & 0 & \dots & 1 \end{bmatrix}, \qquad D = \begin{bmatrix} 0 & 0 & \dots & 0 \\ 0 & 0 & \dots & 0 \\ \vdots & \vdots & \ddots & \vdots \\ 0 & 0 & \dots & 0 \end{bmatrix} \tag{3.19}$$

3.3.1 Current Controlled VSC

By combining equations (3.5) to (3.7) and (3.9) to (3.15) the state-space model of the current controlled VSC can be found as a set of nonlinear differential equations expressed by state variables, inputs and outputs on the form of (3.1) given in the introduction.

The state, x, and input, u, vector of the current controlled VSC are given in (3.20). The state vector includes all the states from the dynamic equations, the current controller and the PLL, while the input vector includes the reference inductance current, the amplitude of the grid voltage and the grid frequency. Matrix A and B of the resulting small-signal state-space model according to (3.18) are given in Appendix D.

$$\begin{gathered} x = \begin{bmatrix} v_{od} & v_{oq} & i_{ld} & i_{lq} & \gamma_d & \gamma_q & i_{od} & i_{oq} & \varepsilon_{pll} & \delta\theta_{pll} \end{bmatrix}^T \\ u = \begin{bmatrix} i_{ld,ref} & i_{lq,ref} & \hat{v}_g & \omega_g \end{bmatrix}^T \end{gathered} \tag{3.20}$$

3.3.2 AC Voltage Controlled VSC

By combining equations (3.5), (3.6), (3.8) and (3.14) to (3.17) the state-space model of the AC voltage controlled VSC can be found.

The states of the AC voltage controller, α_d and α_q, are included in the new state vector. However, the states introduced by the PI-controller, ε_{pll} and the integrator, $\delta\theta_{pll}$ of the PLL will disappear with an AC voltage controlled VSC. This is because the PLL, according to Fig. 2.21, is replaced with a simple block that obtains the phase angle of the voltage by integrating the base of the grid frequency. The input vector will now contain the inputs of the AC voltage controller, $v_{od,ref}$ and $v_{oq,ref}$. However, the amplitude of the grid voltage, $\hat{v}_g$, will no longer be a part of the input vector due to the fact that the grid is decoupled. The A and B matrix of the small-signal state-space model of the AC voltage controlled VSC are given in Appendix D.

$$\begin{gathered} x = \begin{bmatrix} v_{od} & v_{oq} & i_{ld} & i_{lq} & \gamma_d & \gamma_q & i_{od} & i_{oq} & \alpha_d & \alpha_q & \theta_{pll} \end{bmatrix}^T \\ u = \begin{bmatrix} v_{od,ref} & v_{oq,ref} & \omega_g \end{bmatrix}^T \end{gathered} \tag{3.21}$$

3.4 Small-Signal State-Space Model Verification

As mentioned in the introduction it is important to verify the linearized model with the nonlinear model. When the linearized model is verified it is possible to proceed with stability analysis of the system, and to use the steady-state values to derive the impedance models of the current controlled and AC voltage controlled VSC. In this section, the analytical small-signal state-space model is therefore validated through simulations of a detailed model of the system including nonlinear characteristics [58]. The detailed model of the current controlled VSC and AC voltage controlled VSC is given in Appendix C.

The comparison of the linearized and nonlinear model is completed in Simulink and the method of how the two models are compared to each other is illustrated in Fig. 3.7. The small-signal deviation around the steady-state point of the input, Δu, of the analytically derived model is sent through a state-space block. All the inputs are set to zero, except from one which experiences a small step-change to see the response of the model. The product of the state-space block is the small-signal deviation around the steady-state point of the output, Δy. To get the actual response that can be compared with the simulated nonlinear system, the output of the state-space block must be added with the steady-state operating value, $x_{n,0}$, of the same state. The same step-change in input parameter must be implemented to the simulated model. The output of the linearized state-space model and the nonlinear simulated model can now be compared by using a scope, as shown in the figure.

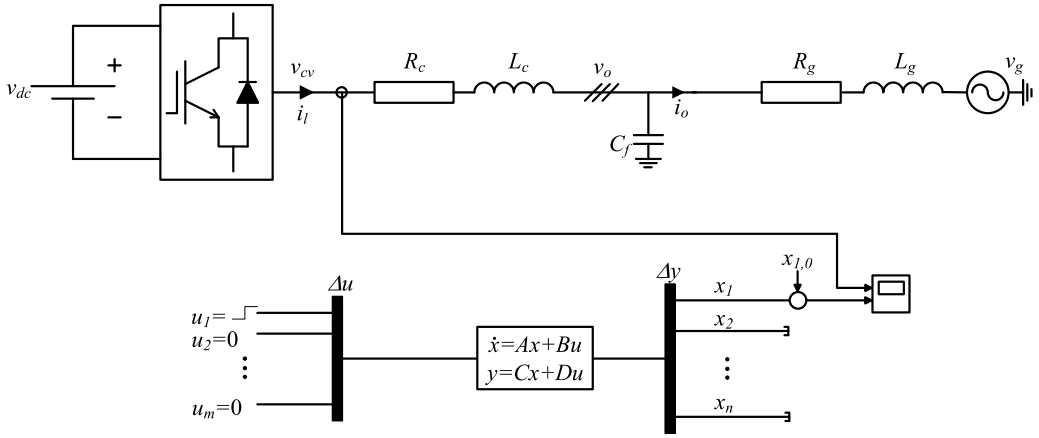

Figure 3.7: The method of model verification.

3.4.1 Current Controlled VSC

Fig. 3.8 shows the responses of the current controlled VSC for a 0.05 pu change in the d-axis current reference, $i_{ld,ref}$, from 0.5 to 0.55 pu. Fig. 3.8a and 3.8b shows the responses of d- and q-axis converter current. As can be observed the current i_{ld} follows its reference and increase from 0.5 to 0.55 pu, while the q-axis current i_{lq} stays constant

at zero unaffected by the step-change at 0.05 seconds.

The d-axis PCC voltage v_{od} in Fig. 3.8c oscillates around its desirable value, just above 1.0 pu, while the q-axis voltage, v_{oq}, in Fig. 3.8d oscillitates around the zero line. Common for both d- and q-axis voltages are that the oscillation created by the step change of the d-axis reference current does not quickly disappear. The grid currents, i_{od} and i_{oq}, in Fig. 3.8e and 3.8f has the same oscillations as the PCC voltage, but also they follow its reference.

However, the responses of the linearized model and the nonlinear model have no noticeable difference and the linearized model can therefore be used to correctly evaluate the stability of the system around the linearization point.

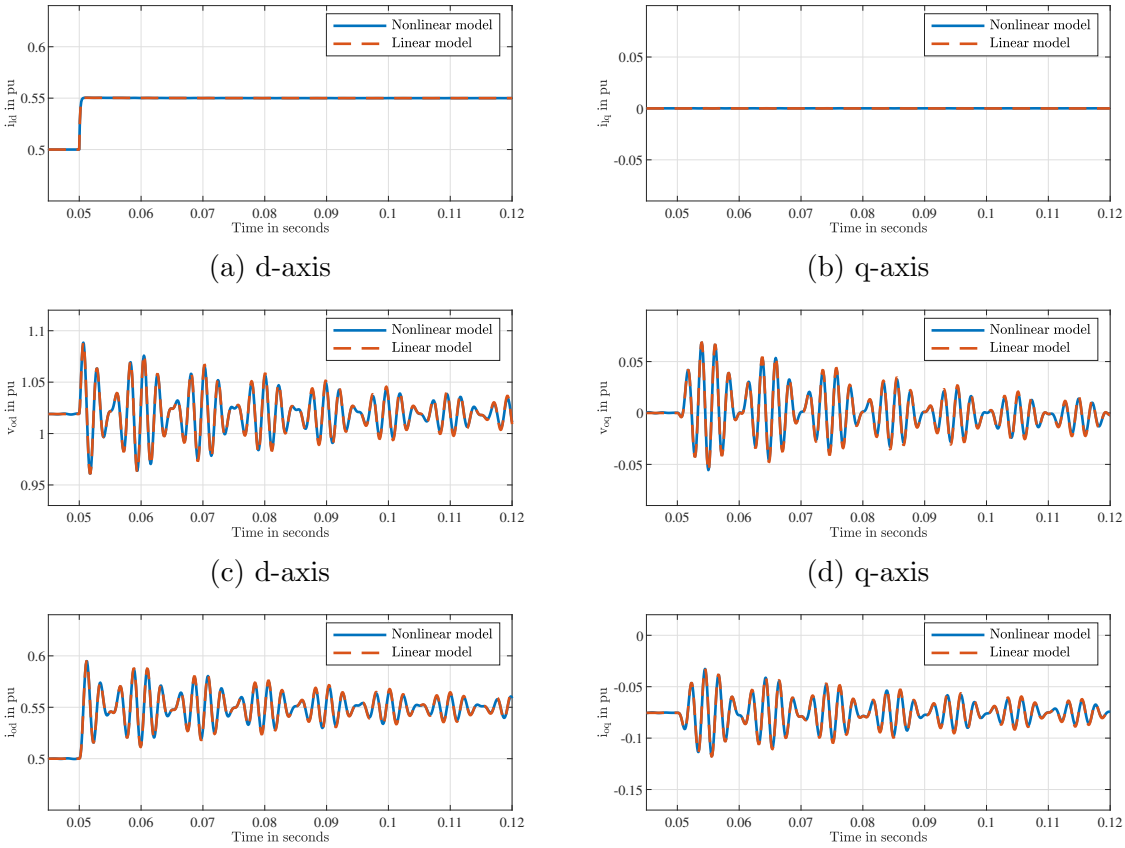

(a) d-axis (b) q-axis

(c) d-axis (d) q-axis

(e) d-axis (f) q-axis

Figure 3.8: Comparison of time domain simulations of a current controlled VSC: (a) and (b) converter current, (c) and (d) voltage at PCC, (e) and (f) grid current.

3.4.2 AC Voltage Controlled VSC

Fig 3.9 shows the responses of the AC voltage controlled VSC with a 0.05 pu change in the d-axis voltage reference input, $v_{od,ref}$, at 0.05 seconds. Fig. 3.9a and 3.9b shows the

responses of the d- and q-axis inductance current, i_{ld} and i_{lq}. As can be observed the q-axis current stays unaffected at a value close to zero, while the d-axis current experiences a small increase from its original value at 0.35 pu. The reason for this change is that when the VSC is based on an AC voltage controlled strategy, the current must be change so that it can set the voltage according to the reference value. That means that when the voltage reference is changed, the currents are also changed.

Fig. 3.9c and 3.9d shows the response of the d- and q-axis PCC voltages, v_{od} and v_{oq}. The q-axis voltage stays undisturbed at zero, while the d-axis voltage increases by 0.05 pu as expected. The step change is not as quick as the one for the current controlled VSC above, but in return it has no oscillations around the desirable value. The same goes for the d- and q-axis grid currents, i_{od} and i_{oq}.

The currents and voltages of the linearized and nonlinear model are similar to each other, which emphasizes the correctness of the derived small-signal state-space model. The analytically derived model of the AC voltage controlled VSC can therefore also be used in further stability analysis.

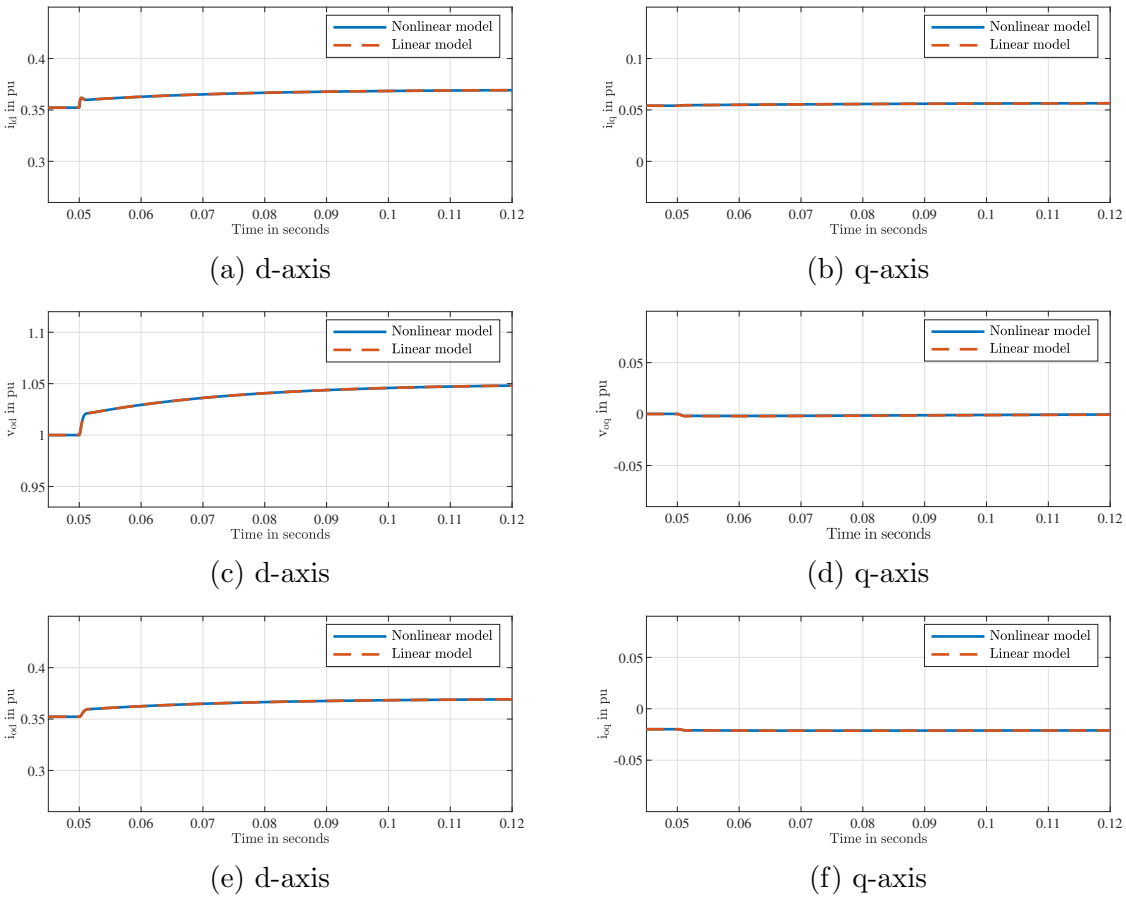

Figure 3.9: Comparison of time domain simulations of an AC voltage controlled VSC: (a) and (b) converter current, (c) and (d) voltage at PCC, (e) and (f) grid current.

3.5 Eigenvalue-Based Stability Analysis

The eigenvalue-based stability analysis was discussed in Chapter 1 as an alternative method to analyze a system's stability. This thesis mainly focuses on the impedance-based stability analysis. However, to give insight in how the state-space model can be used in stability analysis, the eigenvalue-based method is applied to the current controlled and AC voltage controlled VSC. First, it is investigated how the location of the eigenvalues change when the grid impedance is increased for the current controlled VSC. Subsequently, the impact of changing the current controller proportional gain of the AC voltage controlled VSC is observed. The findings are further verified in Chapter 5, when the impedance-based stability method is applied to investigate the same cases.

3.5.1 Current Controlled VSC

The resulting eigenvalues calculated analytically from the small-signal state-space matrix by applying the eigenvalue-based stability analysis are shown in Fig. 3.10. The model of the current controlled VSC has 10 states, and therefore also 10 eigenvalues. For the stable case in Fig. 3.10a there are 3 pairs of complex conjugated poles, 2 real poles and a pair of repeated real poles. In Fig. 3.10b, L_g is increased from 0.16 pu to 1.0 pu to investigate the impact the grid impedance has on the stability of the system. As can be observed, there are now 2 pairs of complex conjugated poles on the right-half plane (RHP), which predicts the system to be unstable under weak grid conditions.

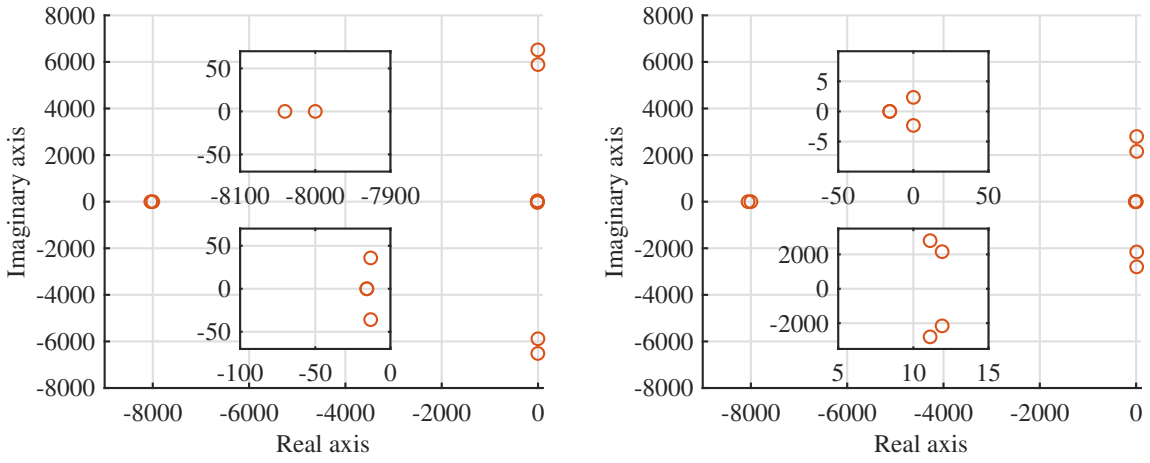

(a) (b)

Figure 3.10: Eigenvalue plot of the current controlled VSC for (a) the stable case and (b) when $L_g = 1.0$ pu.

3.5.2 AC Voltage Controlled VSC

The eigenvalues resulting from the analytical calculations of the AC voltage controlled VSC are shown in Fig. 3.11. For the stable case in Fig. 3.11a there are 4 pairs of complex conjugated poles, and 1 pair of repeated real poles. Fig. 3.11b, on the other hand, shows how the stability is affected when the proportional gain of the outer voltage control loop is decreased to 1% of its original value. It can now be observed that one pair of complex conjugated poles are located in the RHP, and the system is predicted to be unstable.

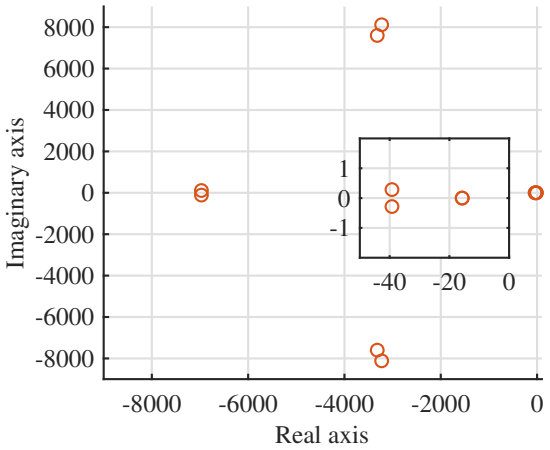

(a)

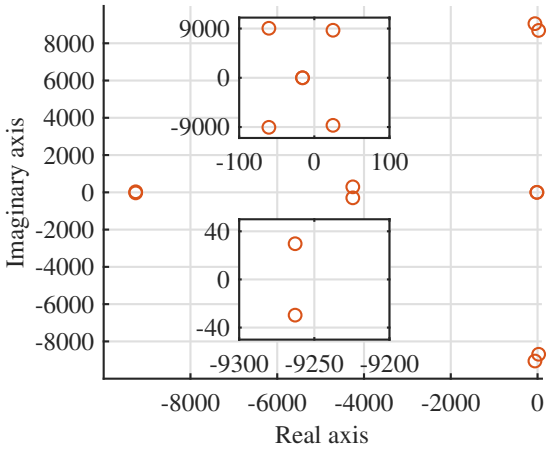

(b)

Figure 3.11: Eigenvalue plot of the AC voltage controlled VSC for (a) the stable case and (b) when k_{pvac} is decreased to 1% of original value.

Chapter 4

Impedance Modeling of the Microgrid

This chapter introduces the impedance-based stability analysis and explains how it can be applied to power electronics dominated systems. Furthermore, an analytical model of the impedance model is derived for the (I) current controlled VSC, (II) the AC voltage controlled VSC, (III) the grid-connected microgrid and (IV) the islanded microgrid. Lastly, the analytical impedance model is verified by applying the single-tone approach.

4.1 Introduction

As already mentioned in Chapter 1, the increased integration of power electronics will lead to higher reliability, efficiency and controllability. However, it will also result in power quality and stability issues which makes it crucial to to be able to perform preliminary assessment of a system's stability. The impedance-based method is, because of its advantages, commonly used to assess the stability of a power electronics dominated system. The method is regarded as an efficient and reliable tool to discover instability sources. Researchers [10] have observed that some of the instability caused by the grid impedance and control parameters is not possible to observe using the impedance-based method from the DC side. The method is therefore applied to the AC side of the systems. It determines the stability by studying the ratio between the source impedance and load impedance of a system.

To investigate the stability, it is necessary to obtain the impedance model of the analyzed system. This chapter gives an introduction to the impedance-based stability analysis. First, Section 4.2 illustrates the impedance model of (I), (II), (III) and (IV). Subsequently, Section 4.3 to 4.6 derives the AC side impedance model for the same four systems. Lastly, Section 4.7 verifies the analytically derived impedance model of the current controlled VSC by applying the single-tone approach.

4.2 Impedance-Based Stability Analysis

The main characteristics of the impedance-based stability analysis is that it divides the system into one source and one load subsystem [59]. In the following, the impedance-based stability analysis is applied to a voltage source system, a current source system and a grid-connected VSC, as done in [14], to explain how the impedance ratio can be used to assess the stability. The impedance-based model of the grid-connected and islanded microgrid is also presented as a foundation before deriving the impedance model in the following sections.

4.2.1 Subsystems of a Voltage Source System

For a voltage source system as in Fig. 4.1, the source subsystem is represented by its Thevenin equivalent with a voltage source, V_s, in series with an output impedance, Z_s, while the load subsystem is represented by its input impedance, Z_l. Considering that most of all power electronics dominated systems are nonlinear, the circuit in Fig. 4.1 is a small-signal representation and is therefore only accurate for small-signal analysis [14].

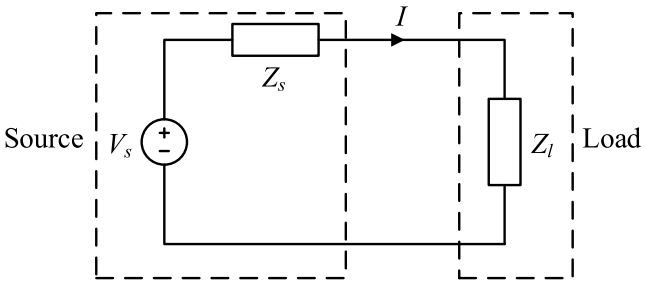

Figure 4.1: The small-signal representation of a voltage source system with load.

The load current, I, of the system can be expressed as in (4.1), which can be rearranged as in (4.2).

$$I(s) = \frac{V_s(s)}{Z_l(s) + Z_s(s)} \tag{4.1}$$

$$I(s) = \frac{V_s(s)}{Z_l(s)} \cdot \frac{1}{1 + Z_s(s)/Z_l(s)} \tag{4.2}$$

It is assumed that the voltage is stable when it is unloaded and that the load is stable when powered from an ideal voltage source. The stability of the system is therefore not affected by $V(s)$ and $1/Z_l(s)$, but is determined by $H_v(s)$ as given in (4.3).

$$H_v(s) = \frac{1}{1 + Z_s(s)/Z_l(s)} \tag{4.3}$$

$H_v(s)$ is similar to the closed-loop transfer function of a negative feedback control system, where the negative feedback equals $Z_s(s)/Z_l(s)$ and the gain is 1. From control theory, the impedance ratio, $Z_s(s)/Z_l(s)$, must satisfy the GNC for $H_v(s)$ to be stable. However, most of the grid-connected VSCs are based on a current controlled strategy and is not represented by an ideal voltage source, but by an ideal current source.

4.2.2 Subsystems of a Current Source System

To develop an impedance-based stability analysis of a current source system, Fig. 4.2 is used. It illustrates the small-signal representation of a current source system with load. The source subsystem is now represented by its Norton equivalent, where I_s is the source current which is connected in parallel to an output admittance, Y_s. The load subsystem, on the other hand, is represented by an input admittance, Y_l.

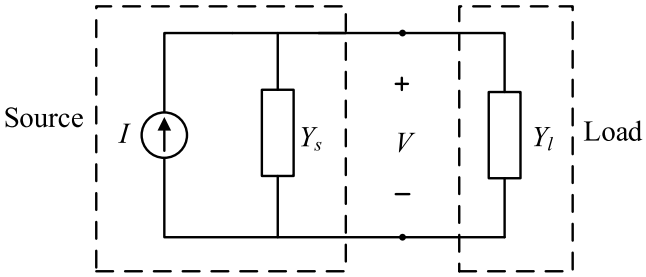

Figure 4.2: The small-signal representation of a current source system with load.

The voltage across the load is expressed as in (4.4), which is further rearranged as in (4.5).

$$V(s) = \frac{I_s(s)}{Y_l(s) + Y_s(s)} \tag{4.4}$$

$$V(s) = \frac{I_s(s)}{Y_l(s)} \cdot \frac{1}{1 + Y_s(s)/Y_l(s)} \tag{4.5}$$

As with the voltage source system, it is assumed a stable current source when its unloaded and that the load is stable when powered from an ideal current source. Both $I(s)$ and $1/Y_l(s)$ is therefore stable and the result is that the stability of the current source system is determined by $H_c(s)$ given in (4.6).

$$H_c(s) = \frac{1}{1 + Y_s(s)/Y_l(s)} \tag{4.6}$$

This also appears like the closed-loop transfer function of a negative feedback control system with unity gain, except that the negative feedback now equals the admittance ratio $Y_s(s)/Y_l(s)$, which must satisfy the GNC for $H_c(s)$ to be stable.

It can be observed that the stability of a voltage source system is decided by its impedance ratio, while the stability of a current source system is decided by its admittance ratio. To be able to easier compare the two ratios, the voltage of the current source system expressed by its impedances in (4.5) is given in (4.7).

$$V(s) = I_s(s)Z_l(s) \cdot \frac{1}{1 + Z_l(s)/Z_s(s)} \tag{4.7}$$

By comparing (4.2) and (4.7) it is observed that the requirement of stability of the voltage and current source system is the opposite of each other. For the voltage source system it is the ratio of the source impedance to the load impedance, $Z_s(s)/Z_l(s)$, while it is the ratio of the load impedance to the source impedance, $Z_l(s)/Z_s(s)$, for the current source system. This means that for the voltage source system to stay stable for a wide range of loads it should have a low Z_s and that a high Z_l secure stable operations. The current source system, on the other hand, will operate more stable for a low Z_l and require a high Z_s to operate stable for a wide range of loads.

4.2.3 Subsystems of a Grid-Connected VSC

A grid-connected VSC is represented by both a Norton equivalent and a Thevenin equivalent. The Norton equivalent represents the current controlled converter, while the grid is represented by its Thevenin equivalent. Fig. 4.3 depicts the small-signal representation of a grid-connected VSC. The converter is modeled as a current source, I_c in parallel to a converter impedance, Z_o, while the grid is modeled as a grid impedance, Z_g, in series with a voltage source, V_g.

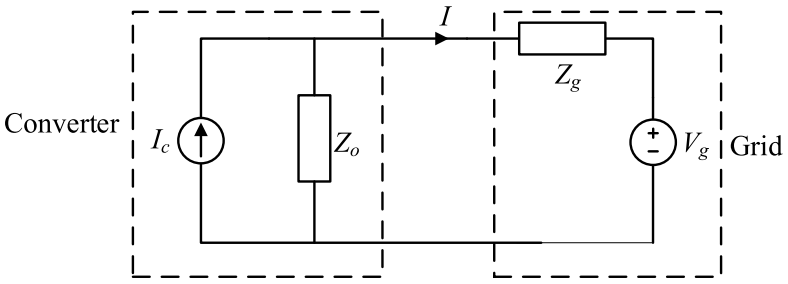

Figure 4.3: The small-signal representation of a grid-connected VSC.

According to the assumptions made for the voltage source and current source system, the grid voltage is stable when unloaded and the converter is stable if it is powered from an ideal voltage source which implicates that Z_g is zero. From Fig. 4.3, the converter output current, I, is given by (4.8), which is rearranged to (4.9).

$$I(s) = \frac{I_c(s)Z_o(s)}{Z_o} - \frac{V_g(s)}{Z_o(s) + Z_g(s)} \tag{4.8}$$

$$I(s) = \left(I_c(s) - \frac{V_g(s)}{Z_o(s)} \right) \cdot \frac{1}{1 + Z_g(s)/Z_o(s)} \tag{4.9}$$

From the equations it can be observed that the ratio of the grid impedance to the converter output impedance, $Z_g(s)/Z_o(s)$, must satisfy the GNC for the grid-connected VSC to be stable. In addition, the converter impedance, Z_o, should be high to provide stable operations under a wide range of grid conditions. The grid impedance, Z_g, on the other hand, should be low to ensure more stable operations.

Small-signal representation of a system requires a steady-state operating point. As explained in Chapter 3, since an AC system do not have an equilibrium, it is necessary to convert the signals from abc-frame to dq-frame. A result from this transformation is that the grid impedance, $\mathbf{Z_g^{dq}}$, and converter impedance, $\mathbf{Z_o^{dq}}$, is given as a 2×2-matrix as in (4.10), where the off-diagonal elements, $Z_{dq}(s)$ and $Z_{qd}(s)$, occur as a result of the cross-coupling effect between the d- and q-axis. Throughout this thesis, bold font represents a matrix.

$$\begin{aligned} \mathbf{Z_g^{dq}}(s) &= \begin{bmatrix} Z_{g,dd}(s) & Z_{g,dq}(s) \\ Z_{g,qq}(s) & Z_{g,qd}(s) \end{bmatrix} \\ \mathbf{Z_o^{dq}}(s) &= \begin{bmatrix} Z_{o,dd}(s) & Z_{o,dq}(s) \\ Z_{o,qq}(s) & Z_{o,qd}(s) \end{bmatrix} \end{aligned} \tag{4.10}$$

4.2.4 Subsystems of the Grid-Connected Microgrid

The VSCs that are represented by a Norton equivalent are based on a current controlled strategy, while the VSCs that are represented by a Thevenin equivalent are based on an AC voltage controlled strategy [27]. When the microgrid is in grid-connected mode the converters can therefore be represented by their Norton equivalent circuit with an ideal current source connected in parallel with an admittance [60]. Fig. 4.4 depicts the impedance-based model of the microgrid and as can be seen, the different microsources and loads are connected to the main grid through the PCC. The switch is closed to emphasize the operation in grid-connected mode. For every VSC n, the admittance is represented by $Y_{o,n}$ while the ideal current source is represented by $i_{o,n}$. The subscript $n \in 1, 2, 3, 4$ is introduced to easier keep track of the different converters. "1" represents the PV, "2" represents the wind power, "3" represents the IG and "4" represents the BESS. The regular RL-load is represented by Z_{load}. The grid, on the other hand, is represented by its Thevenin equivalent circuit which consists of an ideal voltage source, v_g, in series with an output impedance Z_g.

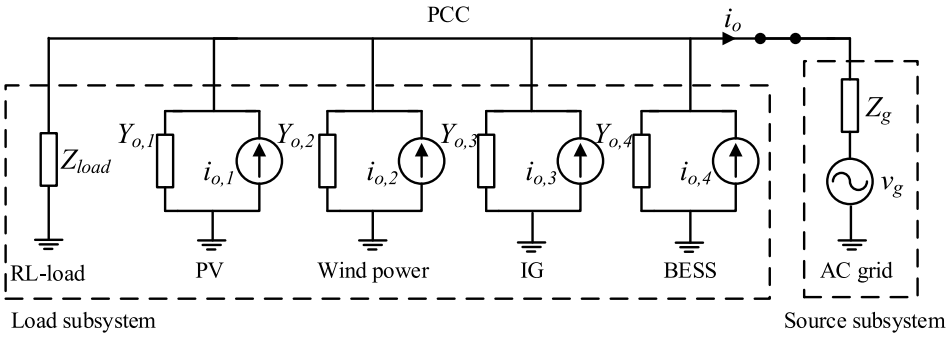

Figure 4.4: Impedance-based model of the microgrid in grid-connected mode.

4.2.5 Subsystems of the Islanded Microgrid

Since the grid is disconnected when the microgrid is operating in islanded mode, it is necessary that one of the converters has an AC voltage controlled strategy and is represented by its Thevenin equivalent. Fig. 4.5 illustrates the impedance-based model of the microgrid in islanded mode where the converter of the BESS is represented by its Thevenin equivalent circuit while the IG, PV and wind power stay represented by their Norton equivalent. The Thevenin equivalent consists of an ideal voltage source, $v_{o,4}$, in series with an output impedance, $Z_{o,4}$.

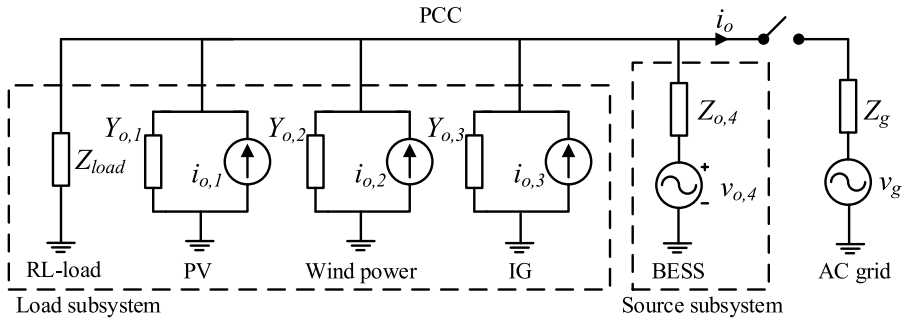

Figure 4.5: Impedance-based model of the microgrid in islanded mode.

4.3 DQ-Domain Impedance Modeling of the Current Controlled VSC

The dq-domain impedance model of the current controlled VSC is now derived. As can be observed in Fig. 4.6 the system is divided into two subsystems at PCC, where the grid equivalent system consists of the grid impedance and filter capacitor, while the converter subsystem consists of the converter impedance and the converter characteristics. The minor loop gain, $\mathbf{L}(s)$, is given by the impedance matrix of the grid equivalent, $\mathbf{Z_{geq}}(s)$, multiplied by the admittance matrix of the current controlled VSC, $\mathbf{Z_{cc}}^{-1}(s)$ as in (4.11).

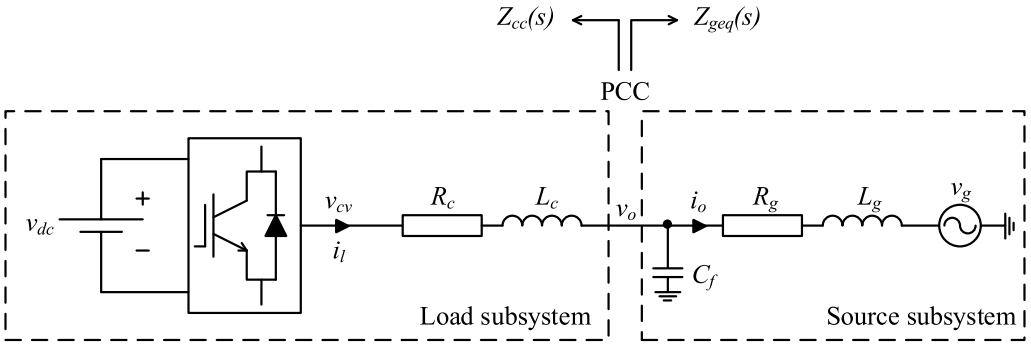

Figure 4.6: Subsystems of a current-controlled VSC.

$$\mathbf{L}(s) = \mathbf{Z_{geq}}(s)\mathbf{Z_{cc}}^{-1}(s) \tag{4.11}$$

4.3.1 Dynamic Equations

The converter impedance is the impedance seen from the PCC towards the converter. The voltage at this point is v_o and the current is i_l. The converter impedance is therefore given by the voltage divided by the current at this point. Using Fig. 4.6, equation (4.12) can be derived to describe the interface voltage, where $\mathbf{Z_o}$ consist of the series impedance, L_c and R_c, between the converter and the PCC and the converter output voltage is expressed by the modulation index, m, multiplied with v_{dc}.

$$\begin{bmatrix} v_{od}^s \\ v_{oq}^s \end{bmatrix} = \begin{bmatrix} m_d^s \\ m_q^s \end{bmatrix} v_{dc} - \underbrace{\begin{bmatrix} R_c + sL_c & -\omega_g L_c \\ \omega_g L_c & R_c + sL_c \end{bmatrix}}_{\mathbf{Z_o}(\mathrm{s})} \cdot \begin{bmatrix} i_{ld}^s \\ i_{lq}^s \end{bmatrix} \tag{4.12}$$

4.3.2 Current Controller

To find the converter impedance it is necessary to express the the modulation index in terms of the interface voltage v_o and the current i_l. Using the block diagram of the control system of the current controlled VSC in Fig. 2.19, the d- and q-axis modulation index can be stated as in (4.13).

$$\begin{aligned} m_d^c &= \underbrace{e^{-sT_s}\frac{1-e^{-sT_s}}{sT_s}}_{\mathrm{PWM}} \cdot \left((k_{pc} + \frac{k_{ic}}{s})(i_{ld,ref}^c - i_{ld}^c) + v_{od}^c - \omega_g L_c i_{lq}^c \right) \\ m_q^c &= \underbrace{e^{-sT_s}\frac{1-e^{-sT_s}}{sT_s}}_{\mathrm{PWM}} \cdot \left((k_{pc} + \frac{k_{ic}}{s})(i_{lq,ref}^c - i_{ld}^c) + v_{oq}^c + \omega_g L_c i_{ld}^c \right) \end{aligned} \tag{4.13}$$

These two equations can be collected into matrix form as in (4.14).

$$\begin{bmatrix} m_d^c \\ m_q^c \end{bmatrix} = \underbrace{\begin{bmatrix} H_{pwm} & 0 \\ 0 & H_{pwm} \end{bmatrix}}_{\mathbf{G_{pwm}(s)}} \cdot \left(\underbrace{\begin{bmatrix} H_{cc} & 0 \\ 0 & H_{cc} \end{bmatrix}}_{\mathbf{G_{cc}(s)}} \cdot \begin{bmatrix} i_{ld,ref}^c - i_{ld}^c \\ i_{lq,ref}^c - i_{lq}^c \end{bmatrix} - \underbrace{\begin{bmatrix} 0 & \omega_{pll} L_c \\ -\omega_{pll} L_c & 0 \end{bmatrix}}_{\mathbf{Z_{del}}} \cdot \begin{bmatrix} i_{ld}^c \\ i_{lq}^c \end{bmatrix} + \begin{bmatrix} v_{od}^c \\ v_{oq}^c \end{bmatrix} \right) \quad (4.14)$$

$\mathbf{G_{pwm}}(s)$ represents the PWM delay, where $H_{pwm}(s) = e^{-sT_s} \cdot \frac{1-e^{-sT_s}}{sT_s}$ and T_s is the sampling delay. $\mathbf{G_{cc}}(s)$ is the current compensator transfer function where $H_{cc}(s) = k_{pc} + \frac{k_{ic}}{s}$. Equation (4.14) can now be expressed simpler as in (4.15).

$$\begin{bmatrix} m_d^c \\ m_q^c \end{bmatrix} = \mathbf{G_{pwm}}(s)\mathbf{G_{cc}}(s) \cdot \begin{bmatrix} i_{ld,ref}^c \\ i_{lq,ref}^c \end{bmatrix} - \mathbf{G_{pwm}}(s)(\mathbf{G_{cc}}(s) + \mathbf{Z_{del}}) \cdot \begin{bmatrix} i_{ld}^c \\ i_{lq}^c \end{bmatrix} + \mathbf{G_{pwm}}(s) \cdot \begin{bmatrix} v_{od}^c \\ v_{oq}^c \end{bmatrix} \quad (4.15)$$

4.3.3 Transformation from Controller to System Referance Frame

To explain the superscript "s" and "c" in (4.12) to (4.13) the PLL must be closer looked at. There are papers, such as [61], that explain this thoroughly. The PLL introduces two dq-frames, where the superscript "s" represents the system dq-frame at system frequency, while superscript "c" represents the controller dq-frame at PLL frequency. Fig. 4.7 illustrates the difference between the two dq-frames.

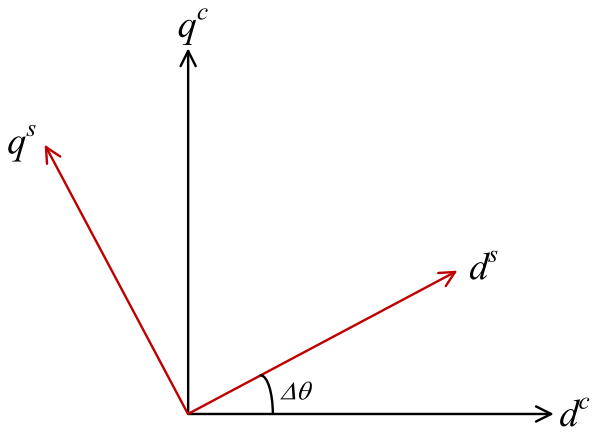

Figure 4.7: Controller and system dq-frame.

If the converter system is in steady-state the two dq-frames in Fig. 4.7 would be aligned with each other. The position of the dq-frame of the system is first changed when small-signal perturbations are added to the grid voltage. This change happens because of the PI-regulator of the PLL. The angle between the system- and controller dq-frame is represented as $\Delta\theta$.

The modulation indexes, currents and voltages in (4.13) are all given in the controller reference frame. To find the converter impedance, it is necessary to convert them to the

system reference frame. This is served by the matrix $\mathbf{T}_{\mathbf{\Delta}\theta}$ in (4.16), which is used to transform between system and controller frame for the duty cycle, voltage and current as in (4.17). The voltage and current vectors in the system dq-frame must be transformed by $\mathbf{T}_{\mathbf{\Delta}\theta}$ to the controller dq-frame to use as inputs in the current controller. While the duty cycle in the controller dq-frame is transformed by the inverse of matrix $\mathbf{T}_{\mathbf{\Delta}\theta}$ to control the IGBTs in the converter bridge in the system dq-frame.

$$\mathbf{T}_{\mathbf{\Delta}\theta} = \begin{bmatrix} \cos(\Delta\theta) & \sin(\Delta\theta) \\ -\sin(\Delta\theta) & \cos(\Delta\theta) \end{bmatrix} \tag{4.16}$$

$$\vec{v}_o^{\,c} = \mathbf{T}_{\mathbf{\Delta}\theta}\vec{v}_o^{\,s}, \qquad \vec{i}_l^{\,c} = \mathbf{T}_{\mathbf{\Delta}\theta}\vec{i}_l^{\,s}, \qquad \vec{d}^{\,s} = \mathbf{T}_{\mathbf{\Delta}\theta}{}^{-1}\vec{d}^{\,c} \tag{4.17}$$

The small-signal perturbations added to the PCC voltage, v_o, will influence the output angle of the PLL, θ, which will further affect the current and duty cycle of the controller. The result of this is that also the converter output voltage, v_{cv}, and the inductance current, i_l, are influenced by the perturbations, which lastly causes the impedance of the converter to be affected by the perturbations. This emphasize the importance of taking the propagation of the small-signal perturbation through the PLL into account. This is done by finding the transfer functions $\mathbf{G}^{\mathbf{v}}_{\mathbf{pll}}(s)$, $\mathbf{G}^{\mathbf{i}}_{\mathbf{pll}}(s)$ and $\mathbf{G}^{\mathbf{d}}_{\mathbf{pll}}(s)$, which models the small-signal perturbation path from the system to controller dq-frame for respectively the voltage, current and duty cycle. To find these three transfer functions, an average model of the PLL is given in Fig. 4.8.

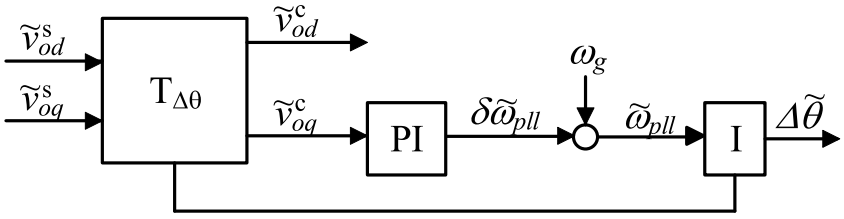

Figure 4.8: Average model of PLL in dq-frame.

As already discussed the two dq-frames would be aligned in steady-state, which gives (4.18). V_o, I_l and D is the steady-state values of the PCC voltage, inductance current and duty cycle, respectively.

$$\vec{V}_o^{\,c} = \vec{V}_o^{\,s}, \qquad \vec{I}_l^{\,c} = \vec{I}_l^{\,s}, \qquad \vec{D}^s = \vec{D}^c \tag{4.18}$$

Following, only the calculations of $\mathbf{G}^{\mathbf{v}}_{\mathbf{pll}}(s)$ is demonstrated, but the same follows for the current and the duty cycle. When assuming that $\Delta\theta$ is equal to zero, (4.16) can be rewritten as in (4.19).

$$\vec{V}_o^{\,c} = \begin{bmatrix} \cos(0) & \sin(0) \\ -\sin(0) & \cos(0) \end{bmatrix} \vec{V}_o^{\,s} \tag{4.19}$$

Adding small-signal perturbations to (4.19) gives (4.20).

$$\begin{bmatrix} V_{od}^c + \tilde{v}_{od}^c \\ V_{oq}^c + \tilde{v}_{oq}^c \end{bmatrix} = \begin{bmatrix} \cos(0 + \Delta\tilde{\theta}) & \sin(0 + \Delta\tilde{\theta}) \\ -\sin(0 + \Delta\tilde{\theta}) & \cos(0 + \Delta\tilde{\theta}) \end{bmatrix} \cdot \begin{bmatrix} V_{od}^s + \tilde{v}_{od}^s \\ V_{oq}^s + \tilde{v}_{oq}^s \end{bmatrix} \tag{4.20}$$

In equation (4.21), small-angle approximation has been applied.

$$\begin{bmatrix} V_{od}^c + \tilde{v}_{od}^c \\ V_{oq}^c + \tilde{v}_{oq}^c \end{bmatrix} \approx \begin{bmatrix} 1 & \Delta\tilde{\theta} \\ -\Delta\tilde{\theta} & 1 \end{bmatrix} \cdot \begin{bmatrix} V_{od}^s + \tilde{v}_{od}^s \\ V_{oq}^s + \tilde{v}_{oq}^s \end{bmatrix} \tag{4.21}$$

Lastly, equation (4.22) is derived by linearization and canceling steady-state terms in accordance to (4.18).

$$\begin{bmatrix} \tilde{v}_{od}^c \\ \tilde{v}_{oq}^c \end{bmatrix} \approx \begin{bmatrix} \tilde{v}_{od}^s + V_{oq}^s \Delta\tilde{\theta} \\ \tilde{v}_{oq}^s - V_{od}^s \Delta\tilde{\theta} \end{bmatrix} \tag{4.22}$$

To express the voltage of the controller dq-frame with terms only from the system dq-frame, an expression of $\Delta\tilde{\theta}$ must be found. From the average model of the PLL in Fig. 4.8, $\Delta\tilde{\theta}$ can be given as in (4.23), where $tf_{pll} = k_{ppll} + \frac{1}{s}k_{ipll}$.

$$\Delta\tilde{\theta} = \tilde{v}_{oq}^c \cdot tf_{pll} \cdot \frac{1}{s} \tag{4.23}$$

By substituting the expression of $\tilde{v}_{oq}^c$ of (4.23) into the second equation of (4.22), $\Delta\tilde{\theta}$ is further derived with only terms from the system dq-frame, as in (4.24).

$$\Delta\tilde{\theta} = \frac{tf_{pll}}{s + V_{od}^s \cdot tf_{pll}} \tilde{v}_{oq}^s \tag{4.24}$$

By defining $\mathbf{G_{pll}}(s)$ as in (4.25), the expression of $\Delta\tilde{\theta}$ is simplified further as shown in (4.26).

$$\mathbf{G_{pll}}(s) = \frac{tf_{pll}}{s + V_{od}^s \cdot tf_{pll}} \tag{4.25}$$

$$\Delta\tilde{\theta} = \mathbf{G_{pll}}(s)\tilde{v}_{oq}^s \tag{4.26}$$

Equation (4.22) can now be rewritten as in (4.27). The result is an approach to go from the small-signal perturbation voltage of the controller dq-frame to the small-signal perturbation voltage of the system dq-frame. The transfer function matrix, $\mathbf{G_{pll}^v}(s)$,

that models this small-signal perturbation path from system to controller dq-frame is also shown in (4.27).

$$\begin{bmatrix} \tilde{v}^c_{od} \\ \tilde{v}^c_{oq} \end{bmatrix} \approx \begin{bmatrix} \tilde{v}^s_{od} + V^s_{oq} G_{pll}(s) \tilde{v}^s_{oq} \\ \tilde{v}^s_{oq} - V^s_{od} G_{pll}(s) \tilde{v}^s_{oq} \end{bmatrix} = \underbrace{\begin{bmatrix} 1 & V^s_{oq} G_{pll}(s) \\ 0 & 1 - V^s_{od} G_{pll}(s) \end{bmatrix}}_{\mathbf{G^v_{pll}(s)}} \begin{bmatrix} \tilde{v}^s_{od} \\ \tilde{v}^s_{oq} \end{bmatrix} \tag{4.27}$$

The same procedure can be used to find $\mathbf{G^i_{pll}}(s)$ and $\mathbf{G^d_{pll}}(s)$, and the resulting matrices are shown in (4.28) and (4.29), respectively.

$$\begin{bmatrix} \tilde{i}^c_{ld} \\ \tilde{i}^c_{lq} \end{bmatrix} = \begin{bmatrix} \tilde{i}^s_{ld} \\ \tilde{i}^s_{lq} \end{bmatrix} + \underbrace{\begin{bmatrix} 0 & I^s_{lq} G_{pll}(s) \\ 0 & -I^s_{ld} G_{pll}(s) \end{bmatrix}}_{\mathbf{G^i_{pll}(s)}} \cdot \begin{bmatrix} \tilde{v}^s_{od} \\ \tilde{v}^s_{oq} \end{bmatrix} \tag{4.28}$$

$$\begin{bmatrix} \tilde{m}^c_{d} \\ \tilde{m}^c_{q} \end{bmatrix} = \begin{bmatrix} \tilde{m}^s_{d} \\ \tilde{m}^s_{q} \end{bmatrix} - \underbrace{\begin{bmatrix} 0 & -D^s_{q} G_{pll}(s) \\ 0 & D^s_{d} G_{pll}(s) \end{bmatrix}}_{\mathbf{G^d_{pll}(s)}} \begin{bmatrix} \tilde{v}^s_{od} \\ \tilde{v}^s_{oq} \end{bmatrix} \tag{4.29}$$

4.3.4 The Converter Impedance

Equation (4.30) can now be linearized and expressed with terms only from the system dq-frame by writing it in small-signal form and inserting (4.27) to (4.29). Because the VSC is controlled by a current controller, the reference currents, $i_{ld,ref}$ and $i_{lq,ref}$, are constants and are cancelled when linearizing. The result is given in (4.30), and for simplicity $\mathbf{G^P_C}$ is short for the expression given in (4.31).

$$\begin{bmatrix} \tilde{m}^s_d \\ \tilde{m}^s_q \end{bmatrix} = \mathbf{G^P_C}(s) \cdot \begin{bmatrix} \tilde{v}^s_{od} \\ \tilde{v}^s_{oq} \end{bmatrix} - \mathbf{G_{pwm}}(s) \cdot (\mathbf{G_{cc}}(s) + \mathbf{Z_{del}}) \begin{bmatrix} \tilde{i}^s_{ld} \\ \tilde{i}^s_{lq} \end{bmatrix} \tag{4.30}$$

$$\mathbf{G^P_C}(s) = \mathbf{G^d_{pll}}(s) + \mathbf{G_{pmw}}(s)\mathbf{G^v_{pll}}(s) - \mathbf{G_{pwm}}(s) \cdot (\mathbf{G_{cc}}(s) + \mathbf{Z_{del}}\mathbf{G^i_{pll}}(s)) \tag{4.31}$$

The last step is to insert (4.30) into (4.12). With the converter output voltage expressed by voltage vector $\vec{v}^s_o$ and current vector $\vec{i}^s_l$ the converter impedance is found in (4.32). Where V_{dc} is the steady-state value of the DC-voltage and $\mathbf{I}(s)$.

$$\mathbf{Z_{cc}}(s) = \frac{\vec{v}^s_o}{\vec{i}^s} = \frac{-\mathbf{G_{pwm}}(s)(\mathbf{G_{cc}}(s) + \mathbf{Z_{del}})V_{dc} - \mathbf{Z_o}(s)}{\mathbf{I}(s) - V_{dc}\mathbf{G^P_C}(s)} \tag{4.32}$$

4.3.5 The Grid Equivalent Impedance

The grid equivalent impedance contains the grid resistance and inductance, R_g and L_g, and the filter capacitance, C_f. By using the dq-transformation the series grid impedance, $\mathbf{Z_g}(s)$, is given in (4.33) and the filter admittance, $\mathbf{Y_{C_f}}(s)$, is given in (4.34).

$$\mathbf{Z_g}(s) = \begin{bmatrix} R_g + sL_g & -\omega_g L_g \\ \omega_g L_g & R_g + sL_g \end{bmatrix} \tag{4.33}$$

$$\mathbf{Y_{C_f}}(s) = \begin{bmatrix} sC_f & -\omega_g C_f \\ \omega_g C_f & sC_f \end{bmatrix}^{-1} \tag{4.34}$$

The total grid equivalent impedance can now be found by (4.35).

$$\mathbf{Z_{geq}}(s) = \left(\mathbf{Z_g}(s)^{-1} + \mathbf{Y_{C_f}}(s)\right)^{-1} \tag{4.35}$$

4.4 DQ-Domain Impedance Modeling of the Grid-Connected Microgrid

As discussed in Subsection 4.2.4, all of the VSCs constituting the microgrid in grid-connected mode will have a current controlled strategy and can be represented by their Norton equivalent. From Fig. 4.9, it can be observed that the PCC now is located before the grid impedance to ensure that the two converters have the same information about the voltage, to ensure synchronization with the grid. To constitute the LCL-filter, an additional filter inductance, $L_f = 0.1$ pu, is connected in parallel with C_f.

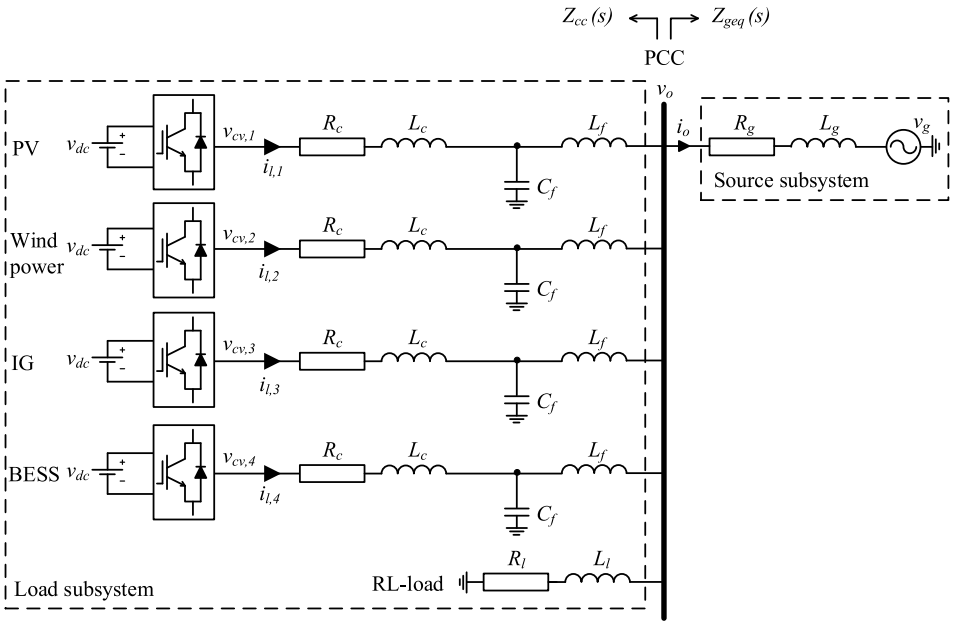

Figure 4.9: Subsystems of a grid-connected microgrid

The system is now divided into new subsystems and it is necessary to derive a new grid equivalent impedance, $\mathbf{Z_{geq}}(s)$, and a new current controlled converter impedance, $\mathbf{Z_{cc}}(s)$. The new grid equivalent impedance consist of the grid impedance, R_g and L_g, while the new converter impedance equals the parallel connection of the four current controlled VSCs and the load. The resulting minor loop gain, $\mathbf{L}(s)$, for the grid-connected microgrid is given in (4.36).

$$\mathbf{L}(s) = \mathbf{Z_{geq}}(s){\mathbf{Z_{cc}}}^{-1}(s) \tag{4.36}$$

4.4.1 The Converter Impedance

The new converter impedance will be similar to the one found in Subsection 4.3.4, except that the matrix $\mathbf{Z_o}(s)$ will change. In addition to consist of the converter impedance, R_c and L_c, the new $\mathbf{Z_o}(s)$ will consist of the new filter inductance, L_f, and the filter capacitance, C_f, as given in (4.37).

$$\mathbf{Z_o}(s) = \underbrace{\begin{bmatrix} sL_f & -\omega_g L_f \\ \omega_g L_f & sL_f \end{bmatrix}}_{\mathbf{Z_{Lf}(s)}} + \left(\underbrace{\begin{bmatrix} sC_f & -\omega_g C_f \\ \omega_g C_f & sC_f \end{bmatrix}}_{\mathbf{Y_{Cf}(s)}} + \underbrace{\begin{bmatrix} R_c + sL_c & -\omega_g L_c \\ \omega_g L_c & R_c + sL_c \end{bmatrix}^{-1}}_{\mathbf{Z_o(s)}} \right)^{-1} \tag{4.37}$$

The RL-load, $\mathbf{Z_{load}}(s)$, that is a part of the microgrid is given in (4.38) and must also be taken into account when calculating the new impedance model of the converter.

$$\mathbf{Z_{load}}(s) = \begin{bmatrix} R_l + sL_l & -\omega_g L_l \\ \omega_g L_l & R_l + sL_l \end{bmatrix} \tag{4.38}$$

The new load impedance, $\mathbf{Z_{cc}}(s)$, for the grid-connected microgrid is given by each individual current controlled VSC and the load impedance, connected in parallel as in (4.39)

$$\mathbf{Z_{cc}}(s) = \mathbf{Z_{cc,1}}(s) \parallel \mathbf{Z_{cc,2}}(s) \parallel \mathbf{Z_{cc,3}}(s) \parallel \mathbf{Z_{cc,4}}(s) \parallel \mathbf{Z_{load}}(s) \tag{4.39}$$

4.4.2 The Grid Equivalent Impedance

The new grid impedance consists only of the series grid inductance, L_g, and grid resistance, R_g as given in (4.40).

$$\mathbf{Z_{geq}}(s) = \begin{bmatrix} R_g + sL_g & -\omega_g L_g \\ \omega_g L_g & R_g + sL_g \end{bmatrix} \tag{4.40}$$

4.5 DQ-Domain Impedance Modeling of the AC Voltage Controlled VSC

The dq-domain impedance model of an AC voltage controlled VSC is now derived. Since the VSC is disconnected from the grid it can be represented as the voltage source system in Subsection 4.2.1. The division between subsystems is therefore given as in Fig. 4.10.

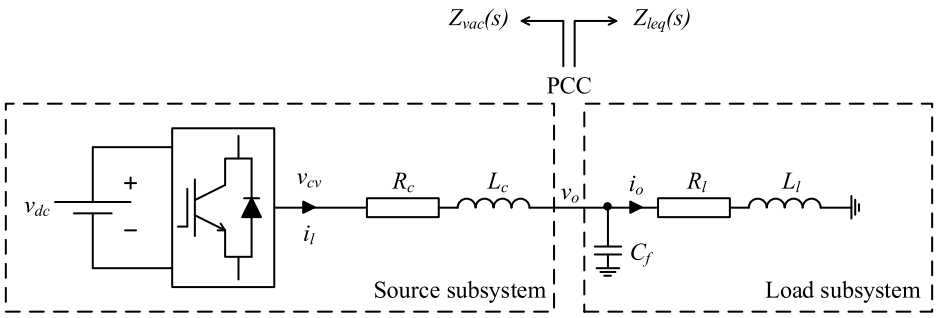

Figure 4.10: Subsystems of an AC voltage controlled VSC.

The VSC is represented by its Thevenin equivalent and the source subsystem is now the AC voltage controlled converter impedance, $\mathbf{Z_{vac}}(s)$. The load subsystem is now the load equivalent impedance, $\mathbf{Z_{leq}}(s)$, that consists of the filter capacitance, C_f, the load resistor, R_l, and the load inductance, L_l. The minor loop gain of the AC voltage controlled VSC, $\mathbf{L}(s)$ is given as in (4.41).

$$\mathbf{L}(s) = Z_{vac}(s)Z_{leq}^{-1}(s) \tag{4.41}$$

4.5.1 Dynamic Equations

The dynamic equations of the AC voltage controlled VSC, is similar to the one found for the current controlled VSC in Subsection 4.3.1. However, since the AC voltage controlled VSC does not need a PLL it is not necessary to separate between system frequency and control frequency. Using Fig. 4.10, the PCC voltage, v_o, can be described as in (4.42).

$$\begin{bmatrix} v_{od} \\ v_{oq} \end{bmatrix} = \begin{bmatrix} m_d \\ m_q \end{bmatrix} v_{dc} - \underbrace{\begin{bmatrix} R_c + sL_c & -\omega_g L_c \\ \omega_g L_c & R_c + sL_c \end{bmatrix}}_{\mathbf{Z_o}} \cdot \begin{bmatrix} i_{ld} \\ i_{lq} \end{bmatrix} \tag{4.42}$$

4.5.2 Outer Voltage Controller

From the control structure of the outer voltage loop given in Fig. 2.21 the d- and q-axis reference current input of the current controller can be obtained as in (4.43), where $H_{vac}(s) = k_{pvac} + k_{ivac}/s$.

$$\begin{bmatrix} i_{ld,ref} \\ i_{lq,ref} \end{bmatrix} = \underbrace{\begin{bmatrix} H_{vac}(s) & 0 \\ 0 & H_{vac}(s) \end{bmatrix}}_{\mathbf{G_{vac}(s)}} \cdot \left(\begin{bmatrix} v_{od,ref} \\ v_{oq,ref} \end{bmatrix} - \begin{bmatrix} v_{od} \\ v_{oq} \end{bmatrix} \right) \tag{4.43}$$

4.5.3 Current Controller

The modulation indexes obtained from the inner current control loop is the same as the equations found for the current controlled VSC in Subsection 4.3.2. However, as with the dynamic equations, it is longer necessary to divide between system and control frequency, and m_d and m_q can be given as in (4.44). $\mathbf{G_{pwm}}(s)$, $\mathbf{G_{cc}}(s)$ and $\mathbf{Z_{del}}$ is the same as for the current controlled VSC.

$$\begin{bmatrix} m_d \\ m_q \end{bmatrix} = \underbrace{\begin{bmatrix} H_{pwm} & 0 \\ 0 & H_{pwm} \end{bmatrix}}_{\mathbf{G_{pwm}(s)}} \cdot \left(\underbrace{\begin{bmatrix} H_{cc} & 0 \\ 0 & H_{cc} \end{bmatrix}}_{\mathbf{G_{cc}(s)}} \cdot \begin{bmatrix} i_{ld,ref} - i_{ld} \\ i_{lq,ref} - i_{lq} \end{bmatrix} - \underbrace{\begin{bmatrix} 0 & \omega_{pll} L_c \\ -\omega_{pll} L_c & 0 \end{bmatrix}}_{\mathbf{Z_{del}}} \cdot \begin{bmatrix} i_{ld} \\ i_{lq} \end{bmatrix} + \begin{bmatrix} v_{od} \\ v_{oq} \end{bmatrix} \right) \tag{4.44}$$

4.5.4 The Converter Impedance

To obtain the impedance model of the AC voltage controlled VSC from (4.42), it is necessary to find the modulation index, m, as a function of i_l and v_o in the frequency domain. Linearizing and combining (4.43) and (4.44), the modulation index can be expressed as in (4.45).

$$\begin{bmatrix} \tilde{m}_d \\ \tilde{m}_q \end{bmatrix} = \mathbf{G_{pwm}}(s) \cdot (\mathbf{I}(s) - \mathbf{G_{cc}}(s)\mathbf{G_{vac}}(s)) \begin{bmatrix} \tilde{v}_{od} \\ \tilde{v}_{oq} \end{bmatrix} - \mathbf{G_{pwm}}(s) \cdot (\mathbf{G_{cc}}(s) + \mathbf{Z_{del}}) \cdot \begin{bmatrix} \tilde{i}_{ld} \\ \tilde{i}_{lq} \end{bmatrix} \tag{4.45}$$

By linearizing (4.45) and inserting it into (4.42), the impedance model of the AC voltage controlled VSC can now be found as in (4.46).

$$\mathbf{Z_{cc}}(s) = \frac{\vec{v}_o}{\vec{i}_l} = \frac{\mathbf{Z_o}(s) + V_{dc}\mathbf{G_{pwm}}(s) \cdot (\mathbf{G_{cc}}(s) + \mathbf{G_{del}})}{\mathbf{I}(s) - V_{dc}\mathbf{G_{pwm}}(s) \cdot (\mathbf{I}(s) - \mathbf{G_{cc}}(s)\mathbf{G_{vac}}(s))} \tag{4.46}$$

4.5.5 The Load Equivalent Impedance

The load equivalent impedance contains the load resistance and inductance, R_l and L_l, and the filter capacitance, C_f. By using the dq-transformation the series load impedance, $\mathbf{Z_l}(s)$, is given in (4.47) and the filter admittance, $\mathbf{Y_{C_f}}(s)$, is given in (4.48).

$$\mathbf{Z_l}(s) = \begin{bmatrix} R_l + sL_l & -\omega_q L_l \\ \omega_g L_l & R_l + sL_l \end{bmatrix} \tag{4.47}$$

$$\mathbf{Y_{C_f}}(s) = \begin{bmatrix} sC_f & -\omega_g C_f \\ \omega_g C_f & sC_f \end{bmatrix}^{-1} \tag{4.48}$$

The total load equivalent impedance can now be found by (4.49).

$$\mathbf{Z_{leq}}(s) = \left[Z_l(s)^{-1} + Y_{C_f}(s)\right]^{-1} \tag{4.49}$$

4.6 DQ-Domain Impedance Modeling of the Islanded Microgrid

As discussed in Subsection 4.2.5, the BESS will change to an AC voltage controlled strategy when the microgrid operates in islanded mode. The other three VSCs will keep their current controlled strategy. The converter impedance of the AC voltage controlled VSC, $\mathbf{Z_{vac}}(s)$, will be the source impedance since it is represented by its Thevenin equivalent. The parallel connection of the load and the three current controlled VSCs, $\mathbf{Z_{cc}}(s)$, will be the load impedance. The division of the subsystems is illustrated in Fig. 4.11. The new minor loop gain, $\mathbf{L}(s)$, is given in (4.50).

$$\mathbf{L}(s) = \mathbf{Z_{vac}}(s)\mathbf{Z_{cc}}^{-1}(s) \tag{4.50}$$

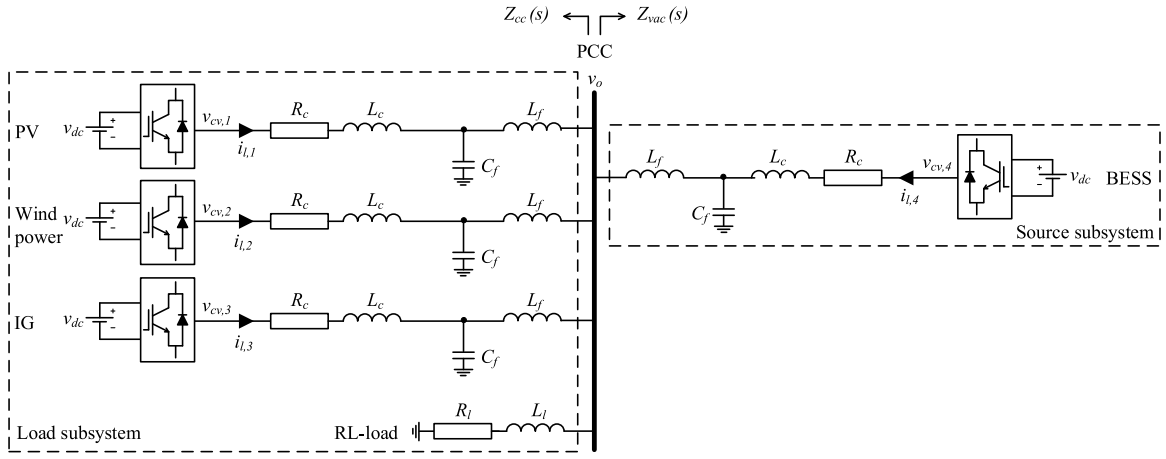

Figure 4.11: Subsystems of the islanded microgrid.

4.6.1 The Source Impedance

The source impedance will be similar to the one found for the single AC voltage controlled converter found in Subsection 4.5.4, except that $\mathbf{Z_o}(s)$ now will consist of the filter inductance, L_c, and the filter capacitance, C_f, as given in Subsection 4.4.1 in (4.37).

4.6.2 The Load Impedance

The load equivalent impedance will consist of the other three current controlled VSC and the load as given in (4.51).

$$\mathbf{Z_{cc}}(s) = \mathbf{Z_{cc,1}}(s) \parallel \mathbf{Z_{cc,2}}(s) \parallel \mathbf{Z_{cc,3}}(s) \parallel \mathbf{Z_{load}}(s) \tag{4.51}$$

4.7 The Single-Tone Approach

The analytically derived impedance model of the current controlled VSC from Section 4.3 is verified, as illustrated in Fig. 4.12, by injecting shunt current perturbations.

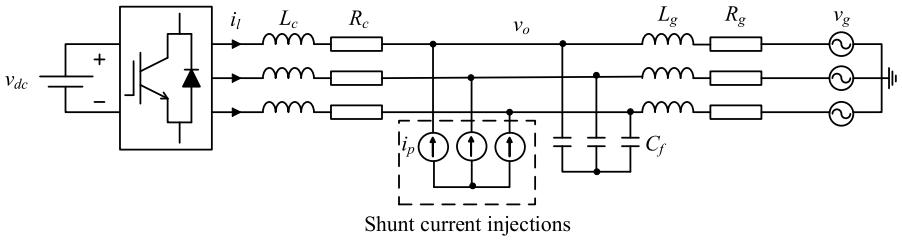

Figure 4.12: Impedance verification setup of a current controlled VSC based on shunt current injections.

Fig. 4.13 illustrates the algorithm of the single-tone approach which inject one current perturbation for every frequency [23]. The measured currents and voltages are then transformed to the dq-frame so that the FFT can be applied to analyze the contribution of the perturbation frequency. The impedances are calculated by dividing the voltage by the current at each frequency. In the following, every step of the single-tone approach is discussed as done in [62].

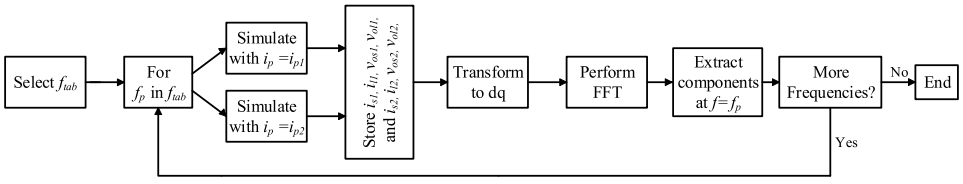

Figure 4.13: The algorithm of the single-tone approach.

4.7.1 Frequency Selection

A vector of frequencies, $f_{tab} = [f_1, f_2, ..., f_n]$, is chosen to decide the number of n iterations the algorithm will have. The frequencies are chosen arbitrary, but the value of the fundamental frequency, 50 Hz, should not be selected because the background voltages and currents with the same frequency will make it difficult to measure the contribution from the perturbation currents [63].

4.7.2 Simulations and FFT

The next step of the single-tone approach is to simulate the system n times for different current perturbations. The perturbations will give different responses on the source and load currents for every iteration. FFT must then be applied to extract the components at the perturbation frequency [64]. This process is further discussed and explained in the next section.

4.7.3 Calculating the Impedances

Fig. 4.14 illustrates the division of the load subsystem and source subsystem with corresponding equations in the dq-frame. The load and source voltages, $v_{ol}(s)$ and $v_{os}(s)$, are equal to each other and given in (4.52). The load and source impedances, $\mathbf{Z_l}(s)$ and $\mathbf{Z_s}(s)$, are given in (4.53) and the load, source and perturbation currents, $i_l(s)$, $i_s(s)$ and $i_p(s)$, are given in (4.54).

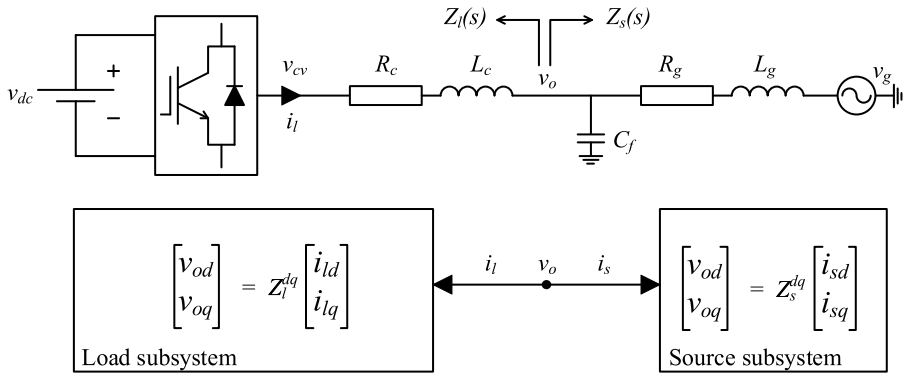

Figure 4.14: The system load and source impedances, with corresponding equations in the dq-frame.

$$v_o(s) = v_{os}(s) = v_{ol}(s) \begin{bmatrix} v_{od}(s) \\ v_{oq}(s) \end{bmatrix} \tag{4.52}$$

$$\begin{aligned} \mathbf{Z_l}(s) &= \begin{bmatrix} Z_{ldd}(s) & Z_{ldq}(s) \\ Z_{lqd}(s) & Z_{lqq}(s) \end{bmatrix} \\ \mathbf{Z_s}(s) &= \begin{bmatrix} Z_{sdd}(s) & Z_{sdq}(s) \\ Z_{sqd}(s) & Z_{sqq}(s) \end{bmatrix} \end{aligned} \tag{4.53}$$

$$i_s(s) = \begin{bmatrix} i_{sd}(s) \\ i_{sq}(s) \end{bmatrix}, \qquad i_l(s) = \begin{bmatrix} i_{ld}(s) \\ i_{lq}(s) \end{bmatrix}, \qquad i_p(s) = \begin{bmatrix} i_{pd}(s) \\ i_{pq}(s) \end{bmatrix} \tag{4.54}$$

It is needed two sets of linear independent perturbation currents to be able to estimate the four impedances. The perturbation signals are given in (4.55), where the first signal is a positive sequence perturbation and the other one is a negative sequence perturbation [3]. The magnitude of the perturbation, $I_{p,mag}$, should be approximately 5% of the AC base current. ω_p is the perturbation frequency and ϕ_p is an arbitrary chosen angle that has to change between the two perturbation sequences.

$$\begin{aligned} i_{p1}^{abc} &= I_{p1,mag} \begin{bmatrix} \sin\left((\omega_p + \omega_g)t + \phi_{p1}\right) \\ \sin\left((\omega_p + \omega_g)t - \frac{2\pi}{3} + \phi_{p1}\right) \\ \sin\left((\omega_p + \omega_g)t + \frac{2\pi}{3} + \phi_{p1}\right) \end{bmatrix} \\ i_{p2}^{abc} &= I_{p2,mag} \begin{bmatrix} \sin\left((\omega_p + \omega_g)t + \phi_{p2}\right) \\ \sin\left((\omega_p + \omega_g)t + \frac{2\pi}{3} + \phi_{p2}\right) \\ \sin\left((\omega_p + \omega_g)t - \frac{2\pi}{3} + \phi_{p2}\right) \end{bmatrix} \end{aligned} \tag{4.55}$$

The two perturbations give different responses on i_{sd}, i_{sq}, i_{ld}, i_{lq}, v_{od} and v_{oq}, which are necessary to retrieve to estimate the load and source impedances. In the following, the subscripts "1" and "2" denote the positive and negative sequence perturbations, respectively. By injecting the two different perturbations, the voltages can be estimated as in (4.56).

$$\begin{aligned} \begin{bmatrix} v_{od1}(s) \\ v_{oq1}(s) \end{bmatrix} &= \begin{bmatrix} Z_{ldd}(s) & Z_{ldq}(s) \\ Z_{lqd}(s) & Z_{lqq}(s) \end{bmatrix} \begin{bmatrix} i_{ld1}(s) \\ i_{lq1}(s) \end{bmatrix} \\ \begin{bmatrix} v_{od2}(s) \\ v_{oq2}(s) \end{bmatrix} &= \begin{bmatrix} Z_{ldd}(s) & Z_{ldq}(s) \\ Z_{lqd}(s) & Z_{lqq}(s) \end{bmatrix} \begin{bmatrix} i_{ld2}(s) \\ i_{lq2}(s) \end{bmatrix} \end{aligned} \tag{4.56}$$

The impedances of the two equations in (4.56) are the same since the frequency of the systems are the same through both perturbations [65]. The equations of (4.56) can be regrouped as in (4.57).

$$\begin{bmatrix} v_{od1}(s) \\ v_{od2}(s) \end{bmatrix} = \begin{bmatrix} i_{ld1}(s) & i_{lq1}(s) \\ i_{ld2}(s) & i_{lq2}(s) \end{bmatrix} \begin{bmatrix} Z_{ldd}(s) \\ Z_{ldq}(s) \end{bmatrix}$$
$$\begin{bmatrix} v_{oq1}(s) \\ v_{oq2}(s) \end{bmatrix} = \begin{bmatrix} i_{ld1}(s) & i_{lq1}(s) \\ i_{ld2}(s) & i_{lq2}(s) \end{bmatrix} \begin{bmatrix} Z_{lqd}(s) \\ Z_{lqq}(s) \end{bmatrix} \tag{4.57}$$

The load impedances can now be calculated as in (4.58).

$$\begin{bmatrix} Z_{ldd}(s) \\ Z_{ldq}(s) \end{bmatrix} = \begin{bmatrix} v_{od1}(s) \\ v_{od2}(s) \end{bmatrix} \begin{bmatrix} i_{ld1}(s) & i_{lq1}(s) \\ i_{ld2}(s) & i_{lq2}(s) \end{bmatrix}^{-1}$$
$$\begin{bmatrix} Z_{lqd}(s) \\ Z_{lqq}(s) \end{bmatrix} = \begin{bmatrix} v_{oq1}(s) \\ v_{oq2}(s) \end{bmatrix} \begin{bmatrix} i_{ld1}(s) & i_{lq1}(s) \\ i_{ld2}(s) & i_{lq2}(s) \end{bmatrix}^{-1} \tag{4.58}$$

Lastly, equation (4.58) can again be regrouped as in (4.59).

$$\begin{bmatrix} Z_{ldd}(s) & Z_{ldq}(s) \\ Z_{lqd}(s) & Z_{lqq}(s) \end{bmatrix} = \begin{bmatrix} i_{ld1}(s) & i_{lq1}(s) \\ i_{ld2}(s) & i_{lq2}(s) \end{bmatrix} \begin{bmatrix} v_{d1}(s) & v_{d2}(s) \\ i_{q1}(s) & i_{q2}(s) \end{bmatrix} \tag{4.59}$$

An expression of the load impedance is now derived and can be found by simulations. The exact same process can be done for the source impedance.

4.7.4 DQ-Frame Impedance Verification of the Current Controlled VSC

As mentioned in the introduction, it is important to verify that the analytical impedance model describes the nonlinear system with a sufficient accuracy. If the match between the analytical and actual impedance deviates from each other, it would not be expedient to apply the impedance-based method to analyze the stability. Therefore, to ensure that the impedance-based stability analysis can predict the stability with high certainty, the impedance model of the current controlled VSC found in Section 4.3 is compared to numerical simulations using the single-tone approach.

Fig. 4.15 shows the result of the impedance verification. The solid line represents the frequency response of the analytical impedance model, while the dotted line represents the frequency response of the numerical simulations. As discussed in Section 4.2, the stable operations of a grid-connected VSC is maintained by having a low grid impedance and a high converter impedance. This is recognized in Fig. 4.15 for the diagonal elements, where the black and green line is lower than the blue and red line for almost all frequencies. There is a good agreement between the black and green line who shows the simulated and analytical frequency response of the grid impedance. It is also a good agreement between the red and blue line that shows the converter impedance. The only

exception is that it can be observed a deviation for low frequencies for the off diagonal elements of the converter impedance. It can be because the phase shift of the off-diagonal elements are ignored in the analytical calculations and that the anti-aliasing filter is neglected.

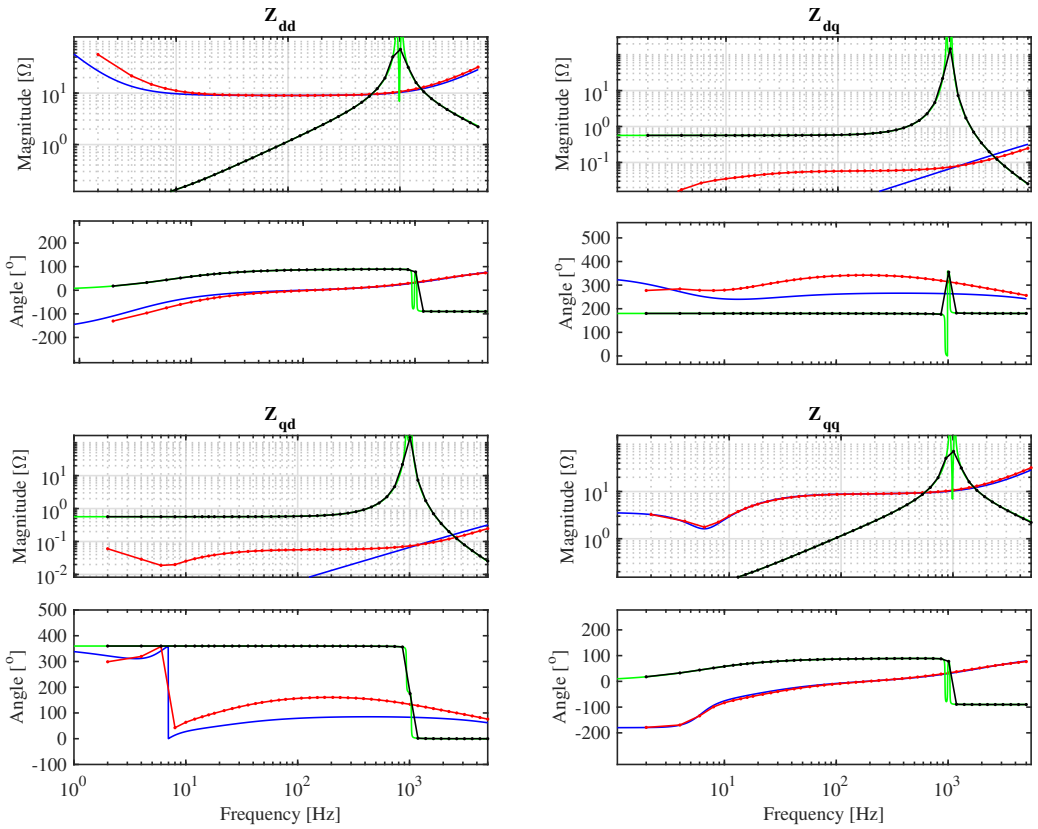

Figure 4.15: A comparison of the simulated and analytical impedances.

Chapter 5

Impedance-Based Stability Analysis

This chapter apply the impedance-based stability method on a single current controlled VSC, a single AC voltage controlled VSC, a grid-connected microgrid and an islanded microgrid to discover the sources of instability. By applying the GNC, it is possible to predict the stability of the system. The literature especially points out that a high grid impedance and the parameters of the control loops might have a negative affect on the system stability. The predicted instability is further verified by time domain simulations.

5.1 Introduction

As microgrids are a part of the future power grid solution, a large proportion of integrated power electronics is essential. This emphasizes the importance of the possibility to perform preliminary assessment of the stability of a system. There are several sources to instability in a power electronics dominated power system. Among others, a large grid impedance can cause instability or harmonic resonance between the grid and the VSC by destabilizing the current control loop. It has also been proven that the PLL leads to system instability and that the parameters of the PI-controller of the current controller might influence the stability. There can also arise stability issues when connecting several VSCs in parallel because the control loops might interact with each other. By applying the GNC on the ratio, the stability can be predicted based on the Nyquist plot. A system is predicted to be stable if the Nyquist plot does not encircle the point $(-1, j0)$ and if the phase margin, which indicates the stability strength of the system, is sufficiently high enough, preferably above 35°.

This chapter will utilize the impedance models retrieved in Chapter 4 to investigate sources of instability in power electronics dominated systems. Section 5.2 analyzes the stability of a grid-connected VSC based on a current controlled strategy. It discusses the effect of increasing the grid impedance and changing the controller parameters of the current controller and PLL. A stability analysis of the grid-connected microgrid is presented in Section 5.3. First, the microgrid is simulated with a variable power

input to take the intermittent solar and wind power into account. Furthermore, the impedance-based stability method is used to see how a weak grid and changing the control parameters affect the stability of the microgrid. Section 5.4 and 5.5 analyzes the stability of an AC voltage controlled VSC and an islanded microgrid, respectively. The predicted stability of all the cases are verified by time domain simulations. Lastly, a discussion of the findings are presented in Section 5.6.

5.2 Impedance-Based Stability Analysis of the Current Controlled VSC

In this section, the stability of the current controlled VSC introduced in Chapter 2 is analyzed for different cases. The GNC is applied to the ratio of the grid and converter impedance model given in Section 4.3, and the predicted stability is verified by time domain simulations.

5.2.1 Stable Case

The stable case is based on the system and control parameters given in Table 2.1, 2.2 and 2.3. Fig. 5.1a presents the eigenvalues λ_1 and λ_2, more commonly known as the characteristics loci of the minor loop gain. The plot does not encircle the point $(-1, j0)$ and has a sufficiently high phase margin of 107°. The system is therefore predicted to be stable, which is validated through time domain simulations in Simulink. Fig. 5.1b shows the three-phase grid currents and PCC voltages when there is a step change from 0.8 pu to 1.0 pu in current reference at 0.5 seconds. As predicted, the system operates stably through the step change. The voltages stay unaffected through the change, except some small disturbances at 0.5 seconds and the currents are able to quickly follow the step change in current reference.

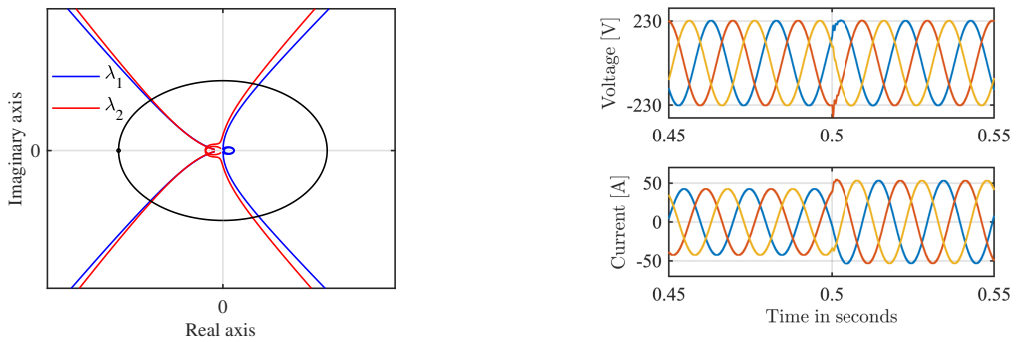

(a) (b)

Figure 5.1: (a) Nyquist plot and (b) time domain simulations for the stable case of the current controlled VSC.

5.2.2 Impact of the Grid Impedance

The stability of the current controlled VSC when connected to a weak grid is now analyzed. From Chapter 3, the system is already predicted to be unstable from the eigenvalue-based stability analysis when the grid impedance between the converter and the stiff grid is increased from 0.16 pu to 1.0 pu. Fig. 5.2a shows the characteristics loci of the minor loop gain when applying the impedance-based stability analysis. It is observed that λ_2 is now encircling the point $(-1, j0)$ and have a low phase margin of $-7.46°$. The open loop system has a pole in the RHP and the system is therefore predicted to be unstable, which is verified by time domain simulations in Fig. 5.2b. The three-phase currents and voltages are out of phase and not able to follow the desirable value.

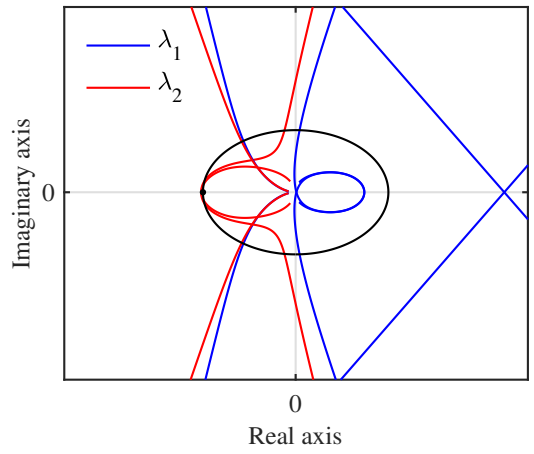

(a)

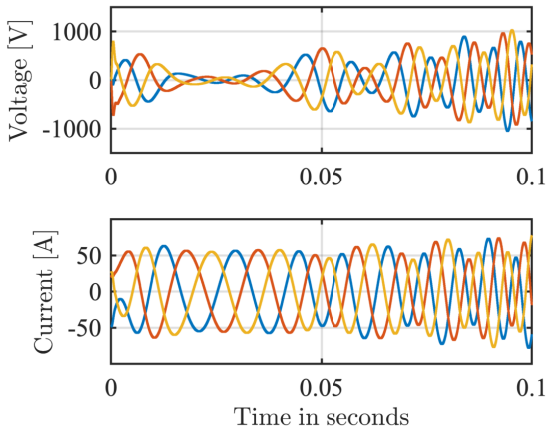

(b)

Figure 5.2: (a) Nyquist plot and (b) time domain simulations when $L_g = 1.0$ pu.

5.2.3 Impact of the Current Controller Proportional Gain

To see how the performance of the current controller affect the stability of the system, the proportional gain, k_{pc}, is decreased to 1% of its original value. It is interesting to see if the stability of the the open loop transfer function of the inner current control loop is affected by this change. The Bode plot in Fig. 5.3 has a gain margin of 89.7° at 12.7 Hz and has infinity gain margin at infinity Hz, which causes the closed loop system of the current controller to stay stable with a change in k_{pc}.

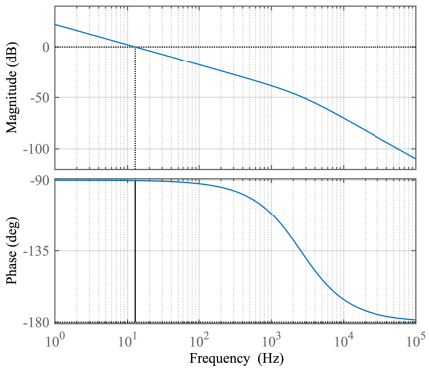

Figure 5.3: Bode plot of inner current controller when k_{pc} is decreased to 1 % of original value.

Fig. 5.4a shows the characteristics loci of the minor loop gain. λ_2 is encircling the point $(-1, j0)$ with a phase margin of $-1.76°$, which predicts an unstable system. This means that a change in k_{pc} does not necessarily mean that the current controller itself is unstable, but it can affect the stability of the whole system. The instability is confirmed by the time domain simulations in Fig. 5.4b, where it can be observed that the three-phase currents and voltages are out of phase and not pure sinusoidal.

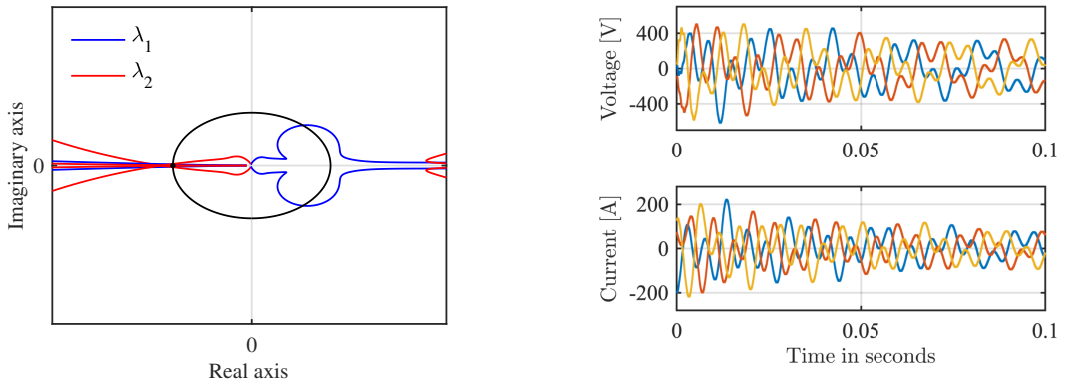

(a) (b)

Figure 5.4: (a) Nyquist plot and (b) time domain simulations when k_{pc} is decreased to 1 % of original value.

5.2.4 Impact of the PLL Integral Gain

The impact of the PLL on the stability is now investigated. The integral gain of the PLL is increased until its 25 times larger than its original value. Fig. 5.5 shows that the open loop system of the PLL will remain stable through the change with a phase margin of 37.9° at 6.88 Hz and a gain margin of minus infinity at 0 Hz. This is the same characteristics as with the Bode plot found in Fig. 2.12 in Chapter 2 and causes the closed loop transfer system to stay stable as well.

The corresponding Nyquist plot in Fig. 5.6a, on the other hand, predicts an unstable system with a phase margin of $-2.62°$. This is confirmed by time domain simulations in Fig. 5.6b, where the three-phase grid currents and PCC voltages are out of phase and not pure sinusoidal. As with the impact of the current controller gain, the PLL gain does not necessarily affect the stability of the closed loop system of the PLL, but it affects the stability of the whole system.

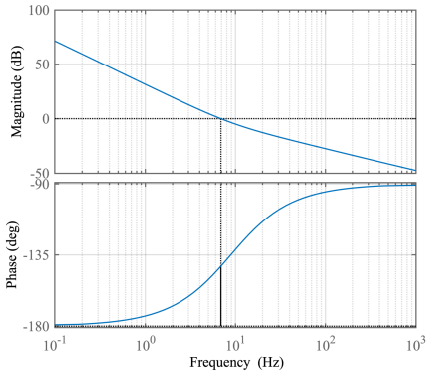

Figure 5.5: Bode plot of PLL when k_{ipll} is 25 times larger than original value.

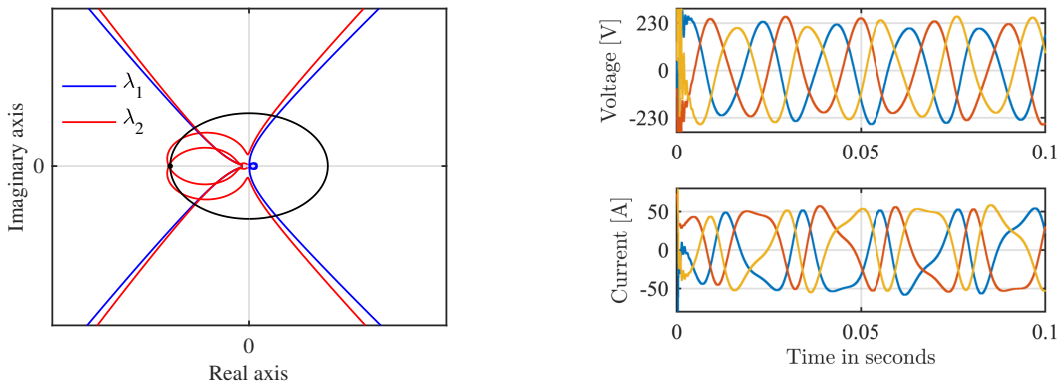

(a) (b)

Figure 5.6: (a) Nyquist plot and (b) time domain simulations when k_{ipll} is 25 times larger than original value.

5.3 Impedance-Based Stability Analysis of the Grid-Connected Microgrid

In this section, the stability of the grid-connected microgrid introduced in Chapter 2 is analyzed for different cases. First, simulations of the microgrid is completed for a variable power input to resemble the intermittent power sources as wind and solar power. Furthermore, the GNC is applied to the impedance ratio derived for the grid-connected microgrid in Section 4.4. Lastly, the predicted stability is verified by time domain simulation.

5.3.1 Impact of Intermittent Power Sources

When analyzing the stability by applying the impedance-based method, the impedance models are derived assuming that all microsources and loads produce or consume a constant amount of power. In real life this is not likely due to the intermittent characteristic of solar and wind power. To look at how the system reacts to the intermittent sources, it is simulated with a variable power input for the solar and wind converter. Fig. 5.7a shows the variable output of the solar power unit, which is built to resemble the solar radiation during a day, with no solar radiation during night, and then increasing radiation until noon before it decreases again. The figure further shows the d- and q-axis current response to the variable reference input. Fig. 5.7b verifies that the three-phase PCC currents react quickly and accurate to this change.

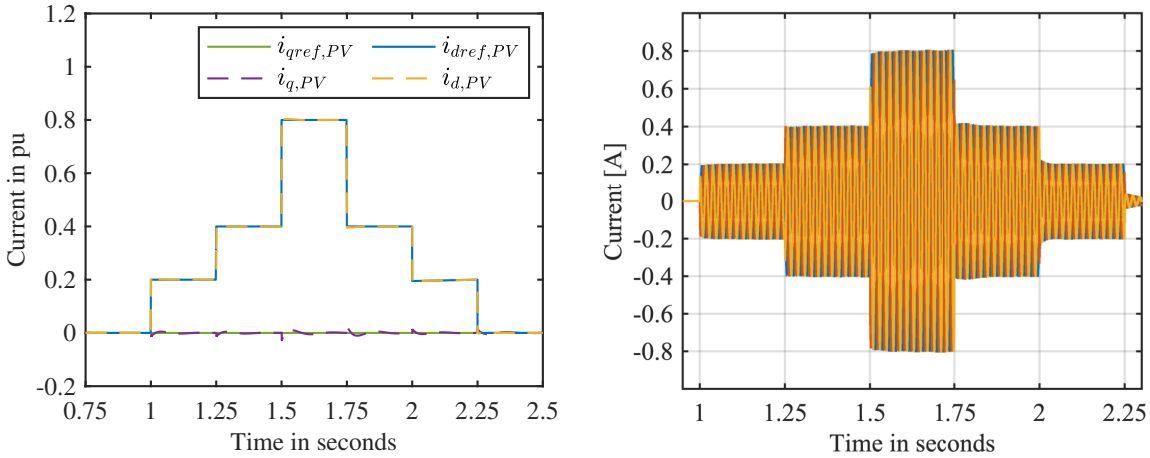

(a) (b)

Figure 5.7: (a) d- and q-axis currents and (b) three-phase PCC currents for a variable current reference of the PV.

The variable output from the wind power in Fig. 5.8a carries more character of randomness. The wind, as a power source is very unpredictable and changes quickly, sometimes with big steps. For instance, at 1.75 seconds the output power changes from 0.2 to 0.8 pu. However, although it is a step change of 0.6 pu, the d-axis current of the wind converter is able to follow the reference, while the q-axis current continues to equal zero. Fig. 5.8b validates that the three-phase PCC currents are able to quickly follow the change in reference with no disturbances.

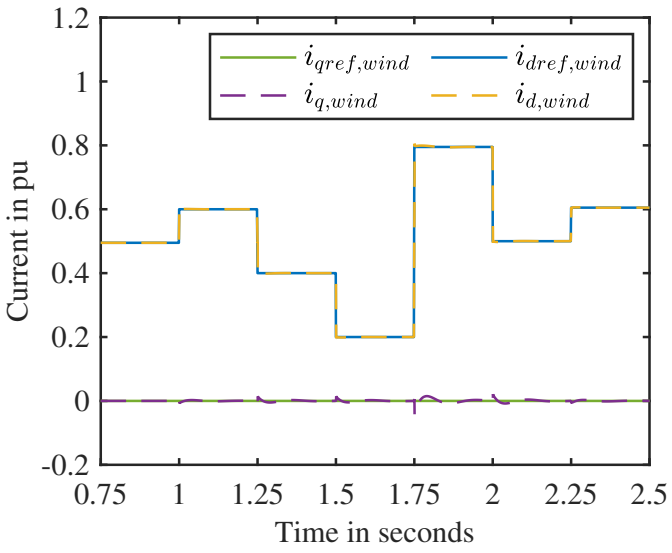

(a)

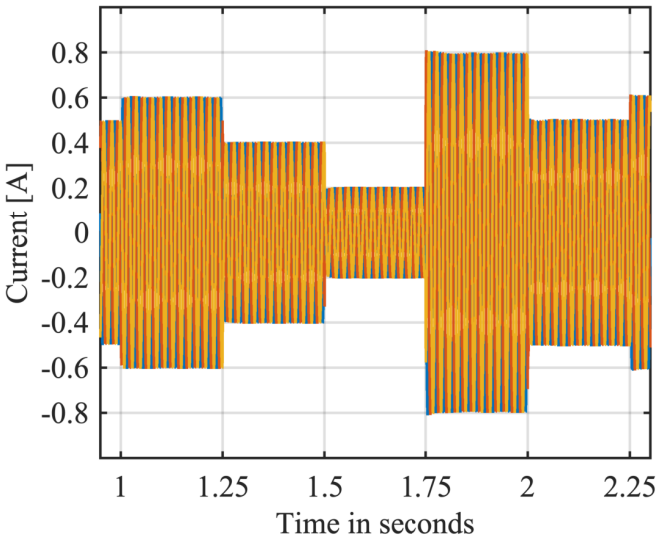

(b)

Figure 5.8: (a) d- and q-axis currents and (b) three-phase PCC currents for a variable current reference of the wind power.

Lastly, Fig. 5.9a shows how the three-phase PCC voltages and grid currents react to the intermittent power sources. And as with the single VSC, the three-phase currents quickly changes from one reference value to another. The three-phase PCC voltages on the other hand, stays unaffected through the changes as desired. Fig. 5.9b shows a zoomed view of the step change in current reference at 1.5 seconds from 0.4 to 0.2 pu. As can be observed the three-phase PCC voltages keep constant, while the three-phase grid currents quickly change without any disturbances.

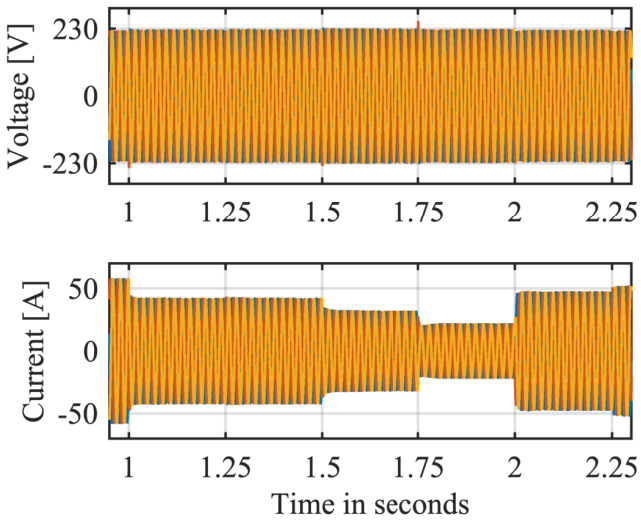

(a)

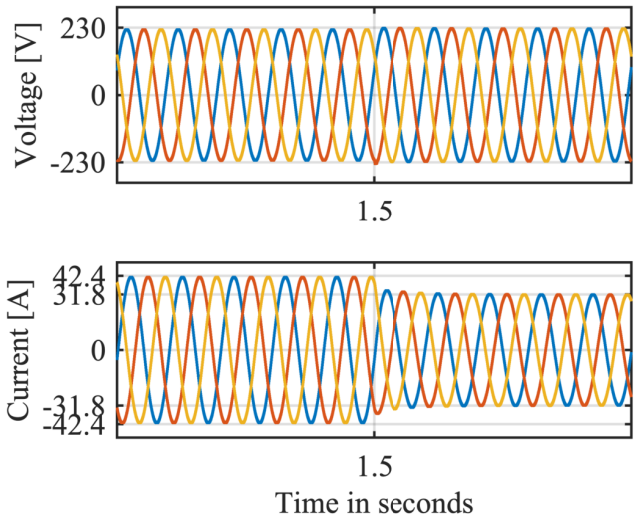

(b)

Figure 5.9: Three-phase PCC voltages and grid currents (a) full view and (b) zoomed view.

5.3.2 Stable Case

For the rest of the stability analysis, the impedance-based method is applied to the impedance ratio of the system, and it is assumed that the microsources and loads produce or consume a constant amount of power. For simplicity, each individual VSC has the same converter and controller parameters as the single VSC analyzed in Section 5.2, the only thing that separates them is the current reference. The different current references are already chosen according to Table 2.4. However, to repeat, the reference current of the PV is 0.4 pu, while it is 0.2 pu for the wind power, -0.7 pu for the IG and -0.2 pu for the BESS.

Fig. 5.10a shows the Nyquist plot of the given stable case. The characteristics loci of the minor loop gain does not encircle the point $(-1, j0)$ and the phase margin is 103°. The predicted stability is further verified by time domain simulations in Fig. 5.10b. It shows the PCC voltages and grid currents of the grid-connected microgrid and as can be observed the three-phase currents and voltages operate at 1.0 pu.

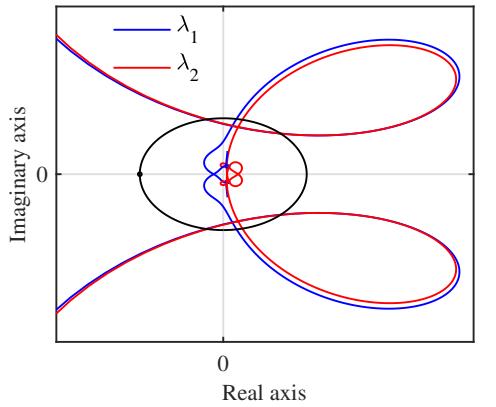

(a)

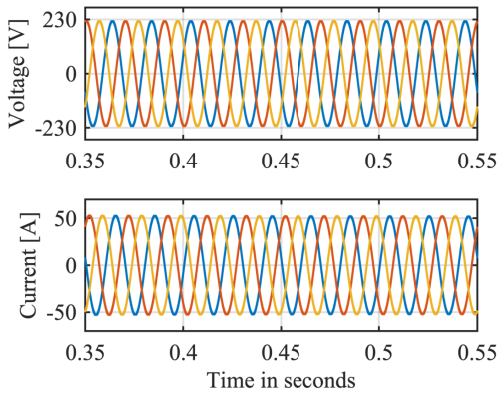

(b)

Figure 5.10: (a) Nyquist plot and (b) time domain simulations for the stable case of the grid-connected microgrid.

5.3.3 Impact of the Grid Impedance

The stability of a grid-connected microgrid when connected to a weak grid is now analyzed. In Fig. 5.11a the grid inductance, L_g, is increased to 0.7 pu. As can be observed, λ_1 just encircles the point $(-1, j0)$ with a phase margin of $-5.73°$.

To see how the system stability reacts to the same change in grid impedance as for the single current controlled VSC, L_g is further increased to 1.0 pu in Fig. 5.11b. As can be seen, λ_1 is now encircling the point $(-1, j0)$ with an even more negative gain margin of $-37.1°$. Compared to the single grid-connected VSC, this insinuates that the stability of a grid-connected microgrid with several VSCs is more prone to stability issues due to connections to a weak grid. Fig. 5.12 shows the three-phase PCC currents and voltages and verifies the predicted instability when $L_g = 0.7$ pu. The three-phase signals are out of phase and are not able to reach the desirable value.

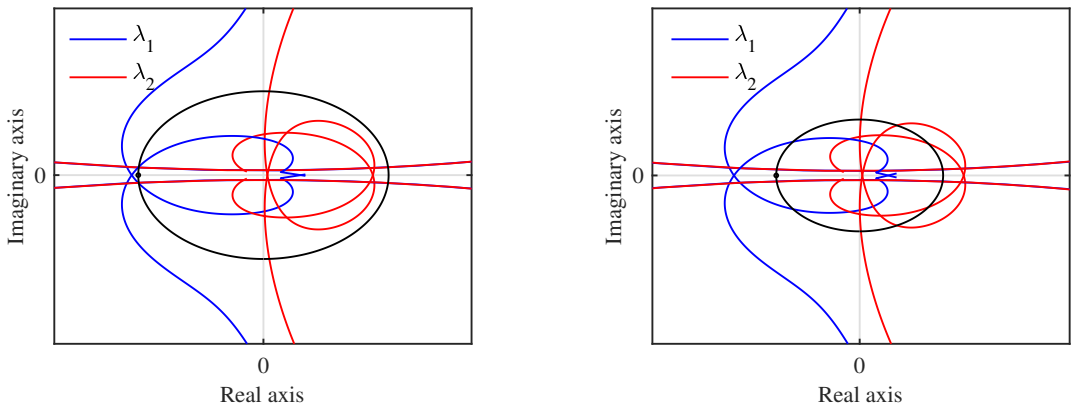

Figure 5.11: Nyquist plot of the grid-connected microgrid when (a) $L_g = 0.7$ pu and (b) $L_g = 1.0$ pu.

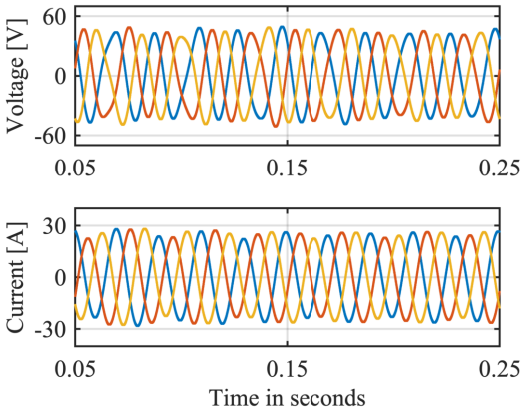

Figure 5.12: Time domain simulations when $L_g = 0.7$ pu.

5.3.4 Impact of the Current Controller Proportional Gain

The grid-connected microgrid is constituted by cascaded VSCs that are based on a current controlled strategy. It is therefore interesting to see how stable operations of the microgrid depend on the performance of the current control loops. First, in Fig. 5.13, the proportional gain of the BESS converter, $k_{pc,BESS}$, is decreased to 1% of its original value. That is, the proportional gain of the current control system of the wind power, PV and IG remains the same.

From Subsection 5.2.3, it can be recalled that the same decrease in proportional gain of the single VSC made the system unstable. However, the corresponding Nyquist plot in Fig. 5.13a, shows that neither λ_1 nor λ_2 encircles the point $(-1, j0)$, which means that the grid-connected microgrid stays stable. The small phase margin of 6.32°, on the other hand, indicates that even if the system operates stable, a small step in current reference could affect the stability. This is shown in Fig. 5.13b, where grid currents and PCC voltages are shown when a step is applied after 1.0 second. The result is an unstable system with currents out of phase.

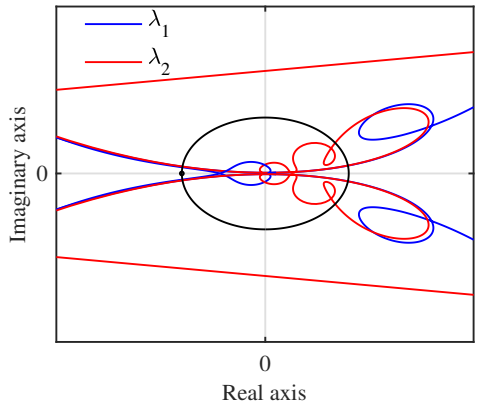

(a)

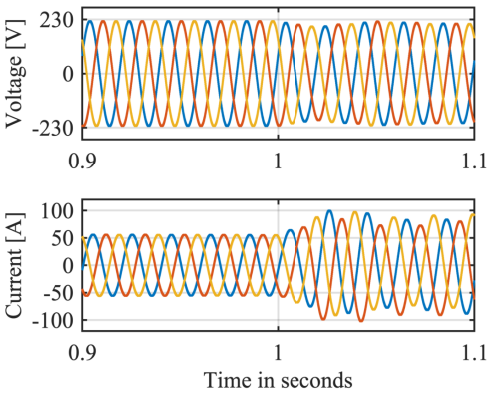

(b)

Figure 5.13: (a) Nyquist plot and (b) time domain simulations when $k_{pc,BESS}$ is 1% of its original value.

Fig. 5.14 shows the case where the proportional gain of the current control loop of both the BESS and IG is reduced to 1% of its original value. This means that two of the current control loops have changed the value of k_{pc}, while the two other control loops keep the original value. λ_1 of the Nyquist plot of Fig. 5.14a encircles the point $(-1, j0)$ with a phase margin of $-13.6°$, which means that the system is predicted to be unstable. This is confirmed by time domain simulations of PCC currents and voltages in Fig. 5.14b.

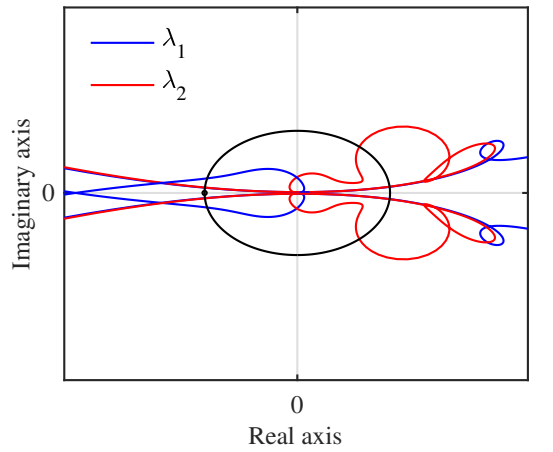

(a)

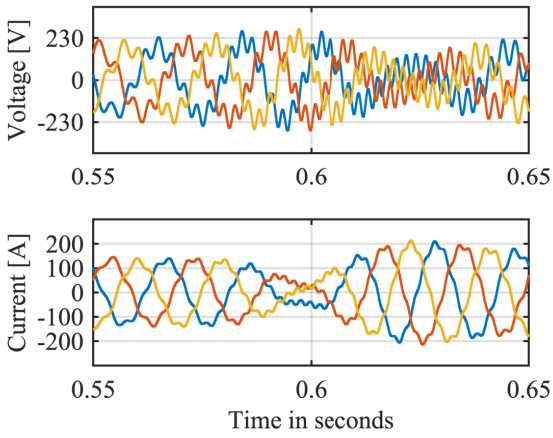

(b)

Figure 5.14: (a) Nyquist plot and (b) time domain simulations when $k_{pc,BESS}$ and $k_{pc,IG}$ is 1% of its original value.

To sum up, the grid-connected microgrid can withstand one of the current controller proportional gains to change, even though the result is that the stability of the system is fragile and do not tolerate a step change in the current. However, if two out of four proportional gains are changed, the system will be unstable.

5.3.5 Impact of the PLL Integral Gain

The impact of the integral gain of the PLL control loop is now investigated. First, k_{ipll} of three of the converters are changed to 40 times its original value, while the integral gain of the PV keeps its original value. Fig. 5.15a shows the characteristics loci of the minor loop gain of this case, and as can be observed, neither λ_1 nor λ_2 encircles the point $(-1, j0)$. With a sufficient high phase margin of 98.4° the system is therefore predicted to be stable, which is confirmed by time domain simulations of the three-phase grid currents and PCC voltages in Fig. 5.16b

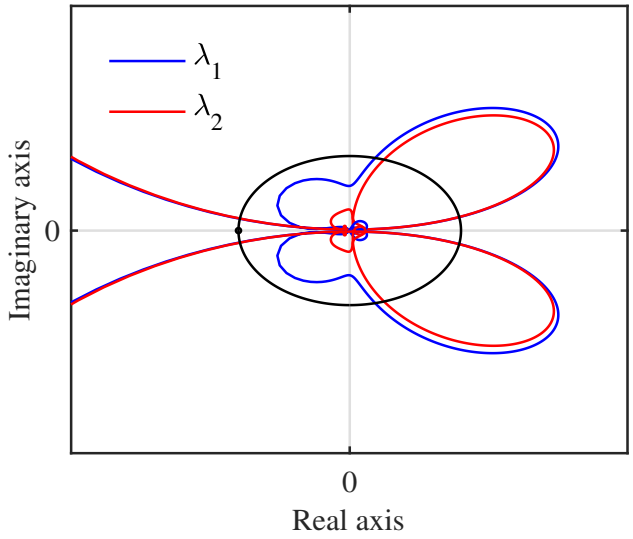

(a)

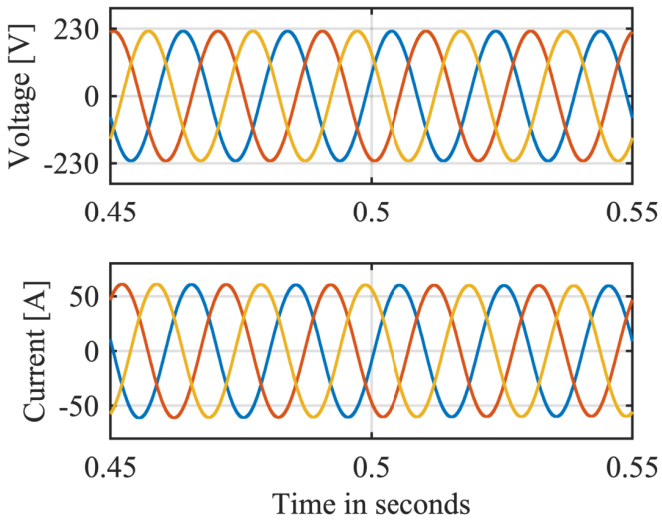

(b)

Figure 5.15: (a) Nyquist plot and (b) time domain simulations when k_{ipll} of all converters except the PV are changed to 40 times its original value.

In Fig. 5.16 all of the integral gains of the PLL control loops are changed to 40 times its original value. Fig. 5.16a shows the Nyquist plot of this case. As can be observed, λ_1 encircles the point $(-1, j0)$ with a phase margin of $-16.9°$ and the system is predicted to be unstable. This is confirmed by time domain simulations in Fig. 5.16b. The three-phase grid currents and PCC voltages are out of phase and not pure sinusoidal. In addition, the currents are almost twice as high as the original operating point at 1.0 pu.

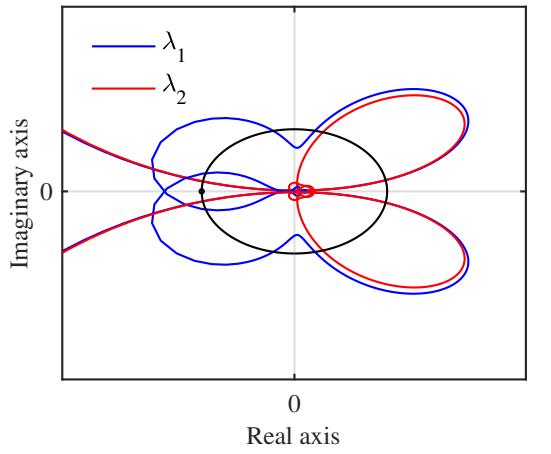

(a)

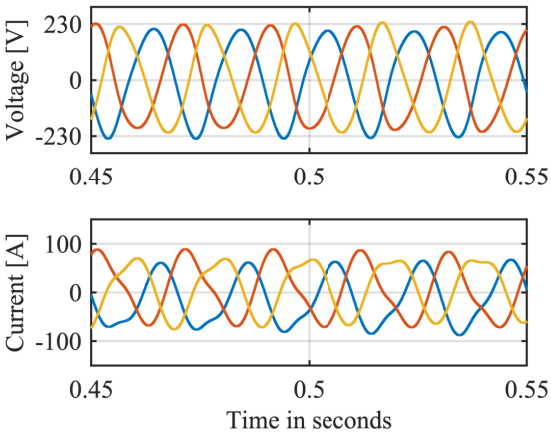

(b)

Figure 5.16: (a) Nyquist plot and (b) time domain simulations when k_{ipll} of all converters are changed to 40 times its original value.

In Section 5.2, the stability of a single grid-connected VSC was analyzed. To destabilize the system, the integral gain of the PLL had to be multiplied with 25. From the analyze above, it is shown that for a grid-connected microgrid, the integral gain of all converters must be changed for the system to experience instability. In addition, the k_{ipll} must be multiplied by 40 rather than 25 to affect the stability. This lead to the conclusion that it is more demanding to destabilize a cascaded system than a single VSC by changing the integral gain of the PLL.

5.4 Impedance-Based Stability Analysis of the AC Voltage Controlled VSC

In this section, the stability of the single AC voltage controlled VSC introduced in Chapter 2 is investigated for different cases. The GNC is applied to the ratio of the converter impedance and load equivalent impedance as given in Section 4.5. First the impedance-based stability analysis is applied to the stable case, before the impact of the load impedance and the proportional gain of the current controller is researched.

5.4.1 Stable Case

The Nyquist plot of the stable case is given in Fig. 5.17a. The characteristics loci of the minor loop gain does not encircle the point $(-1, j0)$, and has a sufficient phase margin of 208°. The system is therefore predicted to be stable, which is further verified by time domain simulations in Fig. 5.17b, where the PCC voltage reference experiences a step change from 0.9 to 1.0 pu after 0.5 seconds. The measured currents in the time domain simulations are also increased after 0.5 seconds to ensure the correct voltage level.

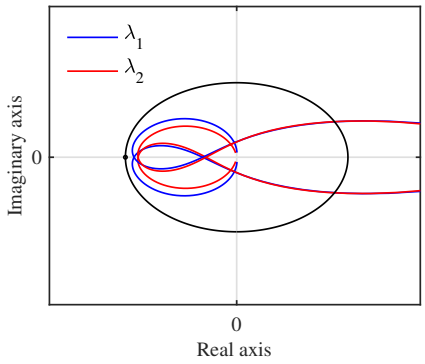

(a)

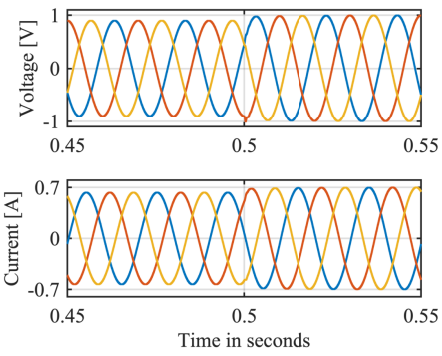

(b)

Figure 5.17: (a) Nyquist plot and (b) time domain simulations for the stable case of AC voltage controlled VSC.

5.4.2 Impact of the Load Impedance

The AC voltage controlled VSC is disconnected to the grid, and the size of the load impedance is therefore of importance to be able to obtain the correct voltage level. In this case the load resistance, R_l, is changed from 2.8 pu to 1.0 pu. A small load resistor requires a high current which might cause instability. Fig. 5.18a shows that the characteristics loci of the minor loop gain does encircle the point $(-1, j0)$ with a negative phase margin of $-32.5°$. The predicted instability is verified by time domain simulations of the PCC voltages and currents in Fig. 5.18b.

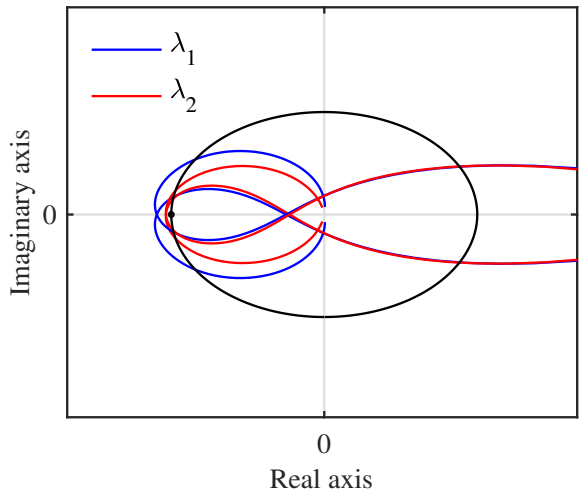

(a)

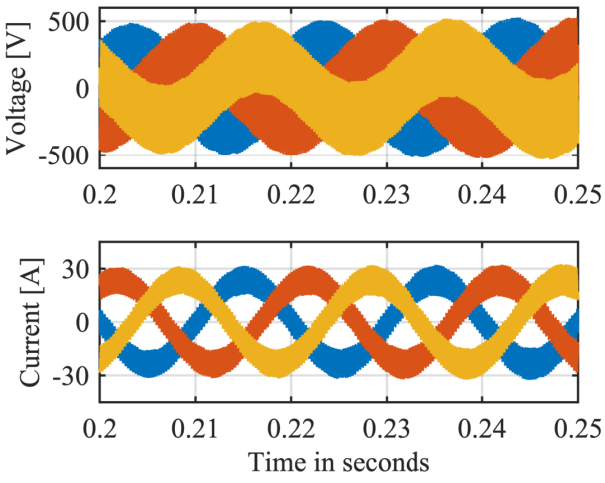

(b)

Figure 5.18: (a) Nyquist plot and (b) time domain simulations when decreasing R_l.

5.4.3 Impact of the AC Voltage Controller Proportional Gain

From Chapter 3, the system is already predicted to be unstable from the eigenvalue-based stability analysis when the proportional gain of the outer voltage control loop, k_{pvac}, is decreased to 1% of its original value. By applying the impedance-based stability analysis on the impedance ratio of the system, the Nyquist plot of Fig. 5.19a is retrieved. As can be observed λ_1 encircles the point $(-1, j0)$ with a phase margin of $-27.5°$ and the system is predicted to be unstable. This confirms the results from the eigenvalue-based stability analysis. The predicted stability from the analytical methods are further verified by time domain simulations in Fig. 5.18b.

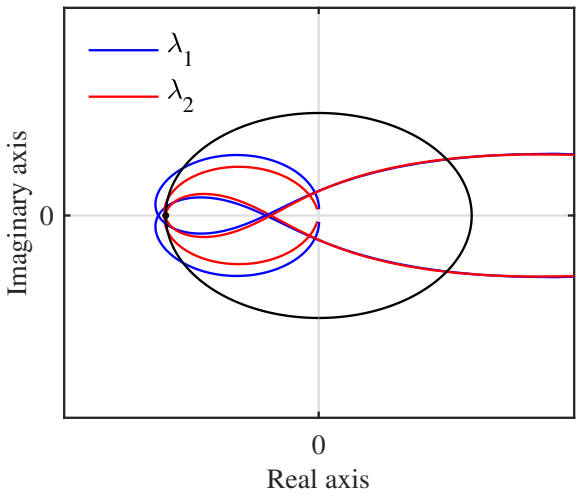

(a)

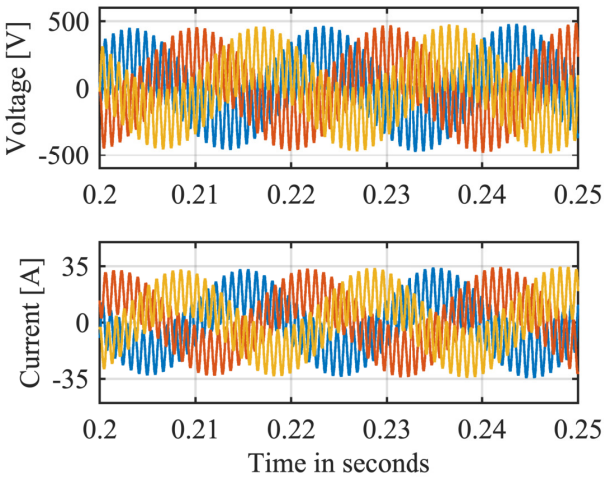

(b)

Figure 5.19: (a) Nyquist plot and (b) time domain simulations when decreasing k_{pvac} to 1% of original value.

5.5 Impedance-Based Stability Analysis of the Islanded Microgrid

In this section, the stability of the islanded microgrid introduced in Chapter 2 is analyzed for different cases. First, simulations of the microgrid is completed for a variable power input to resemble the intermittent wind and solar power sources. The GNC is applied to the ratio of the source impedance and load impedance as given in Section 4.6. First, the impedance-based stability analysis is applied to the stable case, before it is used to investigate the impact on the stability of the proportional gain of the current controller and the proportional gain of the AC voltage controller.

5.5.1 Impact of Intermittent Power Sources

The same variable input of wind and solar power as introduced for the grid-connected microgrid in Subsection 5.3.1 is applied to the islanded microgrid. When the microgrid is disconnected from the grid it can not receive compensation from the grid and it is therefore especially interesting to see how an islanded microgrid responds to a variable power input. An important factor, will be how the BESS is able to compensate for a high power input and a low power input, but first it is investigated how the solar power converter reacts to the variable power input.

Fig. 5.20a shows how the d- and q-axis currents of the PV converter respond to the variable reference input and Fig. 5.20b verifies that the three-phase PV currents react quickly and accurate to the change.

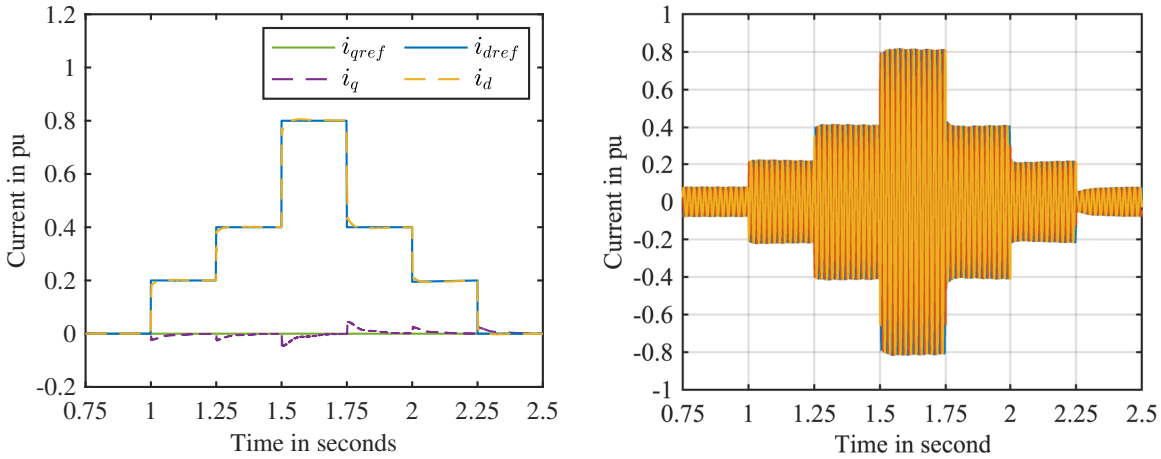

(a) (b)

Figure 5.20: (a) d- and q-axis currents and (b) three-phase currents for variable current reference of PV.

The impact of a variable power input of the wind power is now investigated. As reviewed in Subsection 5.3.1 the variable output of wind power carries more characteristics of randomness. Fig. 5.21a shows how the converter of the wind power unit respond quickly to the d- and q-axis reference current, despite large step changes. Fig. 5.21b validates that the three-phase converter currents are able to quickly follow the change in reference without any undesirable spikes or instability.

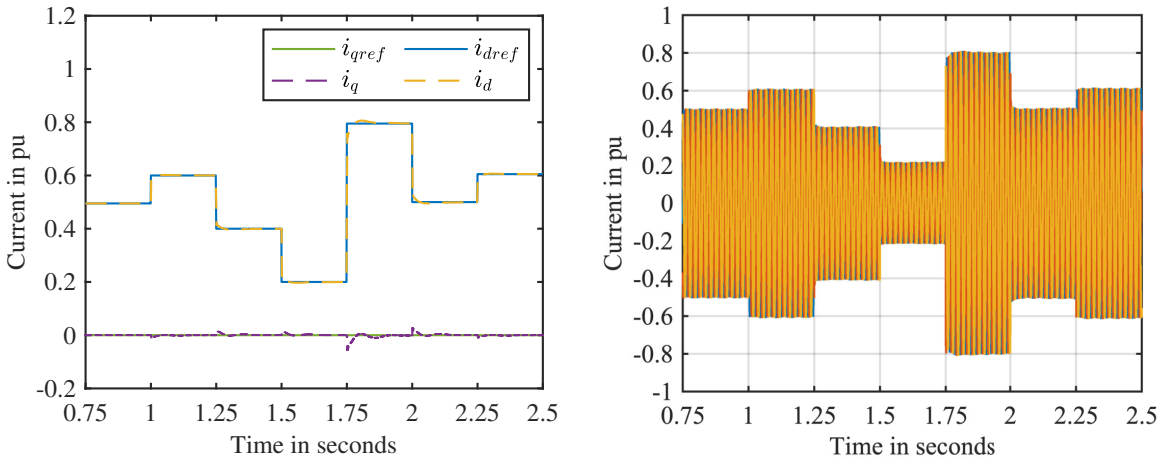

(a) (b)

Figure 5.21: (a) d- and q-axis currents and (b) three-phase currents for variable current reference of wind power unit.

Fig. 5.22a and 5.22b shows how the three-phase currents of the BESS changes in size according to the variable power input of the PV and wind power, respectively, to ensure a constant voltage level at the PCC. As can be observed the three-phase PCC voltages keep constant, while the three-phase currents quickly change without any disturbances.

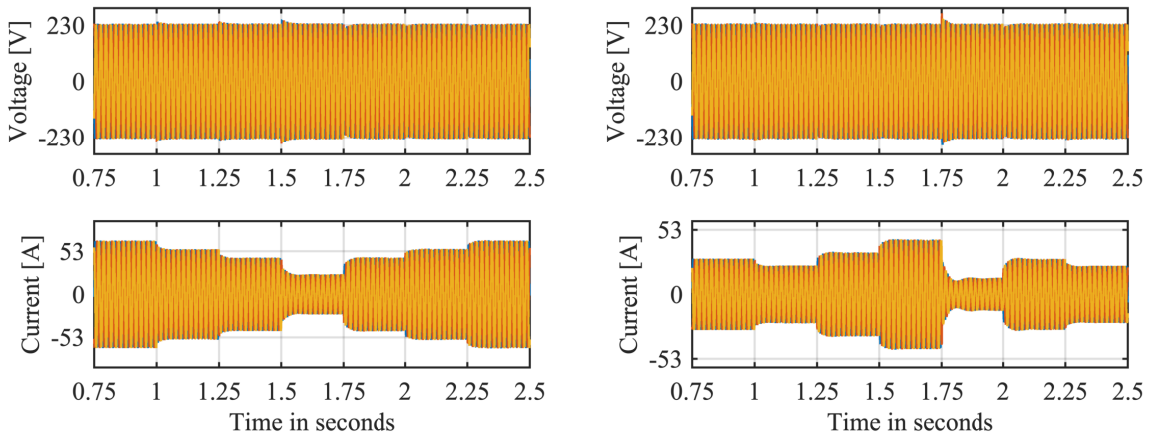

(a) (b)

Figure 5.22: Three-phase PCC voltages and BESS currents for variable reference input of (a) PV and (b) wind power.

5.5.2 Stable Case

For the rest of the stability analysis it will be assumed a constant current reference input according to Table. 2.4 of the three current controlled VSCs, which is the induction generator, solar power and wind power converter. For further simplicity, as with the grid-connected microgrid, all the system and converter parameters are the same for every VSC. Fig. 5.23a shows the Nyquist plot of the islanded microgrid for stable conditions. The characteristics loci of the minor-loop gain has a phase margin of 159° and does not encircle the point $(-1, j0)$, which means that there is no poles in the RHP of the open loop system, hence the system is predicted to be stable. The stability of the system is verified by time domain simulations of the PCC voltages and currents of the BESS in Fig. 5.23b. To emphasize the stability, a step change in the reference voltage from 0.9 pu to 1.0 pu is applied after 0.5 seconds. It can be observed that the BESS currents must be operated at 0.9 pu to obtain the desirable voltage level.

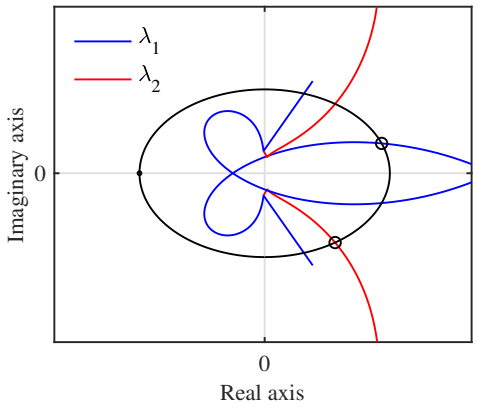

(a)

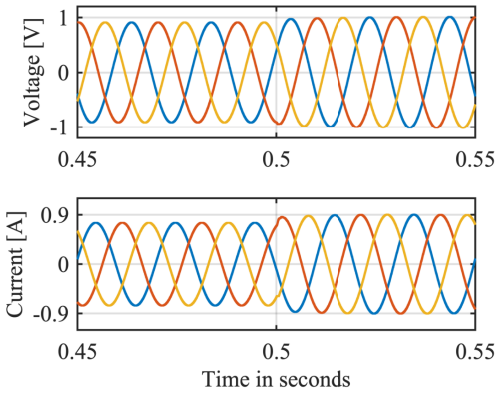

(b)

Figure 5.23: (a) Nyquist plot and (b) time domain simulations for the stable case of the islanded microgrid.

5.5.3 Impact of the Current Controller Proportional Gain

The impact on stability of the current controller proportional gain, k_{pc} is investigated in this subsection. The k_{pc} of both the BESS and the wind power unit is decreased to 1% of its original value. As can be observed from the Nyquist plot in Fig. 5.24a, λ_1 is now encircling the point $(-1, j0)$ with a phase margin of $-48.9°$. The open loop system has a pole in the RHP, and the system is predicted to be unstable. Fig. 5.24b verifies the predicted instability by time domain simulations of the PCC voltages and currents of the BESS.

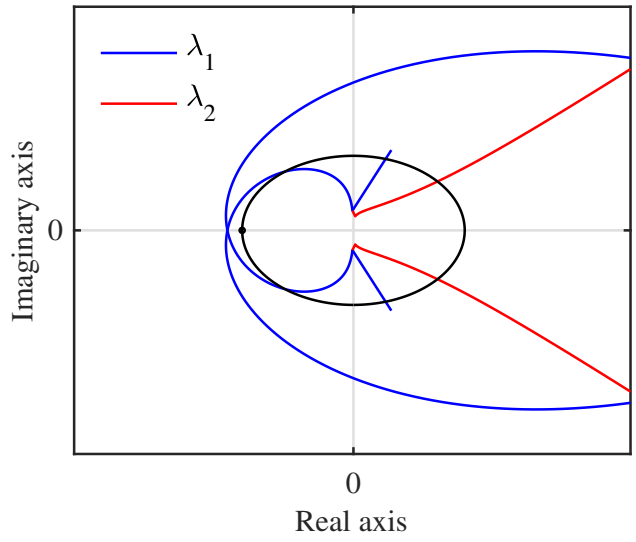

(a)

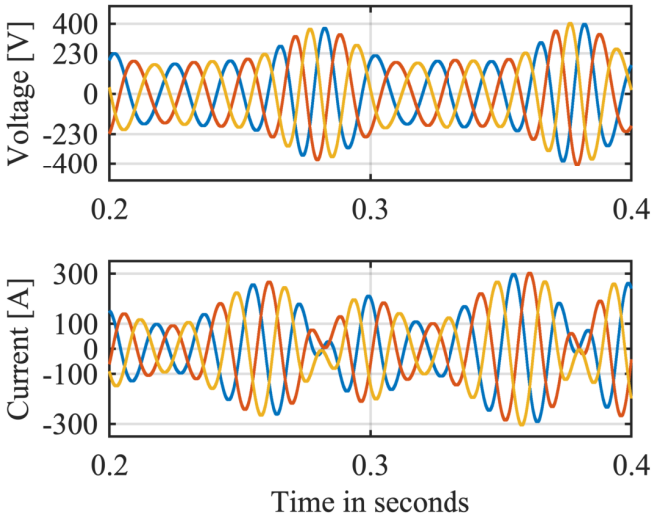

(b)

Figure 5.24: (a) Nyquist plot and (b) time domain simulations when k_{pc} of wind and BESS is changed to 1% of original value.

5.5.4 Impact of the AC Voltage Controller Proportional Gain

In the last case, the impact of the proportional gain of the AC voltage controller, k_{pvac}, is investigated. Fig. 5.25a shows the Nyquist plot of the impedance ratio of the islanded microgrid when the proportional gain is multiplied by 3. As can be observed, λ_2 is now encircling the point $(-1, j0)$ with a negative phase margin of $-19.2°$, and the system is therefore predicted to be unstable. This instability is further verified in Fig. 5.25b by time domain simulations of the three-phase PCC voltages and currents of the BESS.

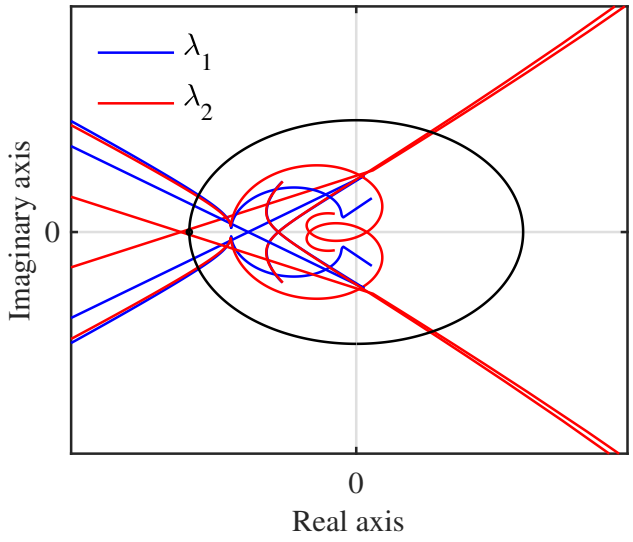

(a)

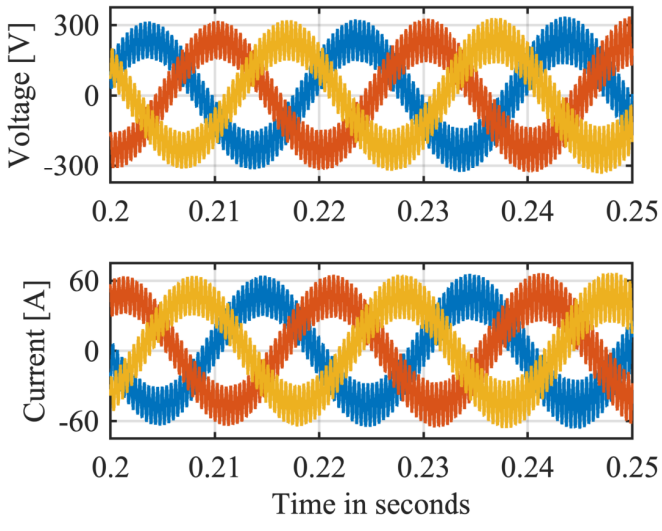

(b)

Figure 5.25: (a) Nyquist plot and (b) time domain simulations when k_{pvac} is multiplied by 3.

5.6 Discussion

The stability of different power electronics dominated systems has been investigated in this chapter, including (I) a current controlled VSC, (II) a grid-connected microgrid, (III) an AC voltage controlled VSC and (IV) an islanded microgrid. To predict the stability, the impedance-based stability analysis was applied to the four different impedance models obtained in Chapter 4. If the corresponding Nyquist plot did not encircle the point $(-1, j0)$ the system was predicted to be stable, and the stability strength of the systems was decided from the phase margin, which preferable should be over 35°. The predicted stability or instability from the Nyquist plot was verified for all cases by time domain simulations.

First, the stability of the current controlled VSC and the grid-connected microgrid was discussed. It is interesting to compare these two systems since the grid-connected microgrid is built up by several paralleled current controlled VSCs. The GNC was first applied to both systems for stable operations, where the predicted stability was verified by time domain simulations. Subsequently, the impact of a weak grid was discussed. A weak grid is introduced by a high grid impedance, which can destabilize the current controller which again can lead to sustained harmonic oscillations [17]. For the current controlled VSC an increase in grid inductance from 0.16 pu to 1.0 pu led to an unstable system with a Nyquist plot that just encircled the point $(-1, j0)$. The instability of the grid-connected microgrid, on the other side, was predicted to be more severe for the same increase in grid inductance. It was discovered that the Nyquist plot of the microgrid just encircled the point $(-1, j0)$ already at $L_g = 0.7$ pu. Based on this research, this means that a system can better withstand a weak grid if it has fewer VSCs connected to it.

Furthermore, the impact of the current controller proportional gain was investigated. Since both the grid-connected microgrid and the VSC is based on a current control strategy, it is especially interesting to observe how the current controller parameters might affect the stability. For the single current controlled VSC the propotional gain, k_{pc}, was decreased to 1% of its original value. The Bode plot of the open loop transfer function of the current controller was obtained, which concluded that the closed loop system would stay stable for this new value of k_{pc}. However, the Nyquist plot of the characteristics loci of the minor-loop gain predicted the system to be unstable, which means that a change in k_{pc} does not necessarily mean that the current controller itself is unstable, but it might affect the stability of the whole system. For the grid-connected microgrid, on the other hand, it was proven that the system will stay stable if one of the control system proportional gain is decreased to 1% of original value. However, the small phase margin of 6.32° suggested that the system could experience instability if there was a small step change in the reference current. This was confirmed by time domain simulations, where it was shown that the three-phase currents and voltages are stable until the step change in current reference. Furthermore it is shown that two of the current control loops constituting the grid-connected microgrid must be changed to 1% of its original value to make the system unstable. Based on this, it is clear that the microgrid can tolerate one of the current controller proportional gain to change, even though the system stability strength is weak. However, if two of the proportional gains

are changed, the system will be unstable.

It is proven that also the PLL parameters can affect the stability of a system [18]. The integral gain of the PLL was increased until it was 25 times larger than its original value, and as with the proportional gain of the current controller the open loop transfer function of the PLL showed that the change in k_{ipll} did not affect the stability of the closed loop system of the PLL. However, the Nyquist plot predicted the system to be unstable, which led to the same conclusion as with changing the proportional gain of the current controller, namely that the PLL integral gain does not necessarily affect the stability of the closed loop system of the PLL, but it can affect the stability of the whole system. The reason for this is that the PLL can be compared to a bridge [66] that propagate the small-signal perturbation in the system voltage to the duty cycle of the controller dq-frame. This will further affect the output current and voltage of the system dq-frame, that finally affects the output impedance of the converter. For the grid-connected microgrid it was shown that even if the integral gain of the PLL is increased for three of the four VSCs, the system will stay stable with a sufficient phase margin of 98.4°. However, when all of the integral gains are multiplied by 40, the Nyquist plot predicted an unstable system. Based on this research, it is shown that it is more demanding to destabilize a microgrid with several paralleled VSCs than a single VSC by changing the integral gain of the PLL.

When applying the impedance-based stability analysis it is assumed that the power input or output of the different microsources and loads are constant. Nevertheless, it is interesting to look at how the grid-connected and islanded microgrid reacts to a variable power input that resembles the intermittent solar and wind power. For both operating modes of the microgrid, it was observed that the d- and q-axis currents are able to follow its reference without any overdamped or underdamped characteristics. This was further verified by the three-phase currents and voltages, where the currents changed according to the variable power input, while the voltage at PCC stayed at the desirable value. For the islanded microgrid it was also interesting to see how the currents of the AC voltage controlled BESS changed to compensate for the variable power input.

The stability of the single AC voltage controlled VSC was further investigated. The GNC was first applied to the system for stable operations, where the predicted stability was verified by time domain simulations. The AC voltage controlled VSC is disconnected from the grid, and hence does not retrieve voltage and frequency regulation from the grid. It is therefore important that the load impedance on the AC side is of such magnitude that the desirable voltage level can be obtained. A low load impedance will require a high current which might cause instability. It was therefore considered interesting to look at the impact of the load resistor when it was decreased from 2.8 pu to 1.0 pu. As was observed, the characteristics loci of the minor loop gain encircled the point $(-1, j0)$ and the system was predicted to be unstable. Subsequently, the impact of the AC voltage controller proportional gain was discussed. When k_{pvac} was decreased to 1% of its original value, the Nyquist plot encircled the point $(-1, j0)$ and the system was predicted to be unstable.

Lastly the stability of the islanded microgrid was analyzed. A microgrid consists of

several VSCs in parallel, and different research [19, 20] has shown that this might cause instability because of interacting control loops. The impact of the current controller and AC voltage controller parameters was therefore further analyzed, but first the stable operations of the microgrid was verifed by the GNC and time domain simulations. When the current controller proportional gain, k_{pc}, of two of the VSCs was changed to 1% of its original value, the corresponding Nyquist plot predicted an unstable system. An unstable system was also predicted when the proportional gain of the AC voltage controller was multipled by 3. Based on this research, it is therefore confirmed that the control loops of a microgrid might be a source of instability.

Chapter 6

Conclusion

This chapter presents the concluding remark, in addition to provide a recommendation for future work.

6.1 Concluding Remark

The increased focus on decreasing environmental pollution has led to a technological shift in the power industry and VSC-based systems have received considerable attention due to its important role in the future grid. VSC-based systems are a necessary building block when moving from a centralized to a decentralized power generation. A decentralized power system take advantage of distributed generation which will lead to benefits such as higher energy efficiency, reliability and controllability. However, the increased amount of power electronics devices will also lead to new challenges for operating and controlling the power grid safely. The complexity and nonlinear characteristics of a VSC-based system emphasizes that it is necessary to have knowledge about methods that can perform preliminary assessment of a systems stability.

To investigate the stability of a power electronics dominated system, the modeling and control of a VSC for two different control strategies, current controlled and AC voltage controlled, where discussed. By connecting several VSCs in parallel, a microgrid with the possibility to switch between the two different control strategies to enable operations in both grid-connected and islanded mode where presented. Furthermore, a small-signal representation of the state-space model of the current controlled VSC and the AC voltage controlled VSC where derived. The intention of deriving the small-signal state-space model was to explain the importance of linearization when applying a large proportion of the stability analysis methods and to show how the eigenvalue-based stability analysis can be used as an alternative method to predict the stability. The impact of the grid inductance was investigated for the current controlled VSC. It was shown that 2 pairs of complex conjugated poles where located on the RHP, which indicates an unstable system, after increasing L_g to 1.0 pu. For the AC voltage controlled VSC, the impact of

the proportional gain of the AC voltage controller was investigated. It was shown that 1 pair of complex conjugated poles were located at the RHP after decreasing k_{pvac} to 1% of its original value. To validate the correctness of the analytically predicted stability, the small-signal representation of the two state-space models were further validated by comparing it to a nonlinear model.

This thesis has mainly focused on small-signal stability analysis in the frequency domain and introduces the impedance-based stability analysis to predict the stability of a power electronics dominated system. One of the advantages of this method is that it needs less computation and includes the impact of the controller dynamics and the grid impedance on the stability. Another advantage is that the method do not need the detailed modeling of the system and are therefore able to predict the stability even if the systems is presented as a black box. To apply the method on a power electronics dominated system, it is a prerequisite that the impedance models are obtained. The impedance models of a current controlled VSC and an AC voltage controlled VSC is therefore derived utilizing the steady-state values from the small-signal state-space models. This knowledge is furthermore combined to obtain the impedance models of a grid-connected and an islanded microgrid.

By applying the impedance-based stability analysis on the minor-loop gain, which is the ratio of source and load impedance, the stability of the VSC-based systems was investigated. The main findings included an understanding of how the system and control parameters affect the stability of a power electronics dominated system. It was established that a weak grid represented by a large grid impedance is a source of instability for both the current-controlled VSC and the grid-connected microgrid. It was also shown that a single VSC was able to better withstand a weak grid than the microgrid. Furthermore, the impact of the current control and PLL parameters was investigated. It was shown that the current-controlled VSC was predicted to be unstable when decreasing the proportional gain of the current controller and increasing the integral gain of the PLL. The same could be observed for the grid-connected microgrid, except that it required that the proportional gain of two of the current control loops and the integral gain of all the PLL loops had to be changed to experience instability. Based on this, it can be concluded that it is more demanding to destabilize a microgrid than a single VSC by changing the control parameters. It was also discovered that even though the system became unstable after changing the control parameter, the Bode plot of the PLL and current controller implied stable operations. This emphasizes the importance of the impedance-based stability analysis.

The AC voltage controlled VSC is disconnected to the grid and by applying the impedance-based stability analysis it was identified that a small load resistor would lead to instability due to the large currents required. It was also established that changing the proportional gain of the AC voltage controller would lead to instability. The impact of changing control parameters were also investigated for the islanded microgrid. It was observed that an increase in the AC voltage control proportional gain would have a negative impact on the stability. Lastly, it was established that the proportional gain of two of the current controllers had to be changed to influence the stability of the microgrid.

6.2 Recommendation for Future Work

In this report, the impedance-based stability analysis was applied to a relatively small and simple system. One way to make the system more close to reality would be to remove the assumption of a constant voltage on the DC side and to add a DC voltage control loop. Because of this, it would be interesting to also apply the impedance-based stability analysis on the DC side to see if any of the sources of instability where neglected when analyzing it only from the AC side. To expand the system further, a HVDC transmission line from the wind power unit to the AC grid could be implemented. Since a weakness of the impedance-based stability analysis is that it has limited observability for larger systems, it would be interesting to investigate the stability at more than one interface, to find the critical location of where the method should be implemented. By applying another stability analysis method, as the eigenvalue-based method, for the same cases as in Chapter 5, it would be possible to compare the results from two different methods and to investigate the potential lacks of the impedance-based stability analysis. By presenting a broader analysis of the islanded and grid-connected microgrid, it would be interesting to compare the stability strength of the two operation modes. Lastly, the impedance model of the AC voltage controlled VSC should be verified.

Appendices

Appendix A

Base Values of Per Unit System

A per unit system is developed to simplify calculations and to easier understand the relationship between the parameter magnitudes. The base system is decided from (A.1) where V_b is the nominal peak voltage at the AC side that is decided from the line-to-line RMS voltage, V_n. S_b and I_b is the nominal three-phase power and nominal peak phase current, respectively. Z_b, L_b and C_b are the base AC impedance, inductance and capacitance. Lastly, ω_b is the base frequency. The resulting base values of the system are given in Table A.1.

$$V_b = \frac{\sqrt{2}}{\sqrt{3}} V_n, \quad I_b = \frac{2}{3}\frac{S_b}{V_b}, \quad Z_b = \frac{V_b}{I_b}, \quad L_b = \frac{Z_b}{\omega_b}, \quad C_b = \frac{1}{Z_b \omega_b} \tag{A.1}$$

Table A.1: Base values of the system.

Parameter	Base Value
S_b	15 kVA
V_b	187.8 V
I_b	53.3 A
Z_b	3.52 Ω
ω_b	314.2 rad/s
L_b	11.2 mH
C_b	902.7 μC

Appendix B

Direct-Quadrature-Zero Transform

The Direct-Quadrature-Zero (dqz) transform consists of two steps and is used to transform three-phase signals into three constant signals. First, the Clarke transform is used to convert time domain signals in the abc-reference frame into signals in the stationary orthogonal $\alpha\beta\gamma$-reference frame. The second and last transform is the Park transform which transform the $\alpha\beta\gamma$ signals to dqz-signals in a rotational orthogonal frame. The rotation of the axis is set to match the speed of the phases, which eliminates the relative motion between the transforms. The result from the transform is given in Fig. B.1 and the matrix used to go from abc- to dqz-frame is given in (B.1). For symmetrical systems, the zero-line in Fig. B.1b and B.1c is removed, and one is left with an $\alpha\beta$- and dq-frame with two signals instead of three.

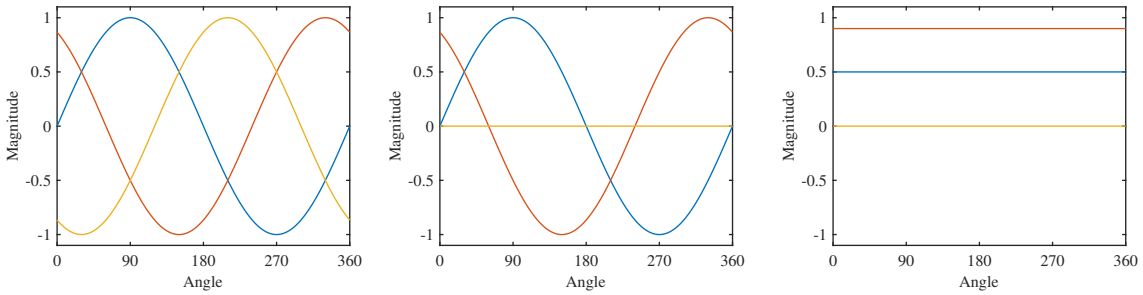

(a) abc-frame (b) $\alpha\beta$-frame (c) dq-frame

Figure B.1: Dq-transformation.

$$\begin{bmatrix} d \\ q \\ 0 \end{bmatrix} = \frac{2}{3} \begin{bmatrix} \sin\theta & \sin(\theta - \frac{2\pi}{3}) & \sin(\theta - \frac{4\pi}{3}) \\ \cos\theta & \cos(\theta - \frac{2\pi}{3}) & \cos(\theta - \frac{4\pi}{3}) \\ \frac{1}{2} & \frac{1}{2} & \frac{1}{2} \end{bmatrix} \begin{bmatrix} a \\ b \\ c \end{bmatrix} \tag{B.1}$$

Appendix C

Simulink Models

In the following, the most important Simulink models are presented. This includes the current controlled VSC, the AC voltage controlled VSC and the microgrid.

C.1 Current Controlled VSC

The structure of the current controlled VSC connected to the grid is shown in Fig. C.1. The electrical system, PLL and inner current control loop is depicted in Fig. C.2, C.3 and C.4, respectively.

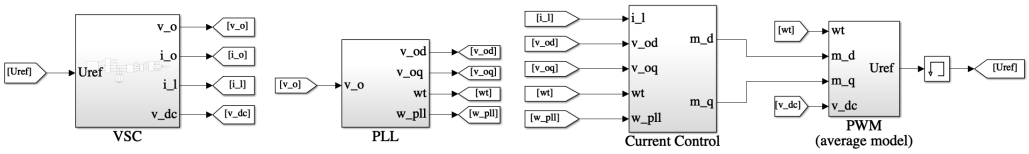

Figure C.1: Overview of the current controlled VSC.

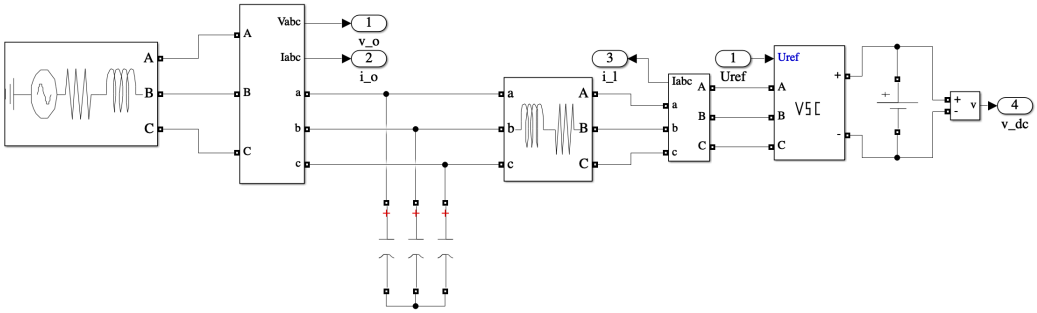

Figure C.2: Electric circuit of current controlled VSC.

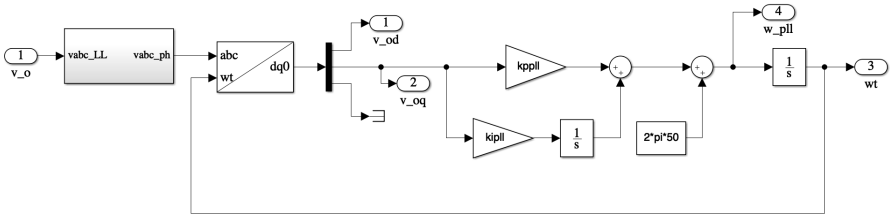

Figure C.3: PLL of the current controlled VSC.

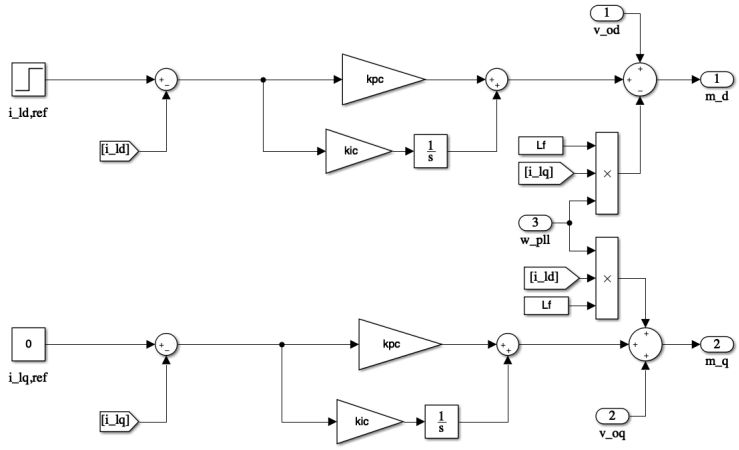

Figure C.4: Inner current control of the grid-connected VSC.

C.2 AC Voltage Controlled VSC

The electric circuit of the AC voltage controlled VSC is given in Fig. C.5. The grid is now disconnected from the grid and the phase of the voltage is found according to Fig. C.6. The AC voltage controller in Fig. C.7 is implemented to control the AC voltage and to create the reference current signals.

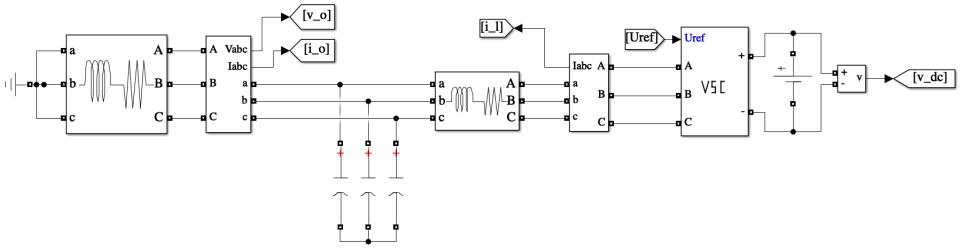

Figure C.5: Electric circuit of AC voltage controlled VSC.

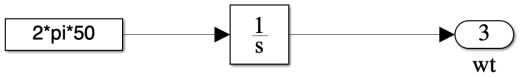

Figure C.6: Retrieving of phase of a AC voltage controlled VSC.

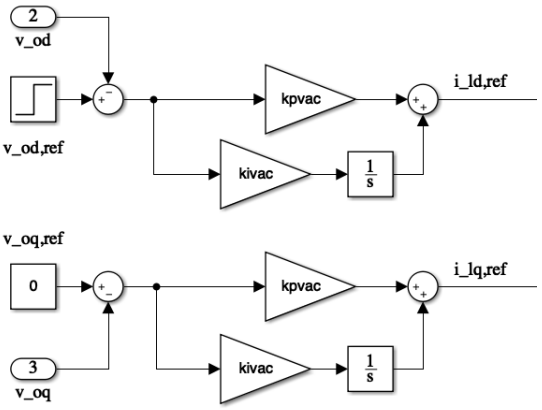

Figure C.7: Outer voltage control of the VSC.

C.3 Microgrid

Fig. C.8 shows how the VSCs and RL-load are connected in parallel to constitute a microgrid. A three-phase circuit breaker is implemented on the grid side to enable changing between islanded and grid-connected mode.

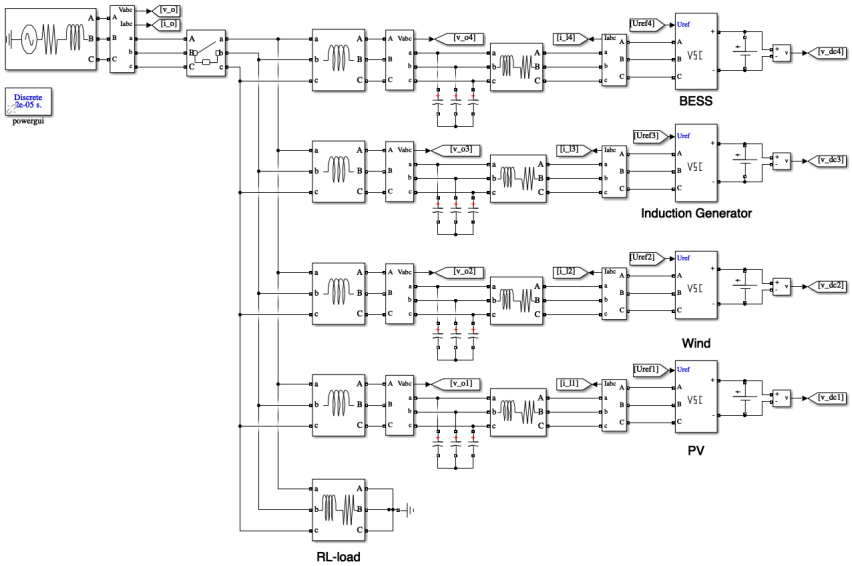

Figure C.8: Electric circuit of microgrid.

The VSC of the induction generator, PV and wind is based on the current controlled strategy shown in Fig. C.4, while the BESS has the possibility to change between a current controlled and AC voltage controlled strategy. To enable this, the PLL of Fig. C.9 is implemented. When the grid is connected the switch is closed and the PLL works according to the one introduced for the current controlled VSC. On the other hand, when the grid is disconnected the switch opens, the PI-controller is decoupled and the phase is retrieved by integrating the base frequency according to the method introduced for the AC voltage controlled VSC.

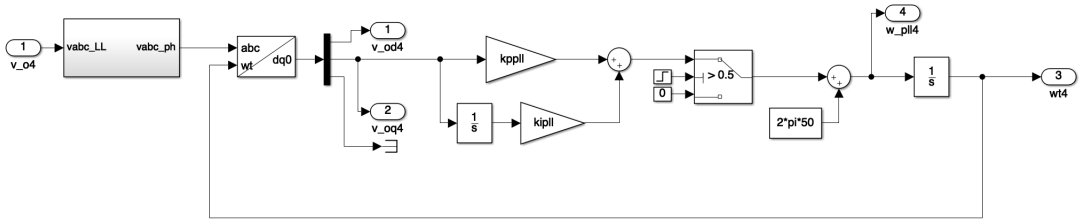

Figure C.9: PLL of the microgrid.

It is also necessary to combine the current control strategy and the AC voltage control strategy to enable grid-connected and islanded operations of the microgrid. Fig. C.10 illustrates how the outer AC voltage control loop can be connected through a switch when the grid is disconnected, while it will be decoupled so that it is only an inner current control loop in grid-connected mode. This also applies for the cross-coupling term, where a switch is implemented to either multiply with ω_b or ω_{pll}.

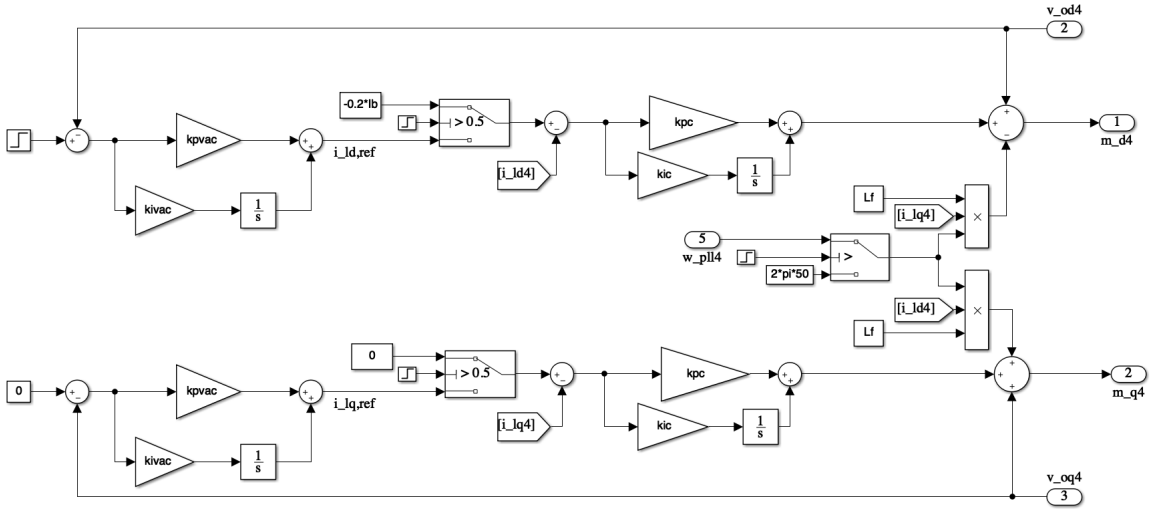

Figure C.10: Control strategy of the microgrid.

Appendix D

Small-Signal State-Space Model

In the following the linearized small-signal state-space model of both a current controlled and an AC voltage controlled VSC are presented.

D.1 Current Controlled VSC

Matrices A and B of the current controlled VSC are given in (D.1) and (D.2), respectively.

$$A = \begin{bmatrix} -\frac{\omega_b(k_{pc}+R_c)}{L_c} & -\omega_b(\varepsilon_0 k_{ipll} + k_{ppll} V_{oq0}) & 0 & -\omega_b I_{lq0} k_{ppll} & 0 & 0 & \frac{\omega_b k_{ic}}{L_c} & 0 & -\omega_b I_{lq0} k_{ipll} & 0 \\ \omega_b(\varepsilon_0 k_{ipll} + k_{ppll} V_{oq0}) & -\frac{\omega_b(k_{pc}+R_c)}{L_c} & 0 & \omega_b I_{ld0} k_{ppll} & 0 & 0 & 0 & \frac{\omega_b k_{ic}}{L_c} & \omega_b I_{ld0} k_{ipll} & 0 \\ \frac{\omega_b}{C_f} & 0 & 0 & \omega_b \omega_{g0} & -\frac{\omega_b}{C_f} & 0 & 0 & 0 & 0 & 0 \\ 0 & \frac{\omega_b}{C_f} & -\omega_b \omega_{g0} & 0 & 0 & -\frac{\omega_b}{C_f} & 0 & o & 0 & 0 \\ 0 & 0 & \frac{\omega_b}{L_g} & 0 & -\frac{\omega_b R_g}{L_g} & \omega_b \omega_{g0} & 0 & 0 & 0 & \frac{\omega_b V_{g0} \sin \delta\theta_0}{L_g} \\ 0 & 0 & 0 & \frac{\omega_b}{L_g} & -\omega_b \omega_{g0} & -\frac{\omega_b R_g}{L_g} & 0 & 0 & 0 & \frac{\omega_b V_{g0} \cos \delta\theta_0}{L_g} \\ -1 & 0 & 0 & 0 & 0 & 0 & 0 & 0 & 0 & 0 \\ 0 & -1 & 0 & 0 & 0 & 0 & 0 & 0 & 0 & 0 \\ 0 & 0 & 0 & 1 & 0 & 0 & 0 & 0 & 0 & 0 \\ 0 & 0 & 0 & \omega_b k_{ppll} & 0 & 0 & 0 & 0 & \omega_b k_{ipll} & 0 \end{bmatrix} \tag{D.1}$$

$$B = \begin{bmatrix} \frac{\omega_b k_{pc}}{L_c} & 0 & 0 & 0 \\ 0 & \frac{\omega_b k_{pc}}{L_c} & 0 & 0 \\ 0 & 0 & 0 & \omega_b V_{oq0} \\ 0 & 0 & 0 & -\omega_b V_{od0} \\ 0 & 0 & -\frac{\omega_b \cos \delta\theta_o}{L_g} & \omega_b I_{oq0} \\ 0 & 0 & \frac{\omega_b \sin \delta\theta_o}{L_g} & -\omega_b I_{od0} \\ 1 & 0 & 0 & 0 \\ 0 & 1 & 0 & 0 \\ 0 & 0 & 0 & 0 \\ 0 & 0 & 0 & 0 \end{bmatrix} \tag{D.2}$$

D.2 AC Voltage Controlled VSC

Matrices A and B of an AC voltage controlled VSC are given in (D.3) and (D.4), respectively.

$$A = \begin{bmatrix} 0 & \omega_b\omega_{g0} & \frac{\omega_b}{C_f} & 0 & 0 & 0 & -\frac{\omega_b}{C_f} & 0 & 0 & 0 \\ -\omega_b\omega_{g0} & 0 & 0 & \frac{\omega_b}{C_f} & 0 & 0 & 0 & -\frac{\omega_b}{C_f} & 0 & 0 \\ -\frac{\omega_b k_{pvac} k_{pc}}{L_c} & 0 & -\frac{\omega_b(k_{pc}+R_c)}{L_c} & 0 & \frac{\omega_b k_{ic}}{L_c} & 0 & 0 & 0 & \frac{\omega_b k_{ivac} k_{pc}}{L_c} & 0 \\ 0 & -\frac{\omega_b k_{pvac} k_{pc}}{L_c} & 0 & -\frac{\omega_b(k_{pc}+R_c)}{L_c} & 0 & \frac{\omega_b k_{ic}}{L_c} & 0 & 0 & 0 & \frac{\omega_b k_{ivac} k_{pc}}{L_c} \\ -k_{pvac} & 0 & -1 & 0 & 0 & 0 & 0 & 0 & k_{ivac} & 0 \\ 0 & -k_{pvac} & 0 & -1 & 0 & 0 & 0 & 0 & 0 & k_{ivac} \\ \frac{\omega_b}{L_l} & 0 & 0 & 0 & 0 & 0 & -\frac{\omega_b R_g}{L_l} & \omega_b\omega_{g0} & 0 & 0 \\ 0 & \frac{\omega_b}{L_l} & 0 & 0 & 0 & 0 & -\omega_b\omega_{g0} & -\frac{\omega_b R_g}{L_l} & 0 & 0 \\ -1 & 0 & 0 & 0 & 0 & 0 & 0 & 0 & 0 & 0 \\ 0 & -1 & 0 & 0 & 0 & 0 & 0 & 0 & 0 & 0 \end{bmatrix} \tag{D.3}$$

$$B = \begin{bmatrix} 0 & 0 & \omega_b V_{oq0} \\ 0 & 0 & -\omega_b V_{od0} \\ 0 & \frac{\omega_b k_{pvac} k_{pc}}{L_c} & 0 \\ \frac{\omega_b k_{pvac} k_{pc}}{L_c} & 0 & 0 \\ 0 & k_{pvac} & 0 \\ k_{pvac} & 0 & 0 \\ 0 & 0 & \omega_v I_{oq0} \\ 0 & 0 & -\omega_v I_{od0} \\ 0 & 1 & 0 \\ 1 & 0 & 0 \end{bmatrix} \tag{D.4}$$

Bibliography

[1] J. Zhang. Power electronics in future electrical power grids. In *2013 4th IEEE International Symposium on Power Electronics for Distributed Generation Systems (PEDG)*, pages 1–3, 2013.

[2] J. Driesen and F. Katiraei. Design for distributed energy resources. *IEEE Power and Energy Magazine*, 6(3):30–40, 2008.

[3] M. T. Miller, M. B. Johns, E. Sortomme, and S. S. Venkata. Advanced integration of distributed energy resources. In *2012 IEEE Power and Energy Society General Meeting*, pages 1–2, 2012.

[4] E. J. Coster, J. M. A. Myrzik, B. Kruimer, and W. L. Kling. Integration issues of distributed generation in distribution grids. *Proceedings of the IEEE*, 99(1):28–39, 2011.

[5] N. Hatziargyriou, H. Asano, R. Iravani, and C. Marnay. Microgrids. *IEEE Power and Energy Magazine*, 5(4):78–94, 2007.

[6] X. Zhou, T. Guo, and Y. Ma. An overview on microgrid technology. In *2015 IEEE International Conference on Mechatronics and Automation (ICMA)*, pages 76–81, 2015.

[7] F. Blaabjerg, Y. Yang, and K. Ma. Power electronics - key technology for renewable energy systems - status and future. In *2013 3rd International Conference on Electric Power and Energy Conversion Systems*, pages 1–6, 2013.

[8] M. Sanz, V. Valdivia, P. Zumel, D. L. del Moral, C. Fernández, A. Lázaro, and A. Barrado. Analysis of the stability of power electronics systems: A practical approach. In *2014 IEEE Applied Power Electronics Conference and Exposition - APEC 2014*, pages 2682–2689, 2014.

[9] S. Jena, S. Sahoo, and C. K. Panigrahi. Interconnection of renewables to the utility grid by three phase pulse width modulated voltage source inverter without phase locked loop. In *2016 International Conference on Signal Processing, Communication, Power and Embedded System (SCOPES)*, pages 818–823, 2016.

[10] M. Amin and M. Molinas. Small-signal stability assessment of power electronics based power systems: A discussion of impedance- and eigenvalue-based methods. *IEEE Transactions on Industry Applications*, 53(5):5014–5030, 2017.

[11] S. Lissandron, L. Dalla Santa, P. Mattavelli, and B. Wen. Experimental validation for impedance-based small-signal stability analysis of single-phase interconnected power systems with grid-feeding inverters. *IEEE Journal of Emerging and Selected Topics in Power Electronics*, 4(1):103–115, 2016.

[12] A. Rygg and M. Molinas. Apparent impedance analysis: A small-signal method for stability analysis of power electronic-based systems. *IEEE Journal of Emerging and Selected Topics in Power Electronics*, 5(4):1474–1486, 2017.

[13] X. Wang, L. Harnefors, and F. Blaabjerg. Unified impedance model of grid-connected voltage-source converters. *IEEE Transactions on Power Electronics*, 33(2):1775–1787, 2018.

[14] J. Sun. Impedance-based stability criterion for grid-connected inverters. *IEEE Transactions on Power Electronics*, 26(11):3075–3078, 2011.

[15] L. Harnefors, M. Bongiorno, and S. Lundberg. Input-admittance calculation and shaping for controlled voltage-source converters. *IEEE Transactions on Industrial Electronics*, 54(6):3323–3334, 2007.

[16] M. Amin, A. Rygg, and M. Molinas. Impedance-based and eigenvalue based stability assessment compared in vsc-hvdc system. In *2016 IEEE Energy Conversion Congress and Exposition (ECCE)*, pages 1–8, 2016.

[17] T. Midtsund, J. A. Suul, and T. Undeland. Evaluation of current controller performance and stability for voltage source converters connected to a weak grid. In *The 2nd International Symposium on Power Electronics for Distributed Generation Systems*, pages 382–388, 2010.

[18] J. A. Suul, M. Molinas, L. Norum, and T. Undeland. Tuning of control loops for grid connected voltage source converters. In *2008 IEEE 2nd International Power and Energy Conference*, pages 797–802, 2008.

[19] J. Sun. Small-signal methods for ac distributed power systems–a review. *IEEE Transactions on Power Electronics*, 24(11):2545–2554, 2009.

[20] Q. Ye, R. Mo, Y. Shi, and H. Li. A unified impedance-based stability criterion (uibsc) for paralleled grid-tied inverters using global minor loop gain (gmlg). In *2015 IEEE Energy Conversion Congress and Exposition (ECCE)*, pages 5816–5821, 2015.

[21] B. Wen, D. Boroyevich, R. Burgos, P. Mattavelli, and Z. Shen. Inverse nyquist stability criterion for grid-tied inverters. *IEEE Transactions on Power Electronics*, 32(2):1548–1556, 2017.

[22] B. Wen, D. Boroyevich, P. Mattavelli, R. Burgos, and Z. Shen. Impedance-based analysis of grid-synchronization stability for three-phase paralleled converters. In *2014 IEEE Applied Power Electronics Conference and Exposition - APEC 2014*, pages 1233–1239, 2014.

[23] M. Amin and M. Molinas. Understanding the origin of oscillatory phenomena observed between wind farms and hvdc systems. *IEEE Journal of Emerging and Selected Topics in Power Electronics*, 5(1):378–392, 2017.

[24] M. Amin and M. Molinas. Impedance based stability analysis of vsc-based hvdc system. In *2015 IEEE Eindhoven PowerTech*, pages 1–6, 2015.

[25] A. Khalil, K. A. Alfaitori, and A. Elbarsha. Stability analysis of parallel-inverters in microgrid. In *2014 20th International Conference on Automation and Computing*, pages 110–115, 2014.

[26] N. Beg, A. Armstorfer, A. Rosin, and H. Biechl. Mathematical modeling and stability analysis of a microgrid in island operation. In *2018 International Conference on Smart Energy Systems and Technologies (SEST)*, pages 1–6, 2018.

[27] M. Mao, W. Zhu, and L. Chang. Stability analysis method for interconnected ac islanded microgrids. In *2018 IEEE International Power Electronics and Application Conference and Exposition (PEAC)*, pages 1–6, 2018.

[28] M. R. Pettersen. Stability assessment of a grid-connected voltage source converter applying the impedance-based stability analysis. Project report in TTM4502, Department of Electric Power Engineering, NTNU – Norwegian University of Science and Technology, Dec. 2019.

[29] Yang Ye, M. Kazerani, and V. H. Quintana. Modeling, control and implementation of three-phase pwm converters. *IEEE Transactions on Power Electronics*, 18(3):857–864, 2003.

[30] REN21 Members. Renewables 2019 global status report. `https://www.ren21.net/wp-content/uploads/2019/05/gsr_2019_full_report_en.pdf`.

[31] Q. Jiang, M. Xue, and G. Geng. Energy management of microgrid in grid-connected and stand-alone modes. *IEEE Transactions on Power Systems*, 28(3):3380–3389, 2013.

[32] S. Parhizi, H. Lotfi, A. Khodaei, and S. Bahramirad. State of the art in research on microgrids: A review. *IEEE Access*, 3:890–925, 2015.

[33] K. A. Potty, P. Keny, and C. Nagarajan. An intelligent microgrid with distributed generation. In *2013 IEEE Innovative Smart Grid Technologies-Asia (ISGT Asia)*, pages 1–5, 2013.

[34] B. Lasseter. Microgrids [distributed power generation]. In *2001 IEEE Power Engineering Society Winter Meeting. Conference Proceedings (Cat. No.01CH37194)*, volume 1, pages 146–149 vol.1, 2001.

[35] O. E. Oni, I. E. Davidson, and K. N. I. Mbangula. A review of lcc-hvdc and vsc-hvdc technologies and applications. In *2016 IEEE 16th International Conference on Environment and Electrical Engineering (EEEIC)*, pages 1–7, 2016.

[36] P. Nguyen and M. Han. Study on harmonic propagation of vsc-based hvdc systems. In *2014 International Conference on Power System Technology*, pages 2146–2153, 2014.

[37] M. N. Hellesnes. Use of battery energy storage for power balancing in a large-scale hvdc connected wind power plant. Master's thesis, Norwegian University of Science and Technology, 6 2017.

[38] Y. Zhang, G. P. Adam, T. C. Lim, S. J. Finney, and B. W. Williams. Voltage source converter in high voltage applications: Multilevel versus two-level converters. In *9th IET International Conference on AC and DC Power Transmission (ACDC 2010)*, pages 1–5, 2010.

[39] T. Jing and A. S. Maklakov. A review of voltage source converters for energy applications. In *2018 International Ural Conference on Green Energy (UralCon)*, pages 275–281, 2018.

[40] M. P. Bahrman, J. G. Johansson, and B. A. Nilsson. Voltage source converter transmission technologies: the right fit for the application. In *2003 IEEE Power Engineering Society General Meeting (IEEE Cat. No.03CH37491)*, volume 3, pages 1840–1847 Vol. 3, 2003.

[41] L. Dongdong, T. Zhengyan, Y. Cikai, and S. S. Kumar. Design and implementation of space vector modulated three phase voltage source inverter. In *2019 IEEE International Conference on Sustainable Energy Technologies and Systems (ICSETS)*, pages 331–335, 2019.

[42] H. I. Sari. Dc/dc converters for multi-terminal hvdc systems. Master's thesis, Norwegian University of Science and Technology, 8 2016.

[43] H. Chen and H. Zhao. Review on pulse-width modulation strategies for common-mode voltage reduction in three-phase voltage-source inverters. *IET Power Electronics*, 9(14):2611–2620, 2016.

[44] H. Azani, A. Massoud, L. Benbrahim, B. W. Williams, and D. Holiday. An lcl filter-based grid-interfaced three-phase voltage source inverter: Performance evaluation and stability anaylsis. In *7th IET International Conference on Power Electronics, Machines and Drives (PEMD 2014)*, pages 1–6, 2014.

[45] C. A. H. Mora and N. L. Díaz Aldana. Vectorial control of a voltage source converter. In *2010 IEEE/PES Transmission and Distribution Conference and Exposition: Latin America (T D-LA)*, pages 689–693, 2010.

[46] M. Cespedes and J. Sun. Impedance modeling and analysis of grid-connected voltage-source converters. *IEEE Transactions on Power Electronics*, 29(3):1254–1261, 2014.

[47] S. Eren, A. Bakhshai, and P. Jain. Control of three-phase voltage source inverter for renewable energy applications. In *2011 IEEE 33rd International Telecommunications Energy Conference (INTELEC)*, pages 1–4, 2011.

[48] Guan-Chyun Hsieh and J. C. Hung. Phase-locked loop techniques. a survey. *IEEE Transactions on Industrial Electronics*, 43(6):609–615, 1996.

[49] S. Golestan, J. M. Guerrero, and J. C. Vasquez. Three-phase plls: A review of recent advances. *IEEE Transactions on Power Electronics*, 32(3):1894–1907, 2017.

[50] T. Kalitjuka. Control of voltage source converters for power system applications. Master's thesis, Norwegian University of Science and Technology, 7 2011.

[51] V. Blasko and V. Kaura. A new mathematical model and control of a three-phase ac-dc voltage source converter. *IEEE Transactions on Power Electronics*, 12(1):116–123, 1997.

[52] M. Molinas C. Bajracharya, J. A. Suul, and T. Undeland. Understanding of tuning techniques of converter controllers for vsc-hvdc. In *2008 Nordic Workshop on Power and Industrial Electronics*, 2008.

[53] M. Amin and M. Molinas. A gray-box method for stability and controller parameter estimation in hvdc-connected wind farms based on nonparametric impedance. *IEEE Transactions on Industrial Electronics*, 66(3):1872–1882, 2019.

[54] M. Patino, S. Höhn, R. Dimitrovski, and M. Luther. Methodology for state-space modelling of power electronic elements in modern electrical energy systems. In *15th IET International Conference on AC and DC Power Transmission (ACDC 2019)*, pages 1–6, 2019.

[55] Gengyin Li, Ming Yin, Ming Zhou, and Chenyong Zhao. Modeling of vsc-hvdc and control strategies for supplying both active and passive systems. In *2006 IEEE Power Engineering Society General Meeting*, pages 6 pp.–, 2006.

[56] M. Amin, J. A. Suul, S. D'Arco, E. Tedeschi, and M. Molinas. Impact of state-space modelling fidelity on the small-signal dynamics of vsc-hvdc systems. In *11th IET International Conference on AC and DC Power Transmission*, pages 1–11, Feb 2015.

[57] M. Amin, M. Molinas, and J. Lyu. Oscillatory phenomena between wind farms and hvdc systems: The impact of control. In *2015 IEEE 16th Workshop on Control and Modeling for Power Electronics (COMPEL)*, pages 1–8, 2015.

[58] S. D'Arco, J. A. Suul, and M. Molinas. Implementation and analysis of a control scheme for damping of oscillations in vsc-based hvdc grids. In *2014 16th International Power Electronics and Motion Control Conference and Exposition*, pages 586–593, Sep. 2014.

[59] B. Wen, D. Boroyevich, R. Burgos, P. Mattavelli, and Z. Shen. D-q impedance specification for balanced three-phase ac distributed power system. In *2015 IEEE Applied Power Electronics Conference and Exposition (APEC)*, pages 2757–2771, 2015.

[60] X. Wang, F. Blaabjerg, and P. C. Loh. An impedance-based stability analysis method for paralleled voltage source converters. In *2014 International Power Electronics Conference (IPEC-Hiroshima 2014 - ECCE ASIA)*, pages 1529–1535, 2014.

[61] B. Wen, D. Boroyevich, R. Burgos, P. Mattavelli, and Z. Shen. Analysis of d-q small-signal impedance of grid-tied inverters. *IEEE Transactions on Power Electronics*, 31(1):675–687, 2016.

[62] A. Rygg, M. Molinas, Chen Zhang, and Xu Cai. Frequency-dependent source and load impedances in power systems based on power electronic converters. In *2016 Power Systems Computation Conference (PSCC)*, pages 1–8, 2016.

[63] J. Huang, K. A. Corzine, and M. Belkhayat. Small-signal impedance measurement of power-electronics-based ac power systems using line-to-line current injection. *IEEE Transactions on Power Electronics*, 24(2):445–455, 2009.

[64] B. Wen, D. Boroyevich, R. Burgos, P. Mattavelli, and Z. Shen. Small-signal stability analysis of three-phase ac systems in the presence of constant power loads based on measured d-q frame impedances. *IEEE Transactions on Power Electronics*, 30(10):5952–5963, 2015.

[65] G. Francis, R. Burgos, D. Boroyevich, F. Wang, and K. Karimi. An algorithm and implementation system for measuring impedance in the d-q domain. In *2011 IEEE Energy Conversion Congress and Exposition*, pages 3221–3228, 2011.

[66] B. Wen, D. Boroyevich, P. Mattavelli, Z. Shen, and R. Burgos. Influence of phase-locked loop on input admittance of three-phase voltage-source converters. In *2013 Twenty-Eighth Annual IEEE Applied Power Electronics Conference and Exposition (APEC)*, pages 897–904, 2013.

Marie Rønhaug Pettersen

Stability Assessment of a Microgrid

NTNU
Norwegian University of
Science and Technology